Tunable soliton-based supercontinuum generation in liquid-core optical fibers

by M. Sc. Ramona Susanne Scheibinger

Dissertation

to obtain the academic title

"Doctor rerum naturalium" (Dr. rer. nat.)

submitted to the council of the

Faculty of Physics and Astronomy of the

FRIEDRICH-SCHILLER-UNIVERSITÄT JENA

based on research conducted at the

LEIBNIZ ipht
LEIBNIZ-INSTITUT *für* PHOTONISCHE TECHNOLOGIEN

Supervisor:

Prof. Dr. Markus A. Schmidt

Submitted:

September 2023

Gutachter:

Prof. Dr. Markus A. Schmidt, Friedrich-Schiller-Universität Jena, Jena

Prof. Dr. Christian Spielmann, Friedrich-Schiller-Universität Jena, Jena

Prof. dr hab. inz. Ryszard Buczynski, University of Warsaw, Warschau, Polen

Disputation am 20.02.2024

Abstract

This work presents the results of temperature-based control of supercontinuum generation in liquid-core step-index fibers. Modifying supercontinuum generation in optical fibers via temperature has two mayor motivations: First, spectral gaps between the wavelength ranges of commercial lasers can be filled via thermal control of wavelength conversion schemes. This helps to optimize the maximum output power with respect to different targeted applications. Second, the temperature tuning, which is especially effective in liquid-core step-index fibers, allows to modify the optical properties of the fibers and thus the dynamics of guided optical pulses. Thus, different nonlinear effects can be studied and fine-tuned in a fixed fiber.

The key parameter adapted via temperature in this work is the group velocity dispersion of the fiber modes, which determines the nonlinear pulse dynamics. Different soliton dynamics, e.g. soliton fission, soliton breathing, soliton breakdown, and soliton tunneling, are studied experimentally and numerically exciting higher-order modes in approximately 10 cm-long carbon disulfide-filled step-index fibers with ultrashort sub-40 fs pulses centered at a wavelength of 1.57 µm. By modifying the temperature of defined fiber sections, strong wavelength shifts of up to 33 nm/Kelvin are detected. The generated dispersive waves reach infrared wavelengths of up to 2.7 micrometers. The experimental results showing these strong thermo-spectral shifts are in good agreement with numerical simulations solving the nonlinear Schrödinger equation and corresponding phase matching calculations. The nonlinear simulations give further insights into the soliton dynamics taking place inside the fiber. In this way, the different soliton processes can be identified and precisely controlled via temperature. Parameters studies are conducted to learn about the optima and limits of the different soliton effects. Besides studying the influence of the absolute fiber temperature of a fixed fiber section, the impact of the length and position of the temperature-controlled fiber sections is investigated in experiments and simulations. Recompression-induced generation of additional dispersive waves is realized via soliton tunneling through normal dispersive regions of varying length.

In summary, this work demonstrates how different flat group velocity dispersion profiles with two ZDWs can be obtained in higher-order modes by controlling the temperature of liquid-core step-index fibers. The thereby strongly varied soliton dynamics result in significant spectral modifications of the generated supercontinua. The experimental and numerical results give proof for the flexible control over soliton dynamics and lay the foundation for temperature-based customization of supercontinuum generation.

Zusammenfassung

Diese Arbeit präsentiert die Ergebnisse variabler Superkontinuumsgeneration durch die Temperaturkontrolle von Flüssigkernstufenindexfasern. Die temperaturgesteuerte Anpassung der Superkontinuumsgeneration in optischen Glasfasern hat zwei Hauptmotivationen: Erstens erlaubt die Kontrolle über Wellenlängenkonversationsprozesse spektrale Lücken zwischen kommerziell verfügbaren Lasern zu schließen. Das hilft die maximale Ausgangsleistung gezielt für verschiedene Anwendungen zu optimieren. Zweitens ermöglicht das Temperaturtuning von Flüssigkernfasern deren optische Eigenschaften und damit die Dynamiken darin geleiteter optischer Pulse sehr flexibel zu verändern, so dass unterschiedlichste nichtlineare Effekte in ein und derselben Faser untersucht und fein abgestimmt werden können.

Der Schlüsselparameter, der in dieser Arbeit durch die Temperaturänderungen angepasst wird, ist die Gruppengeschwindigkeitsdispersion, die die nichtlinearen Pulsdynamiken grundlegend beeinflusst. Durch das Anregen von höheren Ordnungsmoden in etwa 10cm-langen Kohlenstoffdisulfid- gefüllten Stufenindexfasern mit ultrakurzen Pulsen (kürzer 40 fs) einer zentralen Wellenlänge von 1,57 μm werden verschiedene Solitonendynamiken experimentell und in Simulationen untersucht, zum Beispiel das Aufspalten (engl. fission), Atmen (engl. breathing), Zerfallen (engl. breakdown) und Tunneln (engl. tunneling) von Solitonen. Dabei werden temperaturinduzierte Wellenlängenverschiebungen von bis zu 33 nm pro Kelvin detektiert und die dispersiven Wellen erreichen Wellenlängen von bis zu 2,7 Mikrometern im Infraroten. Die experimentellen Ergebnisse, die diese starke Wellenlängenverschiebung zeigen, decken sich mit den Ergebnissen numerischer Simulationen der nichtlinearen Schrödingergleichung, sowie mit Berechnungen der Phasenanpassungsbedingung. Die nichtlinearen Simulationen geben Einblicke in die Solitonendynamiken entlang der optischen Faser, wodurch die unterschiedlichen Effekte identifiziert und präzise durch Temperaturänderungen kontrolliert werden können. Parameterstudien geben neue Aufschlüsse über die Optimierungsmöglichkeiten und Grenzen der unterschiedlichen Solitonendynamiken. Neben dem Einfluss absoluter Temperaturunterschiede in einem festgelegten Faserabschnitt, wird auch der Einfluss der Länge und Position der temperaturkontrollierten Bereiche experimentell und numerisch untersucht. So können durch die erneute Komprimierung von Solitonen nach dem Tunneln durch normal dispersive Bereiche unterschiedlicher Länge zusätzliche dispersive Wellen erzeugt werden.

Zusammenfassend zeigt diese Arbeit wie durch Kontrolle der Temperatur von Flüssigkernstufenindexfasern unterschiedliche, flache Gruppengeschwindigkeitsdispersionsprofile mit zwei Nulldispersionswellenlängen für höhere Ordnungsmoden erreicht werden können. Die dadurch stark veränderlichen Solitonendynamiken äußern sich in spektralen Änderungen der erzeugten Superkontinua. Die experimentellen und numerischen Ergebnisse belegen die flexible Steuerung der Solitonendynamiken und legen die Grundlage für maßangepasste Supercontinuumsgeneration durch Temperaturkontrolle.

Contents

List of Figures

List of Tables

List of acronyms

AD anomalous (group velocity) dispersion

DW dispersive wave

GNLSE generalized nonlinear Schrödinger equation

GVD group velocity dispersion

HOM higher-order mode

LCF liquid-core (step-index) fiber

ND normal (group velocity) dispersion

OSA optical spectrum analyzer

PCF photonic crystal fiber

SCG supercontinuum generation

ZDW zero dispersion wavelength

1 Introduction

Development of light sources

Humans have been fascinated by light since time immemorial. Our lives are dependent on the sunlight. The influence of the ecliptic plane of earth around the sun, which strongly influences agriculture, was studied very early and incorporated in prehistoric monuments such as Stonehenge and pyramids. The ability to control, preserve and make fire is supposed to be a crucial development step in human evolution [1]. Controllable light has remained an important subject of research until today. Light sources have been used for illumination purposes for a long time, but also became a powerful tool in research, industries and medicine. Laser sources are continuously developed further to increase theirs power, improve theirs efficiencies, shorten theirs pulse widths and extend theirs wavelength domains [2], [3]. They dominate over other light sources, such as thermal emitters and light emitting diodes, due to their high power in combination with high spatial coherence [4]. As laser beams can be tightly focused to narrow spots they became almost irreplaceable tools for many applications, such as high power material processing (e.g. laser cutting [5], cladding [6], and welding [7]), nanoscale material processing (e.g. lithography [8]), material analysis (e.g. spectroscopy [9]), and medical treatments (e.g. laser-based eye surgery [10]). Furthermore, laser beams can remain spatially confined while being transmitted over very long distances, which led to new developments in telecommunication (e.g. fiber-based internet), geographical mapping (e.g. LIDAR), military technologies (e.g. directed-energy weapons), and large-scale interferometric experiments (e.g. Laser Interferometer Gravitational-Wave Observatory, LIGO).

Many different laser types have been developed since the first demonstrations of laser emission in 1960, when a solid state ruby laser [11], as well as a helium-neon gas laser [12] were invented shortly after each other. While ruby lasers produce laser pulses at a visible wavelength of 694.3 nm, the first helium-neon laser emitted continuous waves (non-pulsed light) in the infrared wavelength domain at 1152.3 nm, but can also emit other wavelengths like 632.8 nm in the visible, and 3392.2 nm in the mid infrared. Pulsed lasers as well continuous wave lasers are highly requested for a manifold of applications until today [13]–[16]. Further development of lasers mainly targets extending the wavelength range, increasing their power, and reducing the pulse duration of pulsed lasers [3], [17]. Besides, other laser characteristics like temporal and spatial coherence [4], relative intensity noise [18], [19], as well as pulse chirp [20], [21] are continuously optimized to improve existing systems and enable new applications.

Wavelength conversion via nonlinear optical effects

Nonlinear effects are often used to modify the emitted wavelengths, and to compress optical pulses of existing laser sources. The term 'nonlinear' describes some optical ef-

fects that are dependent on the intensity of the incident laser beam [22]. For example the refractive index of a nonlinear medium can be modified by intense laser pulses, which is called optical Kerr effect [23], [24]. The optical Kerr effect is a third-order nonlinear effect that leads to wavelength conversion processes such as self-phase modulation [25], cross-phase-modulation [26], and four-wave mixing [27]. Optical waveguides with nonlinear core materials are often used for nonlinear wavelength conversion, because the confinement of the laser beam in the core allows to maintain high intensities over long interaction lengths, which enables strong nonlinear effects [28]. If the initial laser spectrum gets significantly broadened this is called supercontinuum generation (SCG). Broadband supercontinuum spectra (also called supercontinua) often result from a combination of different nonlinear and dispersive effects [29], [30]. One key parameter for SCG is the group velocity dispersion (GVD) of the guided mode in the waveguide [28]. The GVD describes the delay of different spectral components of an optical pulse induced in a medium, which influences the chirp of the pulse. If the GVD is negative, a light beam propagating through the medium experiences anomalous dispersion (AD), so that short-wavelength components travel faster than long-wavelength components. In this case temporally stable pulses can be formed, which are called temporal optical solitary waves [31], [32], and in the following only referred to as solitons. Solitons can efficiently transfer energy to phase-matched wavelengths in the normal dispersion (ND) domains, which leads to a prominent broadening of the spectrum [30]. A small absolute GVD is advantageous for nonlinear soliton-driven SCG, because this prevents a decrease in peak power typically caused by temporal dispersion. The GVD can be adapted by the chosen mode or the fiber geometry [33]. In the last decades many specialized waveguides with flat AD regimes were developed to obtain extremely broadened spectra [34]–[58]. Additional prerequisites for broadband SCG are strong light confinement in the waveguide core, high nonlinearity and wide transmission windows of the waveguide material.

Extending spectra to ultraviolet wavelengths (10 nm - 400 nm) is of great significance for characterization applications such as spectroscopy of biomolecules [59], fluorescence microscopy [60] and photochemical reactions monitoring [61]. Broadband light sources with longer wavelengths than the visible spectrum, i.e. at infrared wavelengths, are required for various spectroscopy and imaging applications like remote gas sensing [9], [62], microspectroscopy [63], and optical coherence tomography [64]. Infrared supercontinua also have great potential for wavelength-division multiplexing transmission in telecommunication [65], and ultrafast photonics [66]. Infrared wavelength are classified into near infrared (0.78 - 3 µm), mid infrared (3 - 50 µm), and far infrared (50 - 1000 µm) wavelength domains [67], while sometimes a short-wavelength infrared domain (1.4 - 3 µm) is additionally defined [68]. Chalcogenide fibers [52], [69], [70], tellurite fibers [54], [71], and fluoride fibers [72]–[77] are used for mid infrared SCG due to their wide transmission windows and high nonlinearity. Especially broad supercontinua were re-

ported in chalcogenide step-index fiber spanning 1.4-13.3 µm [52], and 2.0 - 15.1 µm [70]. To scale the nonlinear effects, the intensity of the laser beam propagating through the nonlinear optical fiber can be increased by reducing the effective mode area [28], [78].

Waveguides with curved group velocity dispersion

Reducing the effective mode area typically has also the effect that the guided modes are stronger confined in the core. This can lead to a curved group velocity dispersion profile, which has a spectrally restricted, flat AD regime, and enables soliton-based generation of new frequencies, so-called dispersive waves (DWs) in the normal dispersive domains at the short-wavelength and long-wavelength side [30]. In this way dual DW generation broadens the spectrum towards the short-wavelength and long-wavelength domain. In contrast, if the AD regime is not limited at the long-wavelength side, DWs are only generated at the short-wavelength side. The absence of long-wavelength DWs strongly reduces the broadening towards longer wavelength, which is consequently only caused by the redshift of the solitons [79]. To obtain dual DW generation in flat AD regimes microstructured fibers with complex cross section profiles are developed [39], [80] and sometimes even additionally tapered to obtain maximum spectral bandwidths [53]. Exciting higher-order modes (HOMs) in liquid-core step-index fibers (LCFs) with a strong refractive index contrast allows to obtain curved dispersion profiles for moderate core sizes of around 4 µm [79], [81]. For these plain and highly symmetric fiber structures semi-analytical models can be used to calculate the group velocity dispersion and the manufacturing process is less complicated compared to microstructured fibers.

Tunable wavelength conversion in hollow core fibers

Besides aiming for maximum bandwidths, some applications require high power density in selected wavelength intervals, e.g. matching the absorption bands of fluorescence [82] or Raman scattering [83]. Instead of suppressing unwanted wavelengths with optical filters, it is more efficient in terms of energy consumption to optimize the output spectrum for the desired wavelength bands. Tuning of the wavelengths generated in nonlinear waveguides can be either achieved via adapting the laser [84], [85] or the waveguide itself [86]. Wavelength tuning of supercontinuum spectra via laser adjustment has been shown via: a) scaling the laser power e.g. of Raman shifts [71], [75], [87], b) shifting the pump wavelength [51], [85], [88]–[91], c) modifications of the pump pulse duration [92], and d) adaption of the polarization of the laser beam in case non-axially symmetric fibers [86], [93]–[96]. Effects on the nonlinear output spectrum by modifying the waveguide have been experimentally demonstrated via adapting its length [97], [98], changing its material [77] and modifying its cross section. The latter was realized by either switching between different core sizes [81], [99], [100], or changing the complex design of microstructured fibers [101], e.g. by varying the pitch sizes between holes

in the cladding [39]. Furthermore, coating added close to the core of an exposed core fiber was demonstrated to lead to controllable changes of the fiber output wavelength [86], [102]. All these methods either require the exchange of the waveguides or evolve irreversible modifications of them.

Hollow-core waveguides, whose core can be filled via a gas or liquid, offer the opportunity to modify the optical properties of the core more flexibly, e.g. by exchanging the filling core material [103], by using material mixtures with different concentration ratios [104], [105], and by changing the pressure in the core [106]–[108]. All these processes are reversible and do not necessarily require to remove the fiber from the setup, which allows to keep the light coupling conditions unchanged while modifying the optical properties of the fiber. In case of solid-core microstructured fibers reversible spectral changes can be obtained via pressure tuning of the gas infiltrated into the holes surrounding the core [109].

Thermal tuning of liquid-core step-index fibers

Liquid-core step-index fibers (LCFs) are capillary fibers with one central hole that is filled with liquids. These fibers profit from the before-mentioned tuning capabilities of hollow-core fibers and can yield even stronger nonlinear effects, when filled with highly nonlinear solvents, like carbon disulfide (CS_2), tetrachloroethylene or carbon tetrachloride. LCFs are prominent candidates for another dynamical tuning technique, the thermal tuning. Due to their strong thermo-optical coefficients [110] that are of the same order of magnitude ($10^{-4}\,K^{-1}$) as those of semiconductors [111], significant spectral shifts are expected for moderate temperature changes in LCFs [112]. So far thermal sensors were realized with hollow-core fibers by analyzing the spectral broadening of the output spectrum [113] and the spectral shift of generated solitons [114]. Thermal tuning of four-wave mixing was experimentally demonstrated in three different microstructured optical fibers [115]–[117], as well as in ethanol-filled photonic crystal fibers (PCFs) [118], the latter showing an average thermal shift of 13.5 nm/K, while the previous experimental demonstrations did not reach tuning-slopes above 4 nm/K. Small temperature-induced modifications of SCG (< 1 nm/K) were experimentally demonstrated in a nonzero dispersion shifted fiber by Martin-Lopez et al. in 2006 pumping in small AD [119]. Simulations with LCFs and liquid-core PCFs promise similar thermal tuning slopes of supercontinuum spectra of up to 2 nm/K [112], [120], [121]. Numerical simulations of a modulation instability-based temperature sensor by Nallusamy et al. suggested huge tuning slopes of 435 nm/K for infrared Anti-Stokes lines in CS_2-core PCFs [122].

Another promising feature of thermally-controlled LCFs is the additional degree of freedom to modify their temperature along the fiber length. In gas-core fibers continuously increasing and decreasing pressure gradients are used to optimize supercontinuum spectra [123]–[126]. The longitudinal pressure control allows to fine-tune the optical properties and to increase the bandwidth, e.g. spanning from 200 nm to 1.7 μm in a dispersion

decreasing gas-filled microstructured fiber [127]. Complex step-wise dispersion gradients cannot be implemented by pressure tuning, which is restricted to monotonically changing profiles. In contrast, beside continuously decreasing dispersion profiles, also discrete dispersion steps and highly complex dispersion profiles can be applied via temperature control to thermally-sensitive waveguides, e.g. LCFs.

Longitudinal dispersion management is often realized via longitudinal modifications of the waveguide dimensions [58], [128]–[130]. Tapering of fibers is a common method to reduce their core sizes at desired fiber sections. This leads to improved SCG in the fiber sections of reduced dispersion [35], [36], [131]–[134]. Continuously or step-wise dispersion decreasing fibers also enable optimized bandwidth of supercontinua [34], [135]–[143]. Varying the core-size periodically yields dispersion oscillating fibers [80], [144]–[147] and waveguides [130], [148], [149], which show increased spectral bandwidths e.g. via cascaded DW generation [145]–[148] or via sign-alternating dispersion evolutions [149]. Spatially varying the core size along the waveguide or fiber requires precise control during the fabrication and/or post-processing procedure [150] and again represents an irreversible tuning process. In contrast, a temperature profile applied to a thermally sensitive LCF can be modified at any time so that different dispersion landscapes can be realized with one and the same fiber [121].

In 2018 Chemnitz et al. published an experimental evidence of thermally tuned SCG in LCFs. Soliton-based SCG is modified by partly heating a CS_2-core step-index fiber. Studying the output spectrum of the fundamental mode, which shows a continuously extended AD regime towards longer wavelengths, a short-wavelength DW is tuned by $3.5\,\text{nm/K}$ [79]. My contribution to this publication is a first experimental demonstration of thermally tuned SCG using higher-order modes. These modes have a flat and spectrally restricted AD regime in the used CS_2-core step-index fiber, which leads to the generation of a long-wavelength DW that shows a significantly stronger tuning slope of up to $15\,\text{nm/K}$. These results, set the basis for further investigations of the thermal tuning of SCG in CS_2-core step-index fibers using higher-order modes with curved GVD profiles.

Content of this work

In this doctoral thesis on hand the thermal tuning of SCG of higher-order modes in CS_2-core fibers is investigated using ultrashort pulses with a pulse duration smaller than $40\,\text{fs}$, and a center wavelength of $1570\,\text{nm}$. The core diameter is varied between $3.5\,\mu\text{m}$ and $4.0\,\mu\text{m}$ and the higher-order TE_{01} and TM_{01} modes are excited to obtain soliton-driven SCG in systems with curved group velocity dispersion. The influence of temperature on the soliton dynamics and on the generation of short- and long-wavelength DWs is studied experimentally by evaluating the output spectra obtained when applying different temperatures at a fixed fiber section. In addition, the spectral broadening is investigated when applying constant temperatures to fiber sections with varying lengths

or longitudinally shifting starting positions. It is shown that a manifold of different soliton dynamics leading to dual DW generation can be obtained in CS_2-core step-index fibers: Soliton fission, soliton breathing, soliton breakdown, and soliton tunneling are experimentally demonstrated and tuned via temperature changes. To obtain the different soliton effects, the GVD is carefully adjusted by choosing a suitable fiber core diameter and temperature range. Switching between different soliton dynamics is realized via thermal control. All experimental results are compared with numerical simulations solving the generalized nonlinear Schrödinger equation (GNLSE). In addition, these simulation results are evaluated along the propagation length to learn more about the spectral and temporal dynamics of the ultrashort pulses inside the fiber.

One of the main achievements of this thesis is that strong spectral shifts of up to $33\,\mathrm{nm/K}$ are demonstrated via temperature-controlled DW generation. The experimental results showing these strong thermo-spectral shifts are in good agreement with simulations solving the GNLSE and calculations of the corresponding phase matching conditions. Soliton breakdown is experimentally controlled by thermally reducing the width of the anomalous dispersive region. It leads to the generation of additional DWs, whose spatial and spectral onset can be controlled by the applied temperature step. A temperature-induced transition from flat AD to all-ND is realized leading to increased conversion efficiencies from solitons that break down when the dispersion becomes ND to wavelength in the normal dispersive domain. Modifying the length of a heated fiber section, the local and temporal offset between two soliton fission processes is tuned in experiments and simulations. Simulations supporting nonlinear experiments show how additional DWs are generated when a soliton is temporal recompressed after tunneling through a fiber section with ND. Overall it is shown that post-fission tuning, e.g. via temperature-assisted soliton breakdown, has a significant effect on the generated output spectra.

In conclusion, this work gives experimental evidence that soliton-based SCG can be strongly tuned by temperature. Exciting higher-order modes in LCFs thermally induced modifications of the group velocity dispersion give precise control over the soliton dynamics within the fiber. In this way, the output spectrum can be tailored to match different applications. Additionally, soliton dynamics can be precisely controlled to increase the understanding of nonlinear processes and to test new systems such as quasi-phase matching with different grating periods in LCFs.

Structure of this work

This thesis is structured in the following way: Chapter 1 is the introduction at hand. To set the theoretic basis, a brief introduction to fiber optics and soliton-based SCG is provided in Chapter 2, followed by a summary of the material properties of the core-liquid carbon disulfide in Chapter 3. In Chapter 4, the preparation of LCFs, the experimental setup and the used numerical solver for the GNLSE are explained. After these preparing chapters the dependence of the GVD of higher-order modes in CS_2-core fibers on

core diameter and fiber temperature are studied via detailed calculations in Chapter 5. The optimal core diameters to obtain curved GVD profiles for dual DW generation in the TE_{01} and TM_{01} mode are obtained from the calculated GVD itself and phase matching conditions between soliton and DWs. Furthermore, the influence of temperature changes on the GVD and the phase matching to both DWs is investigated. In this context the physical origin of bent GVD profiles is explained and thermal limitations of the experimental setup are discussed. In Chapter 6, simulation results solving the GNLSE demonstrate the manifold soliton dynamics attainable for higher-order modes in CS_2-core fibers using different core dimensions and applying different temperature steps. The numerical simulations provide a better understanding of the physical processes taking place inside the fiber and additional parameter studies are conducted to find the optimum and limits of individual effects. In Chapter 7 experimental results demonstrate that soliton dynamics can be controlled via modifications of the fiber temperature resulting in different output spectra. Experimental and numerical results further prove that it is possible to switch between different soliton dynamics by changing the temperature. After studying the influence of different temperatures in a fixed fiber section, a constant temperature is applied to fiber sections of different lengths and shifting starting positions. Soliton dynamics and dual DW generation are experimentally detected and evaluated comparing them with numerical simulations which give detailed insights into the dynamics taking place inside the fiber. In this way soliton fission, soliton breathing, soliton breakdown, and soliton tunneling are investigated. This work is concluded in Chapter 8, and gives an outlook to further developments of this study, as well as to future applications in Chapter 9.

2 Theory of fiber-based supercontinuum generation

This chapter introduces the basics of guided modes in step-index fibers and gives insights to the theory behind soliton-based SCG. It is not supposed to give a complete summary of this topic, but focuses on the fundamentals needed for the analysis of the numerical and experimental studies conducted in this work.

2.1   Fiber optics

Light guidance in optical fibers benefits from the strong confinement of light in the fiber core [28] and the low losses for km-long fiber lengths. This makes optical fibers very useful for telecommunication. Furthermore, optical fibers are for example used to build laser sources, to spectrally and temporally modify optical pulses, and to build optical sensors. In this chapter the basic principle of light guidance in step-index fibers, a comparison with different fiber types, and the properties of guided modes are explained.

2.1.1   Guidance of light in optical fibers

From the first discovery of guiding light in water jets by Daniel Colladon in 1841 [151], [152] until the development of optical fibers with losses less than 0.2 dB/km in 1979 [153] the working principle remained the same: the light is guided in the core via total internal reflection. Therefore the core needs to have a refractive index n_{co} higher than the refractive index of the surrounding medium n_{cl}, which can be air or any other low refractive index material, commonly called cladding. Until today, commonly used optical fibers, e.g. the single mode fiber SMF28, consist of a high refractive index core surrounded by a low refractive index cladding, see figure 2.1 (a). To protect the fibers mechanically they are additionally covered with a polymer layer, called coating. Due to the step-wise increase of the refractive index between core and cladding, these fibers are called step-index fibers. Besides that, many different new fiber types have been developed in the past decades: Graded-index fibers having a continuous transition from the high refractive index core to the low refractive index cladding (figure 2.1 (b)), fiber with especially doped cores optimized for lasing, and a large variety of microstructured fibers, which can be classified by their guiding mechanisms [154], see figure 2.1 (c-f).

A first type of microstructured fibers is based on total internal reflection having a solid core surrounded by an air hole structure that effectively reduces the refractive index of the cladding, e.g. suspended-core fibers (c) [155], and solid-core Photonic crystal fibers (PCFs) (d) [156]. A second type is based on anti-resonant guiding (also called inhibited coupling), e.g. anti-resonant revolver hollow-core fibers (e) [157]. A third type is based on photonic bandgap guiding, e.g. hollow-core photonic bandgap fibers (f) [154], [158]. Some kind of PCFs are known to be endlessly single-mode [159]. The design of optical fibers can be optimized so that their properties match the targeted applications. Especially microstructured optical fibers have additional degrees of freedom regarding the
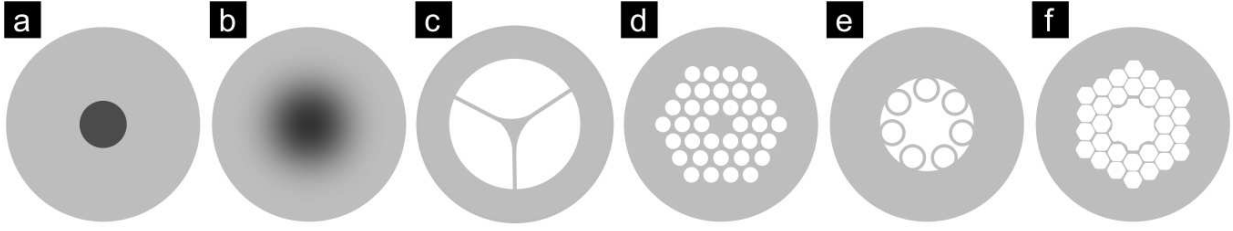
Figure 2.1: **Overview of different fiber types.** a) Step-index fiber, b) graded-index fiber, c) suspended-core fiber, d) solid-core photonic crystal fiber (PCF), e) anti-resonant (revolver) hollow-core fiber, f) hollow-core photonic bandgap fiber. White areas are air-filled regions, light gray areas represent glass, and dark gray regions glass with a comparably higher refractive index.

design of their cross section.

This work focuses on step-index fibers. The guidance of light in step-index fibers can be explained by ray optics. Total internal reflection at the interface between core and cladding is only possible when the reflection angle in the fiber is larger than the critical angle $\theta_c = \arcsin(n_{\mathrm{cl}}/n_{\mathrm{co}})$ [160]. For optical rays entering the fiber from a medium of refractive index n_0 this corresponds to an input angle smaller than the maximal acceptance angle $\theta_{\max} = \arcsin\left(\sqrt{n_{\mathrm{co}}^2 - n_{\mathrm{cl}}^2}/n_0\right)$. The numerical aperture NA is defined as $\mathrm{NA} = n_0 \cdot \sin(\theta_{\max}) = \sqrt{n_{\mathrm{co}}^2 - n_{\mathrm{cl}}^2}$ and describes the acceptance cone of the fiber in dimensionless units. The waveguide parameter V includes the wavelength of the light λ and the radius of the fiber core r_{co} [160]

$$V = 2\pi r_{\mathrm{co}}/\lambda \cdot \mathrm{NA}. \tag{2.1}$$

If the waveguide parameter fulfills V > 1, guidance in the fiber core is possible; if $V \gg 1$, many different modes are guided in the fiber.
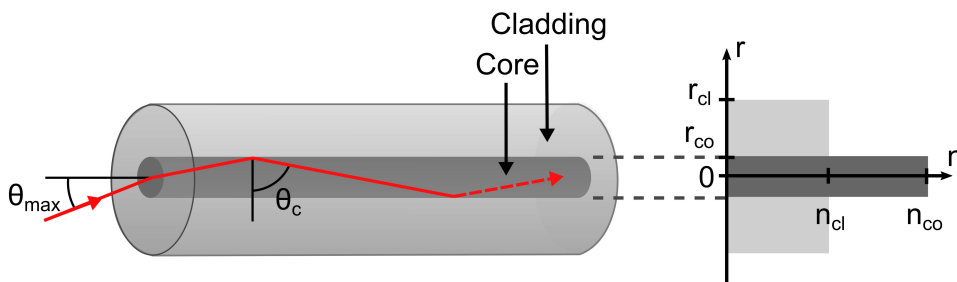
Figure 2.2: **Total internal reflection and refractive index profile of a step-index fiber.** Schematic showing the maximal acceptance angle $\theta_{\max}$, and the critical angle θ_c for a step-index fiber with a refractive index profile n(r) in dependence of the radial coordinate r.

2.1.2   Guided modes

The geometry and material composition of an optical fiber determines the discrete set of electromagnetic fields guided in the fiber, which are called fiber modes. One

distinguishes single-mode fibers that have a comparatively small core and low refractive index difference, and multi-mode optical fibers that have comparatively large cores and huge refractive index difference between core and cladding, see V parameter definition in equation 2.1. Each mode has a different propagation constant β in the fiber, which can be correlated to an effective refractive index $n_{\mathrm{eff}} = \beta/2\pi \cdot \lambda$ of the mode in the fiber. Propagation constant and effective refractive index of the modes depend on the wavelength λ and can be calculated using the Maxwell's equations taking into account the symmetry of the waveguide and its boundary conditions, as explained in the book 'Optical Waveguide Theory' by A. W. Snyder and J. D. Love [160]:

The z-components of the longitudinally propagating electric fields $E_z(r, \Phi)$ and magnetic fields $H_z(r, \Phi)$ are defined in polar coordinates (r,Φ). They fulfill the scalar wave equation (Helmholtz equation):

$$(\nabla_t^2 + n^2 k_0^2 - \beta^2)\Psi = 0, \tag{2.2}$$

and are represented by $\Psi = (E_z, H_z)$. ∇_t represents the transverse derivatives, and $k_0 = 2\pi/\lambda$ the wave number. The propagation constant β is the eigenvalue of this equation. So called modal parameters are introduced in dependence of the normalized radius $\rho = r/r_{\mathrm{co}}$:

$$\text{core parameter } U = \rho\sqrt{k^2 n_{\mathrm{co}}^2 - \beta^2}, \quad \text{cladding parameter } W = \rho\sqrt{\beta^2 - k^2 n_{\mathrm{cl}}^2}, \tag{2.3}$$

$$\text{waveguide parameter } V^2 = U^2 + W^2, \quad \text{and height parameter } \Delta = \frac{n_{\mathrm{co}}^2 - n_{\mathrm{cl}}^2}{2 n_{\mathrm{co}}^2} \tag{2.4}$$

Further following the derivation by A. W. Snyder and J. D. Love [160] the wave equations in the core and cladding can be written as :

$$\left(\frac{\partial^2}{\partial \rho^2} + \frac{1}{\rho}\frac{\partial}{\partial \rho} + \frac{1}{\rho^2}\frac{\partial^2}{\partial \Phi^2}\right)\Psi = \begin{cases} -U^2 \cdot \Psi & \text{for } 0 \leq \rho < 1 \\ +W^2 \cdot \Psi & \text{for } 1 \leq \rho < \infty. \end{cases} \tag{2.5}$$

Separable solutions of the modes include Bessel functions of the first order $J_\nu(U)$ in the core and of the second-order $K_\nu(W)$ in the cladding, as well as their first-order derivatives with respect to the radial coordinate ρ denoted as $J_\nu'(U)$ and $K_\nu'(W)$. Accordingly, the dispersion relation of bound $\mathrm{HE}_{\nu m}$ modes of the ν-th order in a step-index fiber can be written as:

$$\underbrace{\left(\frac{J_\nu'(U)}{U J_\nu(U)} + \frac{K_\nu'(W)}{W K_\nu(W)}\right)}_{\nu=0:\ \mathrm{TE}_{0m}\ \text{mode}} \cdot \underbrace{\left(\frac{J_\nu'(U)}{U J_\nu(U)} + \frac{n_{\mathrm{cl}}^2}{n_{\mathrm{co}}^2}\frac{K_\nu'(W)}{W K_\nu(W)}\right)}_{\nu=0:\ \mathrm{TM}_{0m}\ \text{mode}} = \left(\frac{\nu\beta}{k n_{\mathrm{co}}}\right)^2 \left(\frac{V}{UW}\right)^4, \tag{2.6}$$

where the second index m describes the m-th root of the dispersion equation [160]. Solving the dispersion relation enables to calculate the propagation constant β and the

effective refractive index n_{eff} of each guided mode from the core parameter U and the cladding parameter W:

$$\beta = \frac{1}{\rho}\sqrt{\frac{V^2}{2\Delta} - U^2} = \frac{2\pi}{\lambda} \cdot n_{\text{eff}}. \tag{2.7}$$

In case of TE_{0m}, and TM_{0m} modes only the respectively labeled terms of the dispersion relation 2.6 need to be solved.
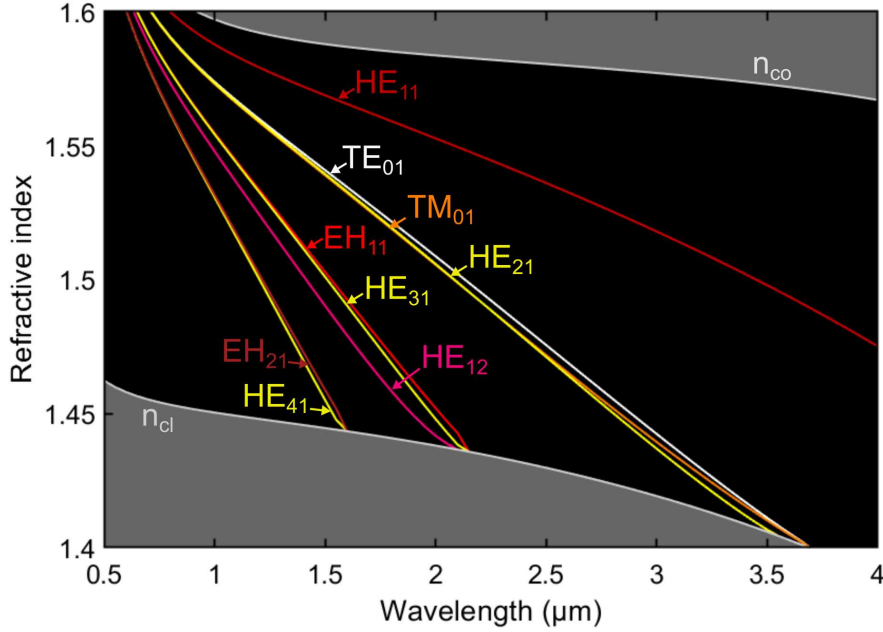
Figure 2.3: **Effective refractive indices of modes guided in a 4 μm CS$_2$-core fiber.** The gray lines represent the refractive indices n_{co}, and n_{cl} of the bulk core material CS$_2$, and the cladding material fused silica. Modal cutoff is reached when the effective refractive index equals the refractive index of the cladding material.

The effective refractive indices of guided modes n_{eff} lie in between the refractive indices of the cladding and the core material: $n_{\text{cl}} < n_{\text{eff}} < n_{\text{co}}$. It approaches the cladding index for increasing wavelengths, see figure 2.3. When n_{eff} matches the refractive index of the cladding the corresponding mode is not guided in the core any more. In this figure n_{eff} is calculated for different higher-order modes of a CS$_2$-core fiber with a core diameter of 4.0 μm surrounded by an infinite silica cladding. If the wavelength increases, less higher-order modes are guided, until above 3.7 μm the fiber becomes single-mode and only guides the fundamental mode HE_{11}.

The electric and magnetic fields of the guided modes can be calculated from the core parameter U and the cladding parameter W [160]. Figure 2.4 shows the calculated intensity distribution corresponding to the modes with the effective refractive indices shown in figure 2.3. The black arrows indicate the local polarization states at a fixed point in time. Comparing ring-shaped higher-order modes, their intensity becomes less concentrated in the central fiber region with increasing mode order. Consequently, higher-order modes that are closer to the cladding, are stronger influenced by changes of the core diameter in comparison to the fundamental mode HE_{11}.
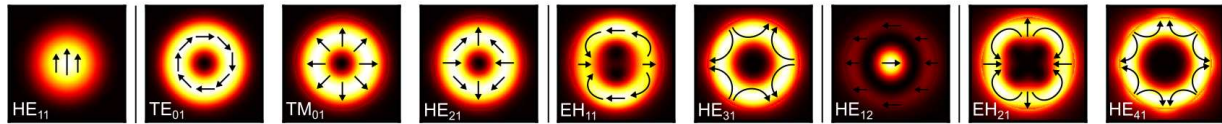
Figure 2.4: **Intensity distribution and polarization of modes guided in a 4 μm CS$_2$-core fiber.** The same modes are chosen as in figure 2.3. The black arrows indicate the polarization distribution at a fixed point in time. Each intensity profile is plotted in linear scale and normalized to its own maximum.

2.2 Supercontinuum generation

Supercontinuum generation describes the strong spectral broadening of initially spectrally narrow optical pulses, which is typically obtained in highly nonlinear waveguides. The first supercontinuum was reported by Alfano and Shapiro 1970 in macroscopic pieces of glass [161]. Until today many especially designed PCFs have been developed to further extend the generated supercontinua [30], [162], e.g. towards mid infrared wavelengths [56]. Broadband mid infrared ($3 - 20\,\mu$m) sources are of special interest for spectroscopic applications [163], [164] due to the characteristic vibrational transitions of molecules in this spectral ('fingerprint') region. The bandwidth of supercontinuum spectra is sometimes given in octaves. A spectrum covering one octave, spreads from its lowest edge at frequency $f_a = c_0/\lambda_a$ to the doubled frequency $2 \cdot f_a$. Besides their extended bandwidths, supercontinuum sources are also highly requested due to their low noise and high coherence properties, which makes them suitable for optical coherence tomography [64], [165]–[170], and optical frequency metrology [99], [171]–[173]. Further applications of supercontinuum sources can be found in optical telecommunication [65], [174], and microscopy [63], [175], [176].

SCG is caused by different nonlinear effects. Which effects are dominating the complex nonlinear broadening process, depends on the pulse parameters of the pump source, as well as on the properties of the nonlinear medium [28]. Furthermore, the properties of the guided mode in the waveguide, e.g. the group velocity dispersion, plays a crucial role for SCG. This chapter explains the importance of the group velocity dispersion parameter on various SCG dynamics. In particular, soliton-driven SCG is discussed, which is the broadening mechanism relevant in this work.

2.2.1 Group velocity dispersion and pulse parameters

Pump power, pulse duration, pulse wavelength, and waveguide properties (e.g. material composition and geometry) play a crucial role determining the nonlinear dynamics of optical pulses propagating in a fiber [28]. Nonlinear dynamics are dominating the wavelength conversion processes in case of ultrashort pulses with pulse durations of the order of a picosecond or less. The group velocity dispersion (GVD), which is defined as the second derivative of the propagation constant β: $\beta_2 = d^2\beta/d\omega_0^2$, is commonly used

to differentiate various nonlinear broadening regimes [79]. The frequently used group velocity dispersion parameter

$$D = -\frac{2\pi c_0}{\lambda^2} \cdot \beta_2 = \frac{-\lambda}{c_0} \cdot \frac{d^2 n_{\text{eff}}}{d\lambda^2} \tag{2.8}$$

can be calculated for different wavelengths λ from the effective refractive index n_{eff}, using the definition of the propagation constant β in equation 2.7. The dispersion length $L_D = T_0^2/|\beta_2|$ combines the impact of the group velocity dispersion and the pulse width T_0, indicating that a shorter dispersive length (equal to unchanged dispersion on a shorter length scale) is obtained for either stronger group velocity dispersion or shorter pulse duration [30].

If the group velocity dispersion (GVD) and its parameter D vanishes, there is supposed to be no dispersion of the group velocity. For a given mode and fiber this is typically only the case for one or two distinct wavelengths, called zero dispersion wavelengths (ZDW)s. When pumping close to these ZDWs, the nonlinear dynamics dominate over the dispersion of the pulse, and strong spectral broadening can be expected in case of sufficient peak power [28]. The ZDWs separate the normal group velocity dispersion regime (in the following called normal dispersion (ND) regime) from the anomalous group velocity dispersion regime (called anomalous dispersion (AD) regime). If a pulse propagates through a material with

- positive GVD (negative D parameter, ND regime): shorter-wavelength components travel slower than the longer-wavelength components, and the pulse becomes positively chirped (up-chirped), increasing in frequency with time.
- negative GVD (positive D parameter, AD regime): shorter-wavelength components travel faster than the longer-wavelength components, and the pulse becomes negatively chirped (down-chirped), decreasing in frequency with time [28].

Anomalous dispersion is especially interesting because it allows to cancel the positive chirp applied by nonlinear effects (e.g. self-phase modulation) [177]. This allows to obtain temporally stable pulses, called solitary waves or optical solitons, which are explained in more details later. A ZDW is obtained at a wavelength, where the material dispersion is completely compensated by the waveguide dispersion [156], [178]. The material dispersion can be modified by changing the core material (e.g. using liquids or soft glasses with high refractive indices as core material [104], [179]) or by adding dopants [28], [180]. The waveguide dispersion can be adapted by changing the waveguide dimensions e.g. the core radius. If the diameter of the hole fiber is reduced over a certain distance, this is called tapering [181]. Furthermore, the waveguide dispersion can be modified by exciting different higher-order modes [81], or by increasing the refractive index difference between core and cladding. The latter one can be achieved by adding air holes around the core, as it is done in suspended core fibers [43] or PCFs [156], shown in figure 2.1 (c,d). Standard fibers have one ZDW separating an ND regime

at short-wavelength from an AD regime at longer wavelengths. In specially designed waveguide systems it is possible to obtain GVD with two or more ZDWs [30]. In this work, systems with two ZDWs are investigated. In that case an AD regime is enclosed between two ND regimes leading to restricted soliton redshifts and additional DW generation to the long-wavelength side [182]. In case of several ZDWs also ND regimes can be spectrally enclosed between AD regimes and soliton tunneling from one AD regime to the other can be observed [183].

Pulse parameters influencing the nonlinear and dispersive dynamics in the fiber are the pulse duration, temporal pulse shape, initial temporal chirp, spectral bandwidth, center wavelength, and peak power at the input of the fiber. They are part of the complex interplay of several nonlinear effects and should be ideally determined at the fiber input. The material absorption of the fiber can additionally reduce the peak power and thus limit nonlinear effect during the propagation of the pulse. The pulse energy, which can be calculated from the average power divided by the repetition rate of the laser source, should not be too high, because otherwise fiber damages will be induced, especially at the fiber input [103].

2.2.2 Broadening mechanisms of supercontinuum generation

Coupling multi-watt beams in long optical fibers of at least several meter lengths, SCG is possible with continuous-wave (CW) pump beams [101].

When pumping with long pulses in the picosecond or nanosecond scale, less average pump power and shorter fiber lengths are sufficient for SCG [184]. One distinguishes the case of ND, where the spectral broadening is dominated by Raman scattering or four-wave mixing, and the case of anomalous GVD, where modulation instability dominates [185]. Modulation instability relies on a power dependent phase shift, which varies along the pulse and leads to the generation of new frequencies at two spectral sidebands [28]. It can also cause CW beams to split-up into pulse trains [186], whose repetition rate can be externally controlled [187].

Using ultrashort femtosecond pulses, SCG is dominantly initiated by self-phase modulation [30]. In the AD regime, the balancing of self-phase modulation and dispersion can lead to complex soliton dynamics, including the split-up of higher-order solitons into multiple fundamental solitons (soliton fission) and the energy transfer to phase-matched DWs in the ND regime [28]. For sufficiently high peak power of the pulse and nonlinearity of the medium, short fiber lengths of less than 1 m and average pump powers below 1 Watt can induce strong spectral broadening [185]. This soliton-fission based broadening mechanism is the key effect studied in this thesis. It is explained in more details in the next section.

2.2.3   Soliton-driven supercontinuum generation

When optical pulses propagate though a fiber nonlinear effects as well as normal dispersion generally induce temporal broadening of the pulse leading to a fast decay of its peak power [28]. This drastically reduces the nonlinear effects and thus the spectral broadening. In AD regimes the positive chirp induced by nonlinear effects (e.g. by self-phase modulation) can be compensated by the anomalous dispersion, so that temporally stable solitary waves (in the following called solitons) propagate along the fiber. Maintaining a high peak power the soliton pulse continually experiences strong nonlinear effects, which can lead to further temporal compression and spectral broadening, followed by efficient energy transfer to phase-matched wavelengths called dispersive waves (DWs), see figure 2.5.
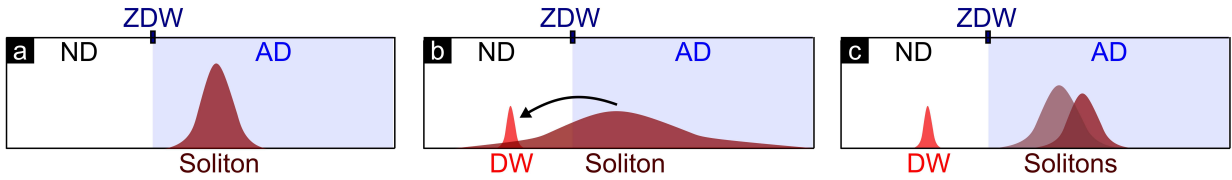
Figure 2.5: Scheme of soliton-fission based dispersive wave generation in a system with one zero-dispersion wavelength (ZDW). (a) Higher-order soliton (dark red) as starting position. (b) Spectral broadening of the soliton due to temporal compression, and transfer of energy to a dispersive wave (DW, red). (c) Split-off fundamental soliton (dark red) and reduced higher-order soliton (red-gray) after soliton fission. The anomalous dispersion (AD) domain is highlighted in blue, the normal dispersion (ND) domain is white. The horizontal axes correspond to wavelengths, and the vertical ones to intensity.

Initial spectral broadening by self-phase modulation

Self-phase modulation, which leads to symmetric spectral broadening of optical pulses, is caused by the nonlinear Kerr effect. It is based on the dependence of the refractive index on the pulse intensity in nonlinear optical media [28]. The intensity-dependent refractive index $\tilde{n} = n + n_2 I$ can be calculated from the power-independent refractive index n, the intensity I, and the nonlinear index coefficient n_2 (also called Kerr parameter), which is proportional to the real part of the third-order susceptibility $\chi^{(3)}_{xxxx}$. The nonlinear length $L_{\text{NL}} = 1/(\gamma_0 P_0)$ is the distance over which the nonlinear phase shifts by 1 rad for a peak power P_0. The nonlinear parameter γ_0 relevant for nonlinear pulse propagation equations is defined as

$$\gamma_0 = \gamma(\omega_0) = \frac{\omega_0 n_2}{c_0 A_{\text{eff}}} \text{ , with } A_{\text{eff}} = \frac{(\iint_{-\infty}^{\infty} |F(x,y)|^2 dx dy)^2}{\iint_{-\infty}^{\infty} |F(x,y)|^4 dx dy} \tag{2.9}$$

being the effective mode area of the fiber for the modal distribution $F(x,y)$ of the investigated mode [28]. Increasing the nonlinear Kerr parameter n_2 and decreasing the effective mode area A_{eff} leads to an increase of the nonlinear parameter γ_0.

Optical solitons and soliton fission in nonlinear fiber optics

In 1973 Hasegawa and Tappert first postulated that the 'nonlinearity of the index of refraction could be used to compensate the pulse broadening effect of dispersion in low-loss optical fibers' [31]. In fiber optics these stable pulses are called solitary waves or solitons, and were first experimentally demonstrated in a fiber with AD by Mollenauer et al in 1980. They stated that in comparison to fundamental solitons, which propagate without distortion, 'solitons of higher order than the fundamental are self-maintaining in the sense that their pulse shapes are periodic with propagation' [32]. Therefore the higher-order solitons are sometimes referred to as optical breathers.

Fundamental and higher-order solitons are analytic solutions of the GNLSE [177]. For a mathematical derivation please refer to chapter 5 of the book Nonlinear fiber optics [28]. In optical fibers the stable propagation of higher-order solitons can be disturbed by the nonlinear Raman effect or higher-order dispersion terms, e.g. third-order dispersion, which act as perturbations of the system [188], [189]. In the LCFs studied here, the higher-order dispersion terms act as perturbations. This leads to the split-off of higher-order solitons to several fundamental solitons, a process that is called soliton fission [190]. The number of the generated fundamental solitons typically equals the next smaller integer of the so called soliton order N of the initially excited soliton. The soliton order depends on pulse and fiber parameters, and is defined by the fraction of the dispersive length L_D and the nonlinear length L_{NL} [28]:

$$N^2 = L_D / N_{NL} = \frac{T_0^2 \gamma_0 P_0}{|\beta_2|}. \tag{2.10}$$

The distance at which the soliton fission occurs generally corresponds to the point at which the initial higher-order soliton is maximally broadened. This distance can be estimated by the fission length $L_{fiss} \approx L_D / N$ [30]. In the following presented studies with HOMs in LCFs this approximation did not match the fission points obtained in the pulse evolution simulations. It was shown that this distance also depends on the input pulse chirp [191], which is not known here.

The fission of higher-order solitons to several fundamental solitons is typically accompanied by a significant energy transfer from the soliton in the AD regime to phase-matched wavelengths in the ND regime, see figure 2.5 b): This was first analytically shown by Akhmediev and Karlsson in 1995 [189], and experimentally proven by Husakou and Herrmann in 2001 using a PCF [192]. The newly generated frequencies are called dispersive waves (DWs), resonant radiation or Cherenkov radiation [30].

Dispersive wave generation and phase matching

To efficiently transfer energy from a soliton to DWs during soliton fission, the spectrally broadened soliton needs to have a significantly strong spectral overlap with the DWs.

The wavelength of the DW $\lambda_{DW} = 2\pi c_0/\omega_{DW}$ can be determined by the following phase matching equation [28]:

$$\beta(\omega) = \beta(\omega_S) + (\omega - \omega_S)\left(\frac{d\beta}{d\omega}\right)_{\omega_S} + \frac{1}{2}\gamma_0 P_S \tag{2.11}$$

The angular frequency ω for which the phase matching condition is fulfilled corresponds to the wavelength of the DW. To obtain this wavelength the propagation constant β and its first derivative are evaluated at the soliton frequency ω_S. The nonlinear phase, which depends on the nonlinear coefficient γ_0 and the peak power P_S of the ejected soliton is highlighted in gray. The peak power of the first split-off soliton

$$P_S = P_p \cdot (2N - 1)^2/N^2 \tag{2.12}$$

can be estimated from the soliton number N and the initial peak power of the soliton P_p [30]. Because the actual peak power of the solitons can not be determined from the conducted experiments, the phase matching conditions with and without nonlinear term are both displayed in this work.

Soliton dynamics in fiber systems with two ZDWs

In case the GVD has two ZDWs, and the soliton is excited in the central AD regime, phase matching can be obtained at two wavelengths, one in the short-wavelength ND regime and one in the long-wavelength ND regime, see equation 2.11. This allows to efficiently transfer energy to one DW at each side of the spectrum, which extends the spectra to shorter and longer wavelengths simultaneously [37], [182]. In case of two ZDWs the slope of the GVD parameter $dD/d\lambda$ is negative around the second ZDW, and the same applies for the third-order dispersion β_3. Consequently, such fibers are described as having a negative dispersion slope in this wavelength domain [30]. This can lead to periodic breathing of solitons in waveguides with two ZDWs [191]. Further-more, the negative dispersion slope can induce a recoil effect on the soliton during the fission process [193]: when DWs are emitted to the long-wavelength side, the soliton is observed to be shifted towards shorter wavelengths in special PCFs [194]. In most fiber systems a redshift of the soliton is observed with increasing propagation distance. In many solid-core fibers a continuous redshift is caused by the Raman induced soliton self frequency shift [195]–[198]. On one hand, solitons reaching the second ZDWs can be hindered to further redshift. This is often referred to as soliton trapping [199]. On the other hand, solitons approaching the second ZDW can also transfer almost all of their energy to phase-matched DWs. This is called soliton breakdown and happens more frequently in waveguides with very close ZDWs [41], [42], [200], [201]. In general two or more ZDWs can be obtained when a bent waveguide dispersion is dominating over the continuously increasing material dispersion curve [202]. This can be for example obtained in tapered fibers[37], [40], [49], PCFs [194], [203], dispersion-modified single

mode fibers [204], and LCFs using higher-order modes [205]. The latter case will be discussed in more detail in the simulation chapter 6. In general, the bending of the waveguide dispersion strongly influences the spectral position of the second ZDW, which makes the generation of the long-wavelength DWs more sensitive on the core diameter and temperature compared to the first ZDW, which almost remains constant.

In summary, different types of optical fibers, and especially the guidance of modes in step-index fibers are introduced. The GVD parameter is discussed being a key parameter distinguishing different SCG mechanisms in general and tuning soliton-driven SCG in particular.

3 Material studies of the core liquid carbon disulfide

Carbon disulfide (CS_2) is a well known solvent and nonlinear material [206], which is used in industry and research for decades. This chapter reveals, why CS_2 is suitable as highly-temperature sensitive core material for fiber based nonlinear frequency conversion and how its temperature-dependent dispersion can be described mathematically. In this context, its optical and chemical properties are discussed and compared to other liquids and (soft) glasses.

3.1   Chemical properties and hazards of carbon disulfide

Carbon disulfide is a linear molecule, which is liquid at room temperature and has a rotten smell due to impurities. It is a transparent, volatile solvent with a high vapor pressure of 395 hPa at room temperature. With a density of 1.266 g/cm^3 it is heavier than water [207]. Its boiling is at 46.2 °C. CS_2 is highly flammable (flash point -30°C), and can lead to skin and eye irritations [207]. It should not be inhaled due to life-threatening health effects, which can occur to humans after inhalation of concentration ratios larger than 3000 ppm [208]. It is furthermore suspected of damaging fertility or the unborn child, and causes damage to organs through prolonged or repeated exposure, if inhaled [207]. The permissible exposure limits are given as a time-weighted average of 1 ppm (3 mg/m^3) [208]. Since 1851 CS_2 has been used extensively and without any personal protection in the rubber industry because of its exceptional fat-solvent property [209]. From the 1880s onwards its health hazards were discovered and further investigated, first in Europe, after 1935 also in the USA [209]. Until today CS_2 is widely used for the manufacture of viscose rayon and cellophane film [210]. Furthermore, CS_2 is the most common and intensively studied liquid in nonlinear optics due to its high nonlinearity and good transmission in the infrared [211]. Nowadays, it is recommended to handle CS_2 only in well-ventilated fume hoods using personal protection, i.e. gloves, protective clothing and eye protection [207].

Figure 3.1: **Molecular structure, and chemical hazard pictograms of CS$_2$.** The linear molecule consisting of one carbon and two sulfur atoms is highly flammable, poses several health risks and is toxic to aquatic life.

3.2   Optical properties of carbon disulfide

Carbon disulfide has a high refractive index of n = 1.5874 for a wavelength of 1.55 µm at room temperature [79], which makes it a suitable core material for LCFs with fused

silica cladding (n = 1.44, at 1.55 µm), and even selected fluoride claddings (CaF$_2$: n = 1.42 at 1.5 µm [212], ZBLAN: n ≈ 1.49 at 1.55 µm [213]). Further well known materials used in LCFs are carbon tetrachloride (CTC, CCl$_4$) and tetrachlorethylene (TCE, C$_2$Cl$_4$) with refractive indices only slightly above that of fused silica, see table 3.1. The large refractive index difference of CS$_2$-silica step-index fibers allows for strongly guided modes and multi-mode guidance. The discrete refractive index step between the liquid core and the fused silica cladding distinguishes LCFs from solid step-index fibers, that always show a certain gradient of the refractive index between core and cladding due to diffusion of particles during the fabrication process [214].

Table 3.1: **Properties of solid and liquid fiber materials.** Refractive indices n, electronic and molecular contributions of the nonlinear refractive indices n$_{2,el}$ and n$_{2,mol}$, and the thermo-optical coefficient (TOC)*. All values are given for a wavelength of 1.55 µm and for a room temperature of 20°C, if not stated differently. The boiling points are given for atmospheric pressure.

Properties	CS$_2$	CCl$_4$	C$_2$Cl$_4$	SiO$_2$	CaF$_2$
Refractive index n	1.587	1.448	1.489	1.444	1.427 [e]
n$_{2,el}$ (10^{-20} m^2/W)	15 [a]	4.80 [b]	5.52 [b]	2.79 [f]	1.90 [g]
n$_{2,mol}$ (10^{-20} m^2/W)	266 [a]	0.08 [b]	0.31 [b]	-	-
TOC (10^{-4} K^{-1})	-7.7 [d]	-3.9 [c]	-5.7 [d]	-0.09	-0.12 [e]
Melting point (°C)	-111	-23	-19		
Boiling point (°C)	46.2	76.7	121		
Viscosity (10^{-3} Pa s)	0.363	0.901	0.839		
Vapor pressure (hPa)	395	122	19		

* The values are obtained as indicated from: a: [215], b: [105], c: [216], d: [110] @800nm, e: [212] @1.5µm @300K, f: [217], g: [218], and from [219] if nothing is specified.

The transmission of CS$_2$ is very high around the telecommunication wavelength of 1.55 µm showing only few weak absorption peaks < 2 dB/cm between 1.9 and 3.3 µm, see table 3.2 a). Figure 3.2 shows a measured attenuation curve of CS$_2$ from 1.2 µm to 10 µm, as published in [219], which unveils further transmission windows around 4 µm, 5.5 µm and beyond 8 µm (details in table 3.2 b)). This makes CS$_2$ suitable as fiber core material in the near to mid infrared.

Table 3.2: **Absorption peaks (a) and transmission windows (b) of CS$_2$** in selected wavelength regions obtained from figure 3.2.

a) Absorption peaks from 1.2 µm to 3.5 µm.

Wavelength of attenuation peak (µm)	1.95	2.23	2.70	2.76	2.90	3.23	3.42
Attenuation coefficient (dB/cm)	0.52	1.70	0.59	0.53	0.82	0.89	16.23

b) Transmission windows from 1.2 µm to 11 µm (threshold 2 dB/cm).

Start wavelength (µm)	<1.2	3.65	4.90	5.33	7.66	9.69
End wavelength (µm)	3.36	4.18	5.17	5.77	9.51	10.85

The optical Kerr effect has been studied intensively in bulk carbon disulfide since the second half of the 20th century ([23], [24], [220]). The strong nonlinear light-induced birefringence allows to use CS$_2$ filled cells as polarization rotating waveplates (also called
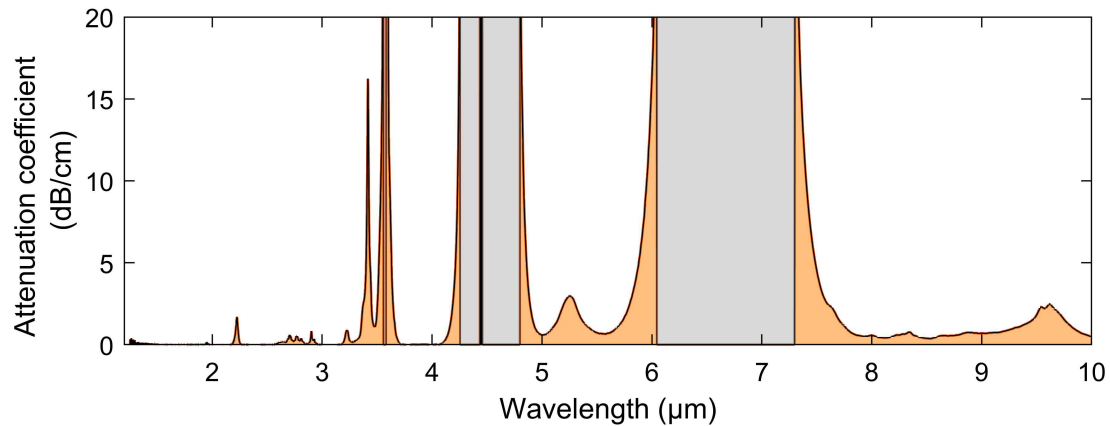
Figure 3.2: **Attenuation coefficient of CS$_2$ in the near to mid infrared.** Experimental results from [219]. No data available in the gray shaded regions with strong attenuation. Adapted with permission from [219]. Copyright 2022, The Optical Society.

Kerr cells), and nonlinear switches. The nonlinear effects of self-focusing [221], [222], and self-phase modulation [25] become present in CS$_2$ when ultrashort pulses with picosecond length or shorter are focused in bulk liquid cells or are injected into LCFs. In case of self-phase modulation the time-varying refractive index change induced by the orientational (non-instantaneous) Kerr effect comes into play.

Effectively, the third-order optical nonlinearity of CS$_2$ has instantaneous bound-electronic ($n_{2,\mathrm{el}}$) and non-instantaneous molecular ($n_{2,\mathrm{el}}$) contributions [223], which were characterized in detail by Reichert et al. [215], [224]. The purely electronic nonlinearity of CS$_2$ $n_2 = 1.5 \cdot 10^{-19}\,\mathrm{m^2/W}$ is already significantly larger than that of fused silica $n_2 = 0.28 \cdot 10^{-19}\,\mathrm{m^2/W}$, see table 3.1. The efficient nonlinearity results from adding the pulse width-dependent non-instantaneous molecular contribution to the electronic response. For CS$_2$ the non-instantaneous terms become relevant for pulse lengths larger than 100 fs [224]. The time-dependent molecular contribution arises from vibrations of the linear CS$_2$ molecules, namely collision (col), libration (lib) and diffusive (dif) molecular terms [223]. The total time-dependent change in the refractive index can be expressed as

$$\Delta n = n_{2,\mathrm{el}}I(t) + \int_{-\infty}^{\infty} \sum_m n_{2,\mathrm{m}} r_\mathrm{m}(t - t') I(t') dt', \tag{3.1}$$

including the three retarded nuclear nonlinear response terms $n_{2,\mathrm{m}} r_\mathrm{m}(t)$ ($m = \mathrm{col, lib, dif}$), the irradiance $I(t)$, and the nonlinear electronic response $n_{2,\mathrm{el}} = 3\Re(\chi^{(3)})/(4n_0^2\epsilon_0 c)$ with the linear refractive n_0, the vacuum permittivity ϵ_0, the bound electronic third-order susceptibility $\chi^{(3)}$ and the speed of light in vacuum c [215]. The non-instantaneous response of CS$_2$ is strongly dependent on the pulse duration of the irradiant light source. For pulses as short as 30 fs to 40 fs these molecular contributions can be neglected because the pulse passes quicker than the reorientational effects occur [225]. The second-order nonlinearity $\chi^{(2)}$ vanishes for CS$_2$ because it is a symmetric molecule.

In solids, the non-instantaneous response is often dominated by the nonlinear Raman response that shows a continuous and broad peak around $\Delta \nu = 0$ due to the bound molecular states [226]. In contrast, the Raman gain spectrum of liquids does not have any broad peak around $\Delta \nu = 0$, but several strong distinct narrow peaks [225]. The strongest Raman response of CS_2 is at $\Delta \nu = 656\,\text{cm}^{-1}$ with a bandwidth of $\delta \nu = 0.7\,\text{cm}^{-1}$ [227]. It results from symmetric stretching modes elongating and squeezing the linear molecule [228]. One consequence for CS_2-core fibers pumped by ultrashort pulses is the absence of a continuous Raman induced soliton redshift of spectrally narrow soliton pulses [225]. Furthermore photon pair generation via spontaneous four-wave mixing in LCFs profits from the distinct Raman peaks of liquids, reducing the Raman noise, which commonly is the main noise source of photon pair generation in silica-core fibers [229]. Note that, the non-instantaneous response leads to modified soliton dynamics, when longer pulses > 100 fs are used [225], [230].

Raman generation [227], [231]–[233], Brillouin scattering [234], and SCG [79], [235], [236] are studied intensively in CS_2-core fibers. The light confinement in the waveguide complements the high nonlinearity of CS_2, and allows for long tightly confined propagation lengths within the nonlinear medium. In the context of SCG, self-phase modulation [236], soliton-driven DW generation [81] and four-wave mixing [237], [238] have been studied experimentally in CS_2-core fiber. Beside these experimental studies, many nonlinear simulations have been performed for various fiber types including capillary fibers and liquid-filled PCFs, always taking advantage of the strong nonlinearity of CS_2 as core material.

3.3 Thermo-optical properties of carbon disulfide

The influence of temperature on the refractive index of CS_2 can be described by a Sellmeier equation with temperature-dependent Sellmeier coefficients $B_1(T)$, $C_1(T)$, (see Tab. 3.3, as published by [79]), extending the dispersion formula suggested by W. Sellmeier in 1872 [239]:

$$n(\lambda, T) = \left(1 + \frac{B_1(T)\lambda^2}{\lambda^2 - C_1^2(T)} + \frac{B_2\lambda^2}{\lambda^2 - C_2^2}\right)^{1/2} \tag{3.2}$$

The first-order thermo-optical coefficient (TOC) is defined as the wavelength dependent linear slope of the refractive index at the chosen temperature T_l with respect to room temperature T_0:

$$n(\lambda_k, T_l) = n_0(\lambda_k) + \left.\frac{dn}{dT}\right|_{T_0}(\lambda_k) \cdot (T_l - T_0) \text{, with } \left.\frac{dn}{dT}\right|_{T_0} = \text{TOC.} \tag{3.3}$$

The Sellmeier coefficients of CS_2 given in table 3.3 are used to calculate the refractive index and all dependent fiber parameters in this work, neglecting any piezo-optical

dependency, because the pressure is assumed to be constant throughout this study. Temperature-dependent values of the refractive index of CS_2 are calculated and plotted in figure 3.3 for a pump wavelength of 1.55 μm using the Sellmeier coefficients from table 3.3. The plot shows an almost linear decay of the refractive index for increasing temperature. The obtained slope of $-7.3 \cdot 10^{-4} \, K^{-1}$ corresponds to the thermo-optic coefficient of CS_2. It absolute value is slightly smaller than that of the value given for 800 nm in the literature ($-7.7 \cdot 10^{-4} \, K^{-1}$) [110]. This difference is minor considering that the thermo-optic coefficient of fused silica is almost two magnitudes smaller, see table 3.1. Its absolute value is also higher than that of other known nonlinear liquids (e.g. CCl_4 and C_2Cl_4, see table 3.1) as well as of semiconductor materials, which are known to have high thermo-optical coefficients (e.g. GaAs: $2 \cdot 10^{-4} \, K^{-1}$) [111]. This makes CS_2-core fibers very sensitive on thermal changes, which can be a disadvantage but also be turned into an advantage, if those LCFs are used for thermal sensing or to controllably tune nonlinear spectral broadening by temperature, as done in this work.

Table 3.3: **Sellmeier coefficients of CS$_2$**, for temperature T in Kelvin, and room temperature $T_0 = 293.15 \, K$ [79].

$B_1(T)$	$2.17144765 - 0.66589562 \cdot (T/T_0)$
B_2	0.085924705
$C_1(T)$ [μm]	$0.18382049 - 0.00505833 \cdot (T/T_0) - 0.00421529 \cdot (T/T_0)^2$
C_2 [μm]	6.48315928
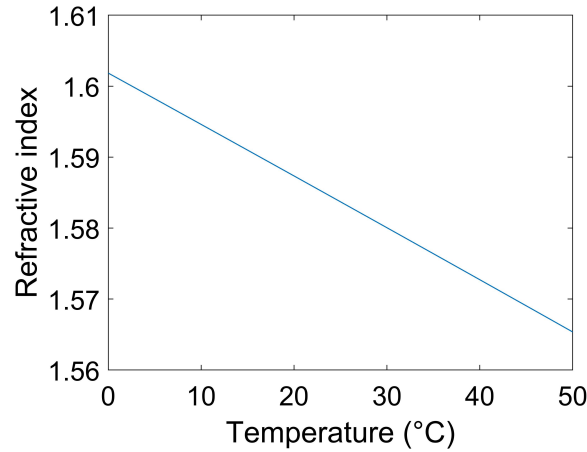
Figure 3.3: **Temperature-dependent refractive index of CS$_2$ at 1.55 μm.** Values calculated using the Sellmeier coefficients for CS$_2$ from table 3.3.

4 Fiber preparation, experimental setup and numerical GNLSE solvers

This chapter introduces the major steps to obtain temperature-controlled SCG in CS_2-core fiber experimentally and numerically. It is explained how the highly volatile liquid is inserted and enclosed in the capillary fiber, how the higher-order modes are excited and how the spectral output is characterized in experiments. Furthermore the thermal control is explained. In the numerical case, the necessity to include the liquid dynamics and higher-order mode coupling using split-step Fourier solvers for the GNLSE is discussed.

4.1 Fiber preparation

The CS_2-core optical fibers used in this work are based on fused silica capillary fibers drawn at the competence center for speciality fibers of Leibniz-IPHT. Their small central circular hole will serve as fiber core when filled with a high-refractive index liquid, in this case CS_2. The most crucial parameter for these studies is the core size, which slightly varies along the several hundred meter to kilometer long fibers due to slight changes in the drawing process. In this study core sizes between 3.5 μm and 4.0 μm are used. To find a capillary with the correct core size, scanning electron microscopy (SEM) images are taken from the fiber cross sections, which allow to determine the core diameter with an accuracy of 50 nm. Fiber probes with significantly cylindrical holes ($\Delta d > 100$ nm) are not used for the nonlinear experiments, because they introduce further effects like spatial birefringence [240]. The diameter of the cladding does not influence the measurements. It is chosen to be 250 μm, 125 μm or 80 μm, which in all cases is significantly lager than the core size, so that the evanescent field does not reach the air-cladding boundary.

To prepare an LCF both ends of the capillary fiber are attached in opto-fluidic mounts, which consist of small, well sealed liquid reservoirs (<1 ml) with transparent windows that allow in- and out-coupling of light to and out of the fiber. To enable good hand-cleaving of the fiber ends the polymer coating of the fiber is removed. Due to the high nonlinearity of the core liquid CS_2, only short fiber lengths of 8 cm to 12 cm are used.

As soon as one reservoir is filled with CS_2, it gets dragged into the fiber via capillary forces. The filling time t_{fill} of a capillary fiber with length L and hole diameter d can be estimated by the Washburn equation [241]

$$t_{\text{fill}} = \frac{4L^2 \cdot \eta_{CS2}}{d \cdot \sigma_{CS2} \cdot \cos(\theta_{CS2})} \tag{4.1}$$

taking into account the surface tension $\sigma_{CS2} = 32.3 \cdot 10^{-3}$ N/m, and the viscosity $\eta_{CS2} = 0.363 \cdot 10^{-3}$ Pa · s. The contact angle θ_{CS2} is assumed to yield $cos(\theta_{CS2}) = 0.5$ for CS_2 and fused silica [242], [243]. For a fiber length of 10 cm and a hole diameter of 4 μm this

yields a filling time of approximately 4 minutes. After the fiber is completely filled with CS_2 from one side, the second liquid reservoir is filled and both sides of the mount are tightly sealed so that the volatile liquid does not evaporate.

4.2   Experimental setup

4.2.1   Optical setup and laser parameters

All experiments are conducted with a commercial ultrashort fiber laser FemtoFiber pro IRs-II from Toptica, which has a center wavelength of 1570 nm, and a pulse duration of less than 40 fs at a repetition rate of 80 MHz. Its beam size $(1/e^2)$ is indicated with 1.8 mm, but at the position of the LCF it is extended to a diameter of roughly 4 mm. The optical setup to couple the laser beam into a LCF and analyze its output is shown in figure 4.1 a).
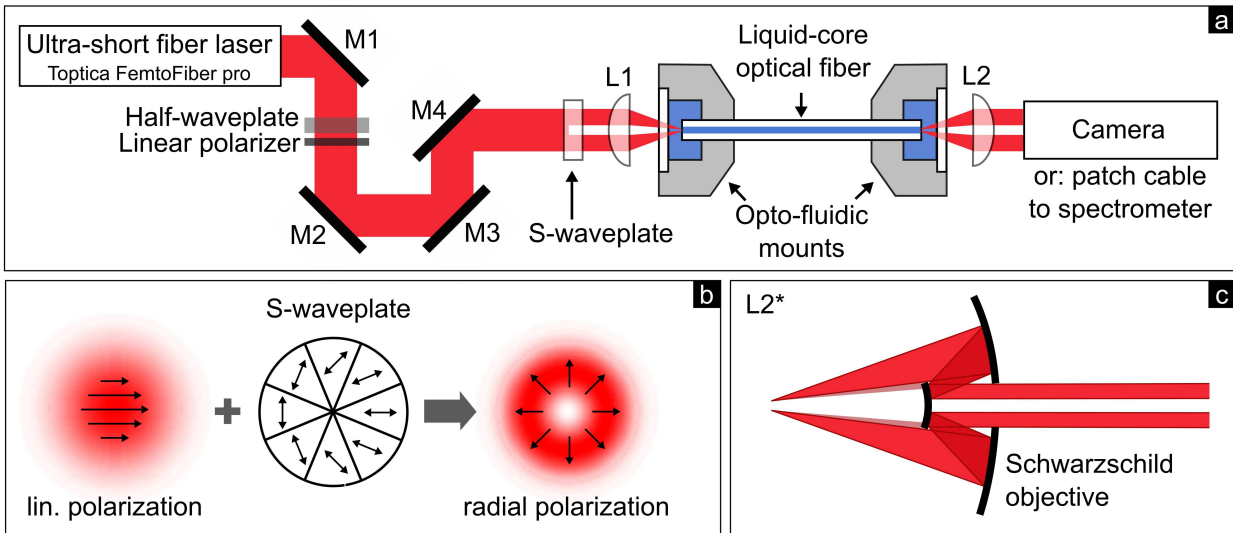
Figure 4.1: **Optical setup for SCG in liquid-core optical fibers.** a) The laser beam emitted from the ultra-short fiber laser source (FemtoFiber pro IRs-II from Toptica) is directed to the liquid-core optical fiber using silver mirrors M1-M4. Its power can be adjusted using a rotatable half-waveplate in combination with a fixed linear polarizer. The beam profile is transferred via an s-waveplate to resemble the ring-shaped higher-order modes TE_{01} and TM_{01}. An aspherical lens L1 (C230-C Thorlabs) is used for incoupling to the fiber, which is sealed by opto-fluidic mounts. The outcoupling lens L2 is either an aspherical lens (C036 from Thorlabs) or a Schwarzschild objective (Ealing 36x). The output beam is analyzed by an infrared camera and different spectrometers. Reproduced and adapted under the terms of the CC-BY license [81]. Copyright 2021, The Authors, Published by Springer Nature. b) Scheme of the transformation of a linear polarized Gaussian beam into a ring-shaped radial polarized beam using a commercial s-waveplate that consists of half-waveplates with rotating fast axes as indicated by the double-head arrows. c) Scheme of the beam path in a Schwarzschild objective, which is used as lens L2 in a).

The laser provides a maximum average power of approximately 120 mW, which can be attenuated by the combination of a half-waveplate and a linear polarizer to ensure damage-free incoupling at low average powers < 10 mW. The first two mirrors (M1 and M2) redirect the beam, which is shared with other optical setups. The other two mirrors (M3 and M4) are used to couple the beam into the fiber with an aspherical lens (L1,

C230-C Thorlabs), which is chosen instead of an objective with many lenses to reduce the additional chirp applied on the ultrashort pulse. It has a focal length $f = 4.51$ mm, and a numerical aperture $NA = 0.55$, which yields highest incoupling efficiency in comparison to other available aspherical lenses. The linearly polarized Gaussian shaped laser beam emitted from the laser is transferred to a ring-shaped beam with radial or azimuthal polarization using a commercial s-waveplate from Altechna, which is placed before the incoupling lens. The s-waveplate consists of continuously rotating half-waveplates [244], as sketched for discrete angles in figure 4.1 b). After passing the s-waveplate the laser beam resembles the higher-order radial polarized TM_{01} fiber mode, which should be excited in the fiber core. Rotating the s-waveplate by $90°$ with respect to the input polarization, the azimuthally polarized TE_{01} mode can be excited. The windows of the opto-fluidic mounts, which the beam passes before reaching the fiber, are either made of sapphire or fused silica. Sapphire windows have a better transmission between $2\,\mu m$ and $5\,\mu m$ than fused silica, but due to their birefringence, they can distort the incoupling beam and are thus rather used at the outcoupling side, where the spectrum is broader and the deformation of the beam is not affecting the excited mode. At the incoupling side the spectrum is centered around $1.57\,\mu m$, so a window of fused silica, which does not manipulate the polarization of the incoupled beam, is sufficient. The light ejected from the fiber is either collimated on an infrared camera (IK1513 from ASB Data Ray Inc.) to observe the beam profile or it is coupled into a patch cord fiber ($100\,\mu m$ core, material: InF) connected to different spectrometers for spectral analysis. For the coupling to the spectrometer a d-coated aspheric lens (L2, C036-D, Thorlabs, $f = 4.00$ mm, $NA = 0.56$) was used initially (experimental results in figure 4.3, 7.1, and 7.3). In all presented experiments conducted with the big Peltier element (which changes the temperature of the whole central fiber section homogeneously) this aspheric lens was implemented at the outcoupling side. During the project this lens L2 was first replaced by an achromatic objective (Mitutoyo MPlan Apo NIR 10x Objective) to reduce the chromatic aberrations. Finally, a Schwarzschild objective (Ealing 36x Reflecting Objective, NA 0.5) was used as lens L2 to prevent any chromatic aberrations and thus allows to couple all wavelengths similarly well into the patch cord fiber, which is feeding the spectrometers. A scheme of the beam path of the ring-shaped beam in the Scharzschild objective is shown in figure 4.1 c). The ring-shaped beams used in this work experience less losses in this reflecting objective compared to Gaussian shaped beams, because the small central mirror blocks central beams, which are weak for the ring-shaped beams. The Schwarzschild objective was used for all experimental results conducted with the longitudinally flexible Peltier element row (figure 7.6, and 7.8).

4.2.2 Excitation and characterization of higher-order modes

The spatial polarization distribution of the injected beam and the output beam can be characterized by measuring the Stokes parameters using a rotatable linear polarizer and

a quarter-wave plate [245]. For higher-order TE_{01} and TM_{01} modes a quartered pattern overlaid to the ring-shaped intensity distribution is expected as shown in my Master thesis [246]. It was demonstrated that the laser beam of the setup shown in figure 4.1 can be transferred to a higher-order TM_{01} or TE_{01} mode by the s-waveplate with a high purity of 96%-99% [81]. Furthermore, the output beam of the fiber remains dominantly in the respectively excited higher-order mode [81]. Due to the high purity demonstrated before, in this work, the polarization was only checked qualitatively by rotating a linear polarizer. Behind the polarizer two oppositely placed lobes, which rotate with the polarizer, can be detected in case of pure higher-order modes. Figure 4.2 shows a sketch of the intensity, and polarization distributions (black arrows) of the higher-order TM_{01}, TE_{01}, and HE_{21} modes without any filter and for three different orientations of the linear polarizer.
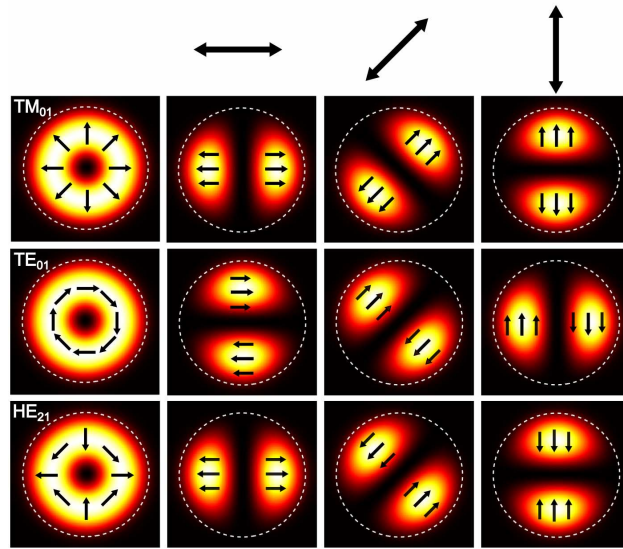
Figure 4.2: **Intensity and polarization distribution of HOMs behind a linear polarizer.** Schematic for different orientations of the linear polarizer. TM_{01} (top row), TE_{01} (middle row) and HE_{21} (bottom row) can be distinguished using the three given filter orientations indicated with black arrows on the top. The black arrows in the plots sketch the field orientation for a fixed moment in time. The polarization of the HE_{21} mode is not rotational symmetric. If the mode is excited rotated by $45°$, the lobes behind the linear polarizer will be rotated by $90°$.

Before starting the nonlinear experiments, good excitation of the desired higher-order mode is ensured. First, the output power is optimized exciting the fundamental mode at maximum of $10\,\text{mW}$ average input power by removing the s-waveplate from the setup. Second, once an input to output coupling efficiency $>30\,\%$ is achieved in the fundamental mode, the s-waveplate is inserted. Its position is adjusted with respect to the beam path to obtain the purest higher-order mode possible. The beam profile captured with the ABS camera should show a clear central hole in the intensity distribution and a symmetric rotation of the lobes, when the linear polarizer is inserted and rotated. In case the intensity distribution has a peak instead of a hole in the center of the beam profile and its intensity oscillates without any spacial rotation when rotating the

polarizer, the incoupling needs to be readjusted because the fundamental mode HE_{11} seems to dominate at the fiber output.

The overall output power is measured behind the fiber sample with a powermeter to assure sufficient coupling efficiency and to detect decoupling at the input as well as losses due to fiber damages. The coupling efficiency to higher-order TM_{01} and TE_{01} modes varies between 14% and 32% for an average input power of 100 mW, depending on the core size and coupling conditions.A drop of the output power at the long-wavelength side during the experiments typically indicates that the targeted higher-order mode is no longer efficiently excited. Whenever such a drop occurs the coupling to the higher-order mode is improved with the infrared ABS camera at low average input power of maximum 10 mW to avoid damaging the liquid close to the fiber core at the incoupling side. For detailed analysis of the output modes in different spectral domains, band pass, short pass and long pass filters are used optionally.

When filtering short- and long-wavelength DWs, as well as soliton and pump of the experimental output spectrum of a TM_{01} mode in a 4.0 μm CS_2-core fiber, their intensity profiles appear asymmetrical, showing two distinct lobes for all wavelength domains despite the pump, see experimentally obtained mode images it the top of figure 4.3. Further analysis of the filtered mode profiles revealed rotations of the lobes when rotating the linear polarizer, so the polarization is supposed to be radial with a non-uniform intensity distribution, which might be caused by slight asymmetries of the fiber core or birefringence of the outcoupling optics, e.g. the sapphire window of the opto-fluidic mount.

4.2.3 Spectral output characterization

Experimentally, the supercontinuum spectra, which are generated in the CS_2-core samples, are characterized using several optical spectrum analyzers (OSAs) that cover different spectral ranges, see table 4.1. In general the grating-based OSAs from Yokogawa have a larger dynamic range (lower noise level) compared to the Fourier transform-based OSA205 from Thorlabs, which covers the broadest spectral range from 1.0 μm to 5.6 μm. During the spectral analysis, the smaller dynamic range of the Thorlabs OSA is taken into account by adding a constant offset (equal to the noise level difference) to all measured spectra to prevent jumps at the intersection wavelength of the displayed spectra. Due to the overlap of the bandwidth of the different spectrometers, the intersection wavelength of the spectra can be optimized to assure a smooth transition between them.

As cutback measurements are difficult to realize in experiments with LCFs, the spectral dynamics are studied for constant fiber lengths either by step-wise increasing the input pulse energy or by comparing step-wise modified temperature scenarios. Matching these
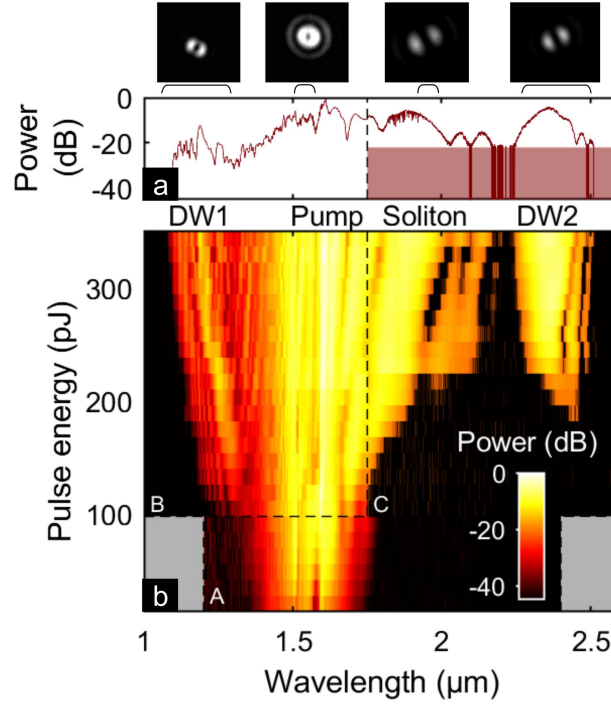
Figure 4.3: **SCG for increasing pulse energies in the TM$_{01}$ mode of a partly heated 4 μm CS$_2$-core fiber.** Experimental results measured with three different spectrometers (A: ANDO OSA AQ6375, B: ANDO OSA AQ6317B, and C: Thorlabs OSA 205). The central fiber section of 5.5 cm length is heated to 37°C, while the first and last 2 cm of the fiber remain at room temperature of 20°C in all cases. a) Spectral output for maximum in-fiber pulse energy of 331 pJ with spectrally resolved output mode profiles. b) Output spectra for varying in-fiber energy. No spectrum was captured in the gray shaded regions. Reproduced and adapted under the terms of the CC-BY license [205]. Copyright 2021, The Authors, Published by Wiley.

Table 4.1: **Properties of optical spectrum analyzers (OSAs) used in this work.**

OSA Model	Company	Wavelength range	Max. dynamic range
OSA205	Thorlabs	1000-5600 nm	43 dB
AQ6375	Yokogawa	1200-2400 nm*	55 dB
AQ6374	Yokogawa	350-1750 nm	60 dB
AQ6315A	Yokogawa	350-1750 nm	70 dB
AQ6317B	Yokogawa	600-1750 nm	70 dB

*extendable to 1000-2500 nm in test mode.

experimental results with simulations the pulse evolution inside the fiber can be obtained from the simulations.

Figure 4.3b shows the output spectra of the TM$_{01}$ mode excited for increasing input pulse energies in a 9.5 cm long CS$_2$-core fiber with a core-diameter of 4.0 μm. The transitions between the spectrometers are indicated with black dashed lines. For better visibility the elevated noise floor of the Thorlabs OSA205 is set to -40 dB artificially, see red dashed region in subfigure (a). The spectral transition between the spectrometers is smooth. The onset of the long-wavelength DW at 2.4 μm is only visible for input pulse energies larger than 180 pJ due to the higher noise floor of the used FTIR OSA. But actually it is expected to be generated simultaneously to the short-wavelength DW at 120 pJ. Furthermore, a loss peak of CS$_2$ (not considered in the simulations) is reducing the detectable

spectral range above 2.7 μm. The aspheric lens (C036-D, Thorlabs) that shows chromatic aberrations is used here to couple the output beam to the spectrometers. To ensure that the long-wavelength DW is detected as good as possible, the coupling was optimized for longer wavelengths eventually suppressing shorter wavelengths. As mentioned before a Schwarzschild objective without any chromatic aberrations is the better choice to prevent wavelength biased measurements, and therefore this reflecting objective was used in later measurements. Note that the coupling conditions always remained constant within a measurement and only the pulse energy or temperature was changed.

4.2.4 Thermal control

The temperature along the fiber is controlled with Peltier elements, either one big Peltier element (5 cm x 5 cm) or a row of 10 small Peltier elements (2.8 mm x 2.8 mm). There is a small gap < 0.5 mm between the Peltier elements, so that in simulations the length of the individually heated zones is considered to be 3.0 cm without any gaps. Even if figure 4.4 shows 16 small Peltier elements attached to the fiber, only 10 elements are actively controlled during the experiments. While the temperature of the big Peltier element is controlled manually via a single adjustable voltage supply, the row of small Peltier elements are fed by a specially programmed control unit. With this control device, which was developed and programmed by the colleague Johannes Hofmann, the voltage and thus temperature of each element is adjustable individually.
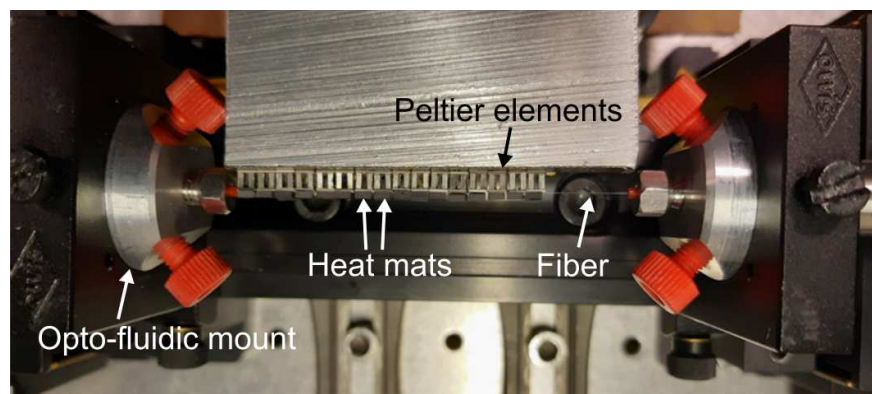
Figure 4.4: **Photo of the thermo-optical setup.** The laser beam is coupled into the liquid-core fiber from the left side. The central section of the fiber can be heated or cooled with a row of 3 mm-long Peltier elements. The thermal camera to observe the temperature distribution, which is facing the covered Peltier elements from below the picture, is not shown here.

For ideal heat transfer the fiber is placed directly on top of the Peltier element(s) and covered with a heat mat of the size of the individual Peltier elements, see figure 4.4. In some cases another heat mat is included between the Peltier elements and the fiber to close a gap caused by height differences. This additional heat mat slightly reduces the maximal temperature achievable in the fiber, and slightly increases the response time by less than 30 seconds.

Using the big Peltier element its temperature is measured with a thermal sensor, which is placed under the covering heat mat right next to the fiber. In case of the small Peltier elements a thermal camera takes pictures from the heat mats covering the fiber. A calibration conducted with a fiber Bragg grating correlates the temperatures measured on the covering heat mat with the actual temperature of the fiber. The calibrated fiber temperature is already given as output on the thermal images. As each Peltier element has a slightly different inner resistance, applying the same voltage does in general not imply the exact same temperature. Furthermore, neighboring Peltier elements influence each other so that their voltage-temperature dependence is coupled. Therefore, a short algorithm is used to get the corresponding voltage input values of each Peltier element for the targeted temperature profiles. This voltage calibration, which was also prepared by Johannes Hofmann, is conducted before the nonlinear measurements to speed up the measuring time and reduce the decoupling during the actual experiment. In the nonlinear experiments a file with the obtained voltage values for each temperature scenario is used as input for the Peltier element control unit. Due to the opto-fluidic mounts 2 cm of the fiber at the start and end can not be controlled thermally and remain at room temperature for all measurements. The laser beam propagating though the fiber is not supposed to change the temperature of the liquid core, because CS_2 is not absorbing at the wavelengths of the pump beam. Experiments to actively heat a fiber from outside using another laser, required high powers and a highly absorbing coating disposed around the fiber cladding [247].

4.3 Numerical GNLSE solvers

By conducting numerical simulations of the pulses propagating through the CS_2-core fiber it is possible to study the nonlinear dynamics at different positions inside the fiber. Besides the spectral evolution also the temporal evolution of the pulse can be studied in simulations and both can be correlated in a spectrogram to distinguish which spectral component has which time delay. In this section the GNLSE and the split-step Fourier algorithm to solve it numerically are explained. Furthermore, a multi-mode solver is discussed, which led to the discovery of an intermodal coupling effect. A comparison with the experimental conditions yielded that the single mode approach is sufficient, and the contribution of marginally co-excited modes is negligible.

4.3.1 Generalized nonlinear Schrödinger equation (GNLSE)

The generalized nonlinear Schrödinger equation (GNLSE) describes the evolution of the spectral field envelope $\widetilde{A}(z;\omega)$, and its time-domain counterpart $A(z,t) = \mathcal{F}\left\{\widetilde{A}(z;\omega)A_{\text{eff}}^{-1/4}(\omega)\right\}$ normalized to the effective mode area A_{eff} (defined in equation 2.9) during propagation in the fiber along the spacial coordinate z. In our case the

following form of the GNLSE is used as described by [225]:

$$\partial_z \widetilde{A}(z;\omega) + \frac{1}{2}\alpha_{\mathrm{m}}(\omega)\widetilde{A} - \mathrm{i}\bar{\beta}(\omega)\widetilde{A} = \mathrm{i}\tilde{\gamma}(\omega)\mathcal{F}\left\{A(z,t)\int_{-\infty}^{\infty} h\left(t'\right)\left|A\left(t-t'\right)\right|^2\,\mathrm{d}t'\right\}. \quad (4.2)$$

The modal attenuation α_{m} of the respective mode m considers the material absorption of CS_2. The propagation constant in the moving time frame $\bar{\beta}(\omega) = \beta(\omega) - \beta(\omega_0) - \omega\partial_\omega\beta|_{\omega_0}$ is related to the pump frequency $\omega_0 = 2\pi c_0/\lambda_{\mathrm{p}}$. The modified nonlinear coefficient $\tilde{\gamma}(\omega)$ is defined with respect to the nonlinear refractive index $n_{2,CS_2} = 3\chi^{(3)}(4\epsilon(\omega)\epsilon_0 c_0)^{-1}$ via $\gamma(\omega) \approx (\omega n_{2,CS_2})/(c_0 A_{\mathrm{eff}}) \equiv \tilde{\gamma}(\omega)\cdot A_{\mathrm{eff}}^{-3/4}$. The general response function $h(t) = (1-f_{\mathrm{mol}})\delta(t) + f_{\mathrm{mol}}R(t)/\int R(t)dt$ is normalized to one over the whole time interval, and incorporates the instantaneous electronic response as well as the delayed molecular response function. The weight between the two nonlinear contributions is defined by the molecular fraction $f_{\mathrm{mol}} = n_{2,\mathrm{mol}}/(n_{2,\mathrm{el}} + n_{2,\mathrm{mol}})$. The input field envelope $\widetilde{A}(0;\omega)$ is either defined by an ideal sech-squared pulse with a full width at half maximum of $\tau_{\mathrm{FWHM}} = 40\,\mathrm{fs}$ or it is reconstructed from the measured spectrum of the pump laser [185].

4.3.2 Mono-mode solver for GNLSE

In this section a rough overview over the split-step Fourier algorithm is given, which was implemented by Mario Chemnitz to solve the GNLSE for one selected mode in a step-index fiber with given geometry [225].

The split-step Fourier algorithm separates the total fiber length L in discrete propagation steps. The linear part of the GNLSE is solved in the frequency domain, while the nonlinear part is solved after a Fourier transformation in the middle of the propagation step in the time domain, see figure 4.5. After the inverse Fourier transformation, the dispersion is applied again in the frequency domain for the remaining half of the propagation step [185]. The nonlinear step is solved using a Runge-Kutta integrator of the 4th order [248].
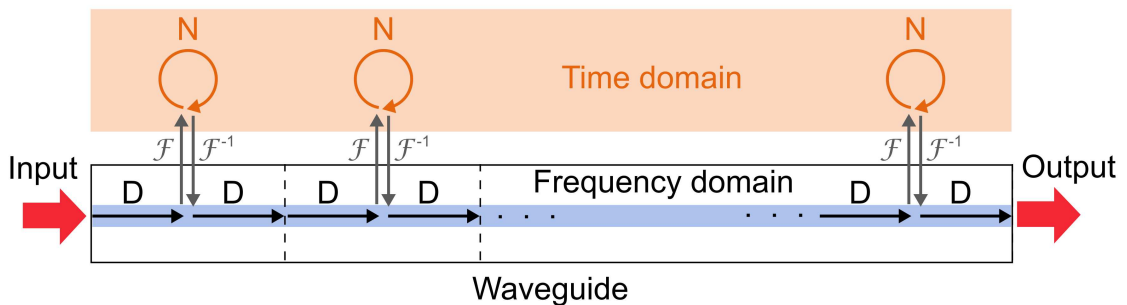
Figure 4.5: **Schematic of the split-step Fourier solver.** The linear part of the GNLSE (loss and dispersion terms) represented by the operator D is solved in the frequency domain, while the nonlinear part N is solved after a Fourier transform in the time domain [185].

This code is implemented in Matlab and allows to include chirp and white noise. The

nonlinear coefficient γ can be recalculated during propagation in the fiber, which does not influence the spectral output in this work. The molecular contribution is negligible here due to the short pulse duration of the input pulse of approx. $40\,fs$.

4.3.3   Numerical approach for coupled modes

In this section the impact of mode coupling on supercontinuum generation is discussed using simulation results obtained with a multi-mode GNSLE solver. These simulation were provided by Niklas Lüpken and Carsten Fallnich from the WWU Münster. Collaboration with them led to the discovery of intermodal DW generation and showed that the impact of mode coupling on the output spectra is negligible for the systems studied in this work.

When higher-order modes are excited in a few-mode fiber they can also couple with each other transferring energy from one mode to the other. During the incoupling process parts of the total input power can be coupled to other higher-order modes besides the mainly excited one. Using experimentally field distributions of the input laser beam that are modified via the s-waveplate, an overlap with other higher-order modes of up to 3% is observed. This contribution is calculated overlapping the theoretic fiber modes with the experimentally measured electrical fields after transferring them numerically to the focal spot, where the fiber start is to be considered [81].
This initial excitation of a mode mixture and the following mode coupling during the propagation in the fiber can be accounted for by solving the multi-mode GNLSE [55], which was first introduced by Poletti and Horak [249].

$$
\begin{aligned}
\frac{\partial A_p}{\partial z} =& i \left(\beta_0^{(p)} - \beta_0 \right) A_p - \left(\beta_1^{(p)} - \beta_1 \right) \frac{\partial A_p}{\partial t} + i \sum_{n \geq 2} \frac{\beta_n^{(p)}}{n!} \left(i \frac{\partial}{\partial t} \right)^n A_p + i \frac{n_2 \omega_0}{c} \left(1 + i\tau_0 \frac{\partial}{\partial t} \right) \\
& \sum_{l,m,n} \left\{ Q_{plmn} \left(\omega_0 \right) \left[2 \left(1 - f_R \right) A_l A_m A_n^* + 3 f_R A_l \int d\tau h(\tau) A_m(t - \tau) A_n^*(t - \tau) \right] \right\}
\end{aligned}
\tag{4.3}
$$

The key parameter of this multi-mode equation is the nonlinear coupling coefficient Q_{plmn} between the different modes p, l, m, n. A_p is the amplitude of mode p, z the propagation distance, $\beta_k^{(p)}$ the k-th dispersion coefficient of mode p, β_0 an overall phase factor, $1/\beta_1$ the velocity of the reference frame, t the time in the reference frame, n_2 the nonlinear refractive index coefficient, ω_0 the angular center frequency, τ_0 the shock time constant, f_R the fractional contribution of the non-instantaneous response, and $h(\tau)$ the delayed response function.
Solving the multi-mode GNLSE for a dominantly excited TM_{01} mode (99%) and a slightly excited HE_{21} mode (1%) in a $3.9\,\mu m$ CS_2-core fiber with a total in-fiber energy of $403\,pJ$ showed that the output of all non-excited modes remains zero, e.g. no power is coupled to the TE_{01} mode or HE_{11} mode [81] due to the structure of the numerical code.

A new effect is discovered in the same TM_{01}-HE_{21} simulation: Despite the fact, that the power in the HE_{21} is much too small for soliton fission (soliton number $N = 0.4$), the energy transfer to a DW in this mode is triggered by the soliton fission in the strongly excited TM_{01} mode [81]. The simultaneity of the DW generation in both modes could be clearly seen when plotting the spectral evolution along fiber length for both modes, as done in figure 4.6.
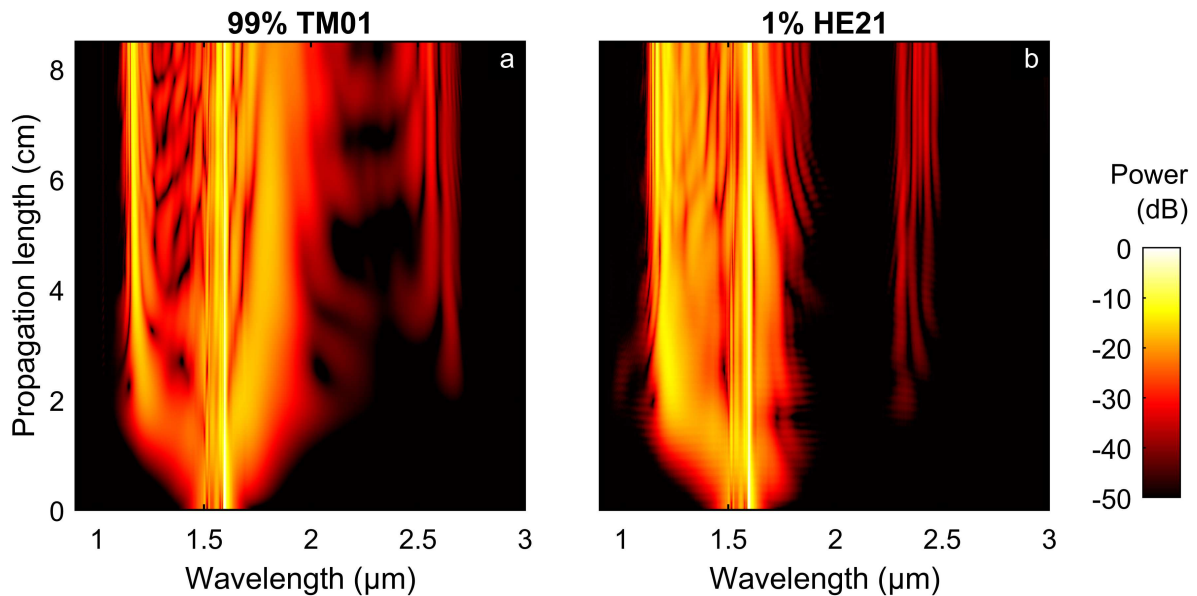
Figure 4.6: **Spectral pulse evolutions of coupled HOMs in a 3.9 μm CS$_2$-core fiber.** The total input pulse energy of 403 pJ is distributed between the modes so that the TM_{01} mode is excited with 99%, and the HE_{21} mode with 1%, simultaneously. The power distributions are normalized independently for both modes to their respective maximum. The fiber is at room temperature of 20°C. Reproduced and adapted under the terms of the CC-BY license [81]. Copyright 2021, The Authors, Published by Springer Nature.

This intermodal DW triggering can also be observed in the multi-mode simulations for an initial mode combination of 96% TE_{01}, 3% TM_{01}, and 1% HE_{21} in the same CS$_2$-core fiber. Even if the contribution of the individual higher-order modes could not be controlled step-wise in this setup, and no experimental demonstration of the effect was possible, this study triggered further investigations in a silicon nitride waveguide, which could relate the intermodal DW generation to intermodal cross-phase modulation between the different transverse modes [250].

Besides discovering this intermodal DW generation process, the coupling to other modes did not manipulate the overall output spectra significantly. To be concrete, the components in the weak modes could not be experimentally measured in the studies, and the output spectra obtained with the mono-mode simulation matched well the experimentally measured output spectra. Hence, all following simulations discussed in this work are conducted with the mono-mode solver only.

4.3.4   Evaluation of the numerical results

The numerically obtained results can be evaluated comparing their output spectra with the experimentally obtained output spectra. For a good match between simulations and experiments the most dominant spectral features (e.g. soliton and DWs) are expected to show the same changes for modified parameters and similar wavelengths. A perfect match of the simulations and experiments is not expected, even if the LCFs show an ideal step-index distribution, because the complex nonlinear dynamics strongly depend on the nonlinear properties and fiber parameters, which are not perfectly determined for each experiment.

The evolutions of the numerically obtained spectra give insights into the soliton dynamics taking place within the fiber, and are complemented by the numerically obtained temporal evolutions of the studied pulse. Applying spectral filters before transferring the spectra to the temporal domain allows to separate the temporal dynamics with respect to the wavelength. Furthermore, this reduces interference fringes between the different spectral components in the time domain. A correlation between spectral and temporal components can be also achieved calculating spectrograms from the temporal fields. The spectrograms are obtained by multiplying a sech-square shaped time gate to the temporal field envelopes before applying the Fourier transform that correlates temporal and spectral fields [202], [251].

In summary, this chapter introduced the experimental setup and the numerical simulations used to study the temperature-dependent SCG of CS_2-core fibers in work.

5 Fiber design for thermal tuning of dual dispersive wave generation in CS_2-core fibers

Dispersion profiles with a narrow AD regime in between two ZDWs can be obtained in higher-order modes of CS_2-core step-index fibers if their core diameter is adjusted carefully. In this special dispersion design, which is typically obtained in PCFs with complex fiber structures [194], [203] or tapered fibers with very small cores [37], [40], [49] dual DW generation can be achieved, when pumping in the AD regime close to the long-wavelength ZDW. The dual DW generation can be tuned by temperature. Due to the high thermo-optical coefficient of CS_2 a temperature dependence of the GVD is observed. Bent GVD curves show a stronger temperature dependence than continuously increasing/decreasing GVD curves, which promises significant temperature control over the soliton dynamics of HOMs in CS_2-core fibers.

This chapter discusses the basics of dual DW generation of HOMs in CS_2-core step-index fibers. The design of the fiber geometry, namely the core diameter, is optimized to obtain GVD distributions with two closely-spaced ZDWs. The phase matching condition between a soliton in the AD regime and DWs on both sides of the spectrum are discussed and an explanation for the strongly bending group velocity dispersion of higher-order modes in CS_2-core step-index fibers is given. The temperature dependence of the GVD is discussed and its limitations in experiments are summarized. Finally exemplary nonlinear simulations are displayed and the LCF is compared to other thermally tuned nonlinear wavelength conversion systems stressing its outstanding tuning capabilities.

5.1 Fiber design for dual dispersive wave generation

Soliton-driven SCG strongly depends on the pulse duration, the peak power and the wavelength of the input pulse, as well as on the group velocity dispersion of the mode in the waveguide. The group velocity dispersion of a mode can be modified by changing the material composition and geometry of the waveguide. In CS_2-core step-index fibers strongly bent group velocity dispersion profiles with two ZDWs can be obtained for higher-order modes, which strongly vary with core diameter [81]. Here, the dependence of the group velocity dispersion on the core diameter is studied for the three lowest higher-order modes (TE_{01}, TM_{01}, HE_{21}) as well as for the fundamental mode (HE_{11}). An explanation for this strongly bent group velocity dispersion is given and dual DW generation is studied via phase matching calculations, before a comparison to other waveguide systems for dual DW generation is presented.

5.1.1 Core diameter adjustment of CS$_2$-core step-index fibers for dual dispersive wave generation

The group velocity dispersion parameter is crucial for DW generation in soliton-based SCG. In most cases the GVD parameter is increasing continuously showing one ZDW separating a short-wavelength ND regime from a long-wavelength AD regime [30]. By adjusting the core diameter of a CS$_2$-core fiber a group velocity dispersion landscape with two ZDWs can be obtained for higher-order modes. Figure 5.1 shows the group velocity dispersion parameter D with respect to wavelength and core radius for the fundamental mode HE$_{11}$ and the first three higher-order modes TE$_{01}$, TM$_{01}$ and HE$_{21}$ in a CS$_2$-core fiber. The GVD parameter is calculated from the effective refractive index of the respective mode at room temperature in a CS$_2$-core fiber with increasing core radius, using equation 2.8.
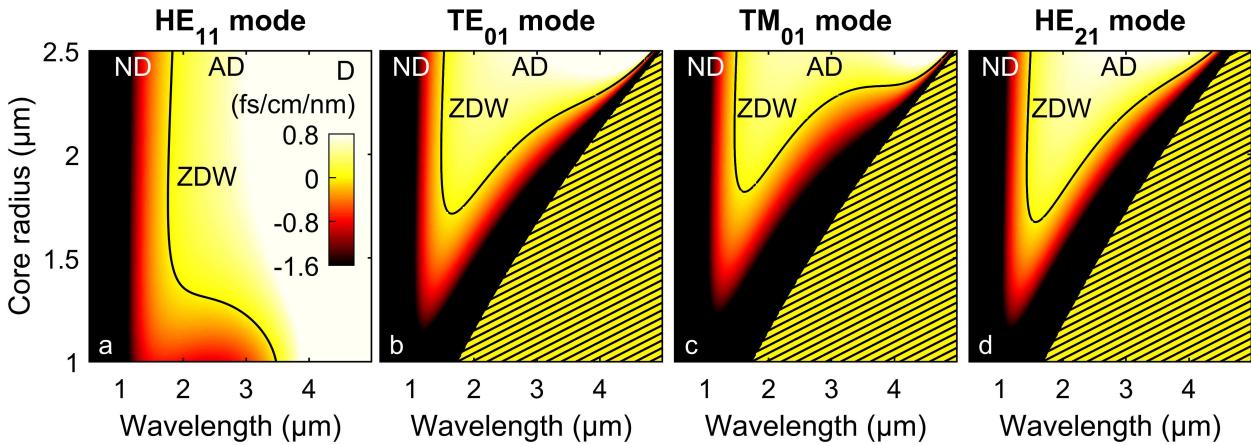
Figure 5.1: **Dependence of GVD on core diameter of CS$_2$-core fibers for different modes.** The GVD parameter D of the fundamental mode HE$_{11}$ is compared with those of the HOMs TE$_{01}$, TM$_{01}$ and HE$_{21}$. The black lines indicate the ZDWs. The color bar in (a) belongs to all images. No mode guidance in the shaded areas. The fibers are at room temperature of 20°C.

For core radii larger than 1.8 μm all three depicted higher-order modes of figure 5.4 show two ZDWs in the CS$_2$-core step-index fiber. The dispersion is anomalous in between the two ZDWs, whereas it is normal for shorter and longer wavelengths. For the TE$_{01}$ and HE$_{21}$ modes this double zero dispersion regime is already obtained for slightly smaller core radii of 1.7 μm. For even smaller core radii the three HOMs are all-normal dispersive (all-ND), which is also interesting for SCG [252]–[254], but which is not the focus for this work. The yellow-gray shaded domain at the right side depicts the region, where the modes are not guided any more, because their modal cutoff is reached ($V = 0$). In contrast to the higher-order modes, the fundamental mode HE$_{11}$ shows one ZDW only for all given core radii. The fundamental mode is normal dispersive for short-wavelengths and anomalous dispersive for wavelengths beyond the ZDW. As the ZDW of the HE$_{11}$ mode is larger than 1.9 μm it is not suitable for soliton-based SCG pumped with the available laser at 1.57 μm. However, the AD regime of all three higher-order

modes shown here covers the pump wavelength, which makes them very interesting for soliton pumped dual DW generation.

The GVD of the shown HOMs is favourable for tailorable dual DW generation due to the following reasons: Pumping in a narrow AD regime permits to generate solitons in a very low dispersion regime, which can achieve a strong spectral overlap with the DWs in the neighbouring ND regimes. Furthermore, the second ZDW shifts significantly with varying core diameter of the CS_2-core fiber, see GVD of all three higher-order modes in figure 5.1. This can be used to optimize the GVD by modifying the core diameter. In contrast, the ZDW of the fundamental mode remains almost constant for all core diameters larger than $1.4\,\mu m$. The only stronger slope of the ZDW of the fundamental mode is observed for core radii between $1.2\,\mu m$ and $1.4\,\mu m$.
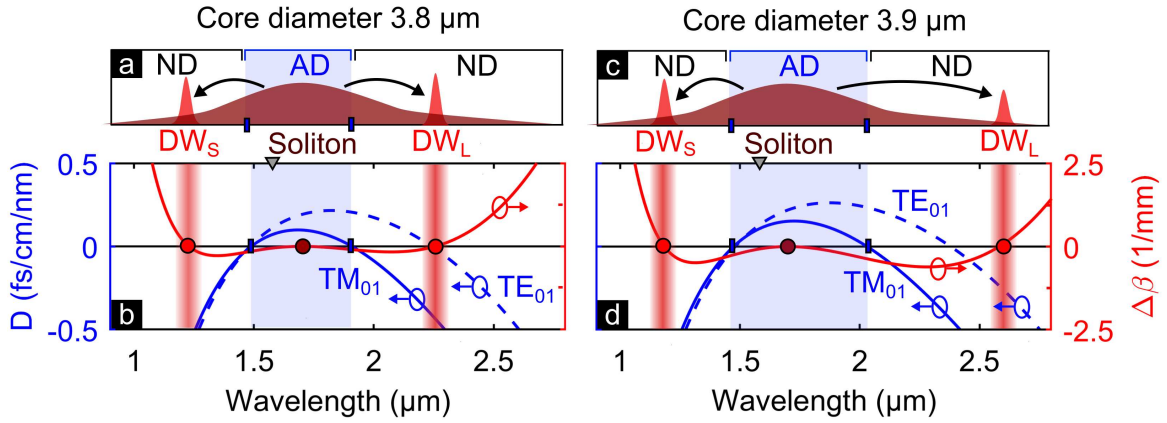
Figure 5.2: **GVD and phase-mismatch of TM_{01} mode for different core diameters of CS_2-core fibers.** Group velocity dispersion parameter D (blue, left axis) and phase matching condition between soliton and DWs $\Delta\beta$ (red, right axis) for core diameters of $3.8\,\mu m$ (a,b) and $3.9\,\mu m$ (c,d), and a fixed soliton wavelength of $1.7\,\mu m$. The blue dashed line shows the GVD parameter of the TE_{01} mode for comparison. The fiber is at room temperature of $20°C$.

Figure 5.2 shows the GVD parameter of the TM_{01} mode in two exemplary CS_2-core fibers with $3.8\,\mu m$ and $3.9\,\mu m$ core diameter, which represent two differently narrow AD regimes that cover the central pump wavelength of $1.57\,\mu m$ indicated by a gray triangle. The red curve shows the phase matching condition assuming a slightly redshifted soliton wavelength of $1.7\,\mu m$ (dark red circle) for both cases. In the moment of soliton fission the soliton is spectrally broadened (see dark red pulse in a) due to its strong temporal compression. phase matching between soliton and DWs is obtained, when the phase-mismatch vanishes, i.a. when the phase matching curve crosses zero, see red filled circles. Generation of DWs furthermore requires a spectral overlap between the soliton and the phase-matched wavelengths. For both fibers, the phase matching wavelength of the short-wavelength DW (here depicted as DW_S) is almost identical, namely $1.49\,\mu m$ (b), and $1.48\,\mu m$ (d). On the contrary, the long-wavelength DW (DW_L), redshifts significantly from $2.26\,\mu m$ (b) to $2.58\,\mu m$ (d) for increasing core size. This can be correlated to the ZDWs (blue rectangles), which are almost identical at the short-wavelength

side and redshift from 1.91 µm (b) to 2.03 µm (d) on the long-wavelength side. Similar modifications of the ZDWs are known from different tapered waveguides [57], [255]

The strength of the spectral overlap of the soliton with the phase-matched wavelengths determines the strength of the energy transfer to the DWs. Thus in general, the closer the soliton to the ZDW and the phase matching wavelength, the higher the final intensity of the generated DW.

The long-wavelengths ZDWs of the TE$_{01}$ mode (GVD given as blue dashed line in figure 5.2) are considerably longer compared to those of the TM$_{01}$ mode in the same fiber. This suggests even longer wavelengths of the phase-matched long-wavelength DWs, and a significantly reduced spectral overlap with the soliton and thus a strongly reduced conversion efficiencies. Due to the limited dynamic range of the only available OSA covering wavelengths larger than 2.4 µm (see Thorlabs OSA205 in table 4.1), the long-wavelength DWs of the TE$_{01}$ mode beyond 2.6 µm are not expected to be detectable in experiments.

Besides the fiber geometry, the pulse parameters are also influencing the spectral position of the DWs. The soliton wavelength as well as the soliton peak power are both included in the phase matching condition, see equation 2.11 in chapter 2. Whereas the peak power of the soliton only plays a role for the nonlinear phase term, the soliton wavelength influences all other terms of the phase matching condition. The soliton dynamics are further influenced by the initial pulse chirp [30], [191].
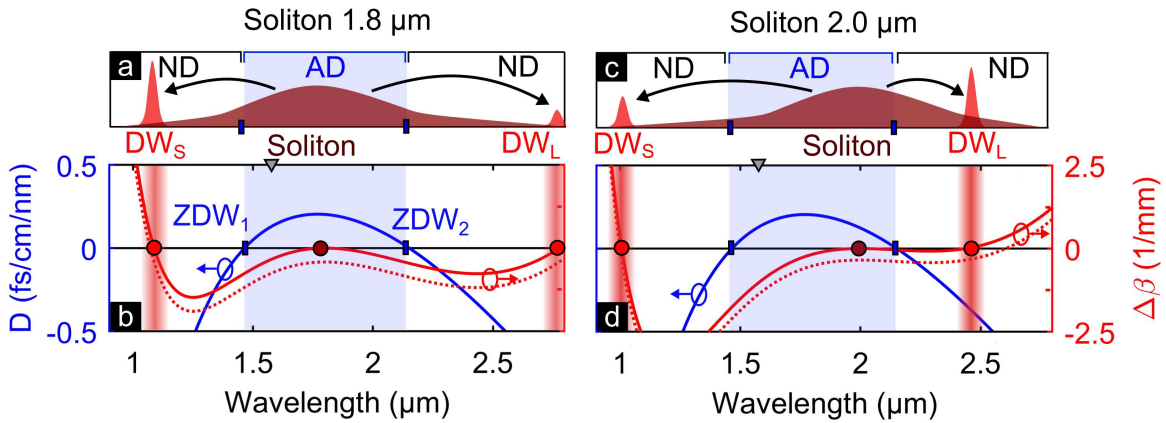
Figure 5.3: **GVD and phase-mismatch of TM$_{01}$ mode for different soliton wavelengths in a 4.0 µm CS$_2$-core fiber.** Group velocity dispersion parameter D (left axis, blue) and phase matching condition of soliton and DWs $\Delta\beta$ (right axis, red) for different soliton wavelengths of 1.8 µm (a,b) and 2.0 µm (c,d). The nonlinear phase included in red dotted phase-mismatch curves is calculated for a soliton peak power of 21.7 kW. The fiber is at room temperature of 20°C.

The spectral dependence of the DW generation on the soliton wavelength is studied in figure 5.3 for a constant GVD distribution of the TM$_{01}$ mode in a 4.0 µm CS$_2$-core fiber. The red curves show the phase-mismatch of DWs with a soliton at 1.8 µm and 2.0 µm, respectively. The phase-matched wavelengths blueshift significantly from 2.78 µm to

2.44 μm, when redshifting the soliton wavelength from 1.8 μm to 2.0 μm. The short-wavelength DWs are again influenced less, blueshifting only from 1.09 μm to 1.01 μm between the two cases. In general, the closer the soliton wavelength to the ZDW the closer the phase matched DW is generated to the soliton on this side, and visa versa. This was already proven experimentally for the long-wavelength DW by Genty et al. in 2002 using a microstructured fiber with two close ZDWs [39]. In case the soliton wavelength is further decreased to 1.70 μm, the long-wavelength DW shifts up to 2.9 μm, which is far outside the depicted region. Due to the further reduced spectral overlap with the soliton this DW will also be much weaker. Thus aiming for a high conversion efficiency, generating a DW in the proximity of the soliton is favorable, which goes along with a small spectral distance between soliton and ZDW.

The dependence of the DWs on the soliton peak power is taken into account in the nonlinear term (gray font color) of the phase matching equation 2.11. So far the nonlinear phase was not included in the depicted phase matching curves. The red dotted lines in figure 5.3 include the nonlinear phase based on a soliton peak power of 21.7 kW. This leads to a vertical shift of the phase matching curve, which equals a redshift of the long-wavelength phase matching point, whereas the spectral position of the short-wavelength DW remains almost unchanged. The soliton peak power is estimated from the totally injected peak power P_{peak} of 7.3 kW using equation 2.12. P_{peak} itself includes some uncertainties, because the actually incoupled average power as well as the exact pulse duration are unknown. Thus the nonlinear phase cannot be determined exactly.

In conclusion, CS_2-core fibers with a core diameter between 3.5 μm and 4.0 μm are promising to experimentally generate and detect dual DW generation of higher-order TE_{01}, TM_{01} or HE_{11} modes. In these fibers the HOMs have narrow AD regimes with ZDWs between 1.4 μm and 2.2 μm, for which DWs between 1.0 μm and 2.7 μm can be expected from the phase matching conditions. For the TE_{01} mode slightly smaller core diameters of 3.5 μm to 3.7 μm are preferred in comparison to the TM_{01} mode (3.8 μm to 4.0 μm), because of its slightly broader AD regime for equal core diameters.

5.1.2 Origin of strongly bent group velocity dispersion with two zero dispersion wavelengths

Group velocity dispersion profiles with two ZDWs are well known from PCFs with complex cross section profiles [194], [203] and tapers with very small core sizes [37], [40], [49], [57]. To explain why selected HOMs also show a bent GVD with two ZDWs in CS_2-core step-index fibers with moderate core radii around 2.0 μm, the GVD of three different guided modes is calculated for CS_2-core step-index fibers with increasing core radii in figure 5.4. In case of the fundamental mode HE_{11} (a) the GVD is continuously increasing for increasing wavelengths for all core radii larger or equal 1.25 μm. For the smallest calculated core diameter of 1.0 μm the GVD curve of the HE_{11} mode is bending downwards for wavelengths between 1.6 μm and 2.4 μm. In this wavelength regime the

GVD remains in the normal dispersive regime without having any ZDW below 3.5 μm. The TE$_{01}$ mode (b) as well as the HE$_{12}$ (c) mode show a bent GVD for core radii larger or equal 1.5 μm and 2.0 μm, respectively. At even larger core radii the GVD changes from being bent down to continuously increasing similar to the HE$_{11}$ mode. For the TE$_{01}$ mode this transition appears for core radii between 2.0 μm and 2.5 μm, whereas for the HE$_{12}$ it appears for even larger core radii between 3.0 μm and 3.5 μm. Depending on the bending of the GVD curves, the long-wavelength ZDW is significantly shifting closer or further from the first ZDW, whereas this short-wavelength ZDW only slightly redshifts with increasing core radius. In case of the 1.50 μm core radius of the TE$_{01}$ mode, the GVD curve is strongly bent within the ND regime showing no ZDWs, leading to an all-ND GVD regime. This shows that two ZDWs can be obtained at larger core sizes when increasing the mode order. A drawback of higher-order modes is their typically less efficient coupling efficiency to step-index fibers, their reduced cutoff-wavelength, and their more complex spatial field distribution. The modified dispersion of different HOMs [52] and the reduced coupling efficiency was also experimentally demonstrated in microstructured optical fibers [256], which showed modified SCG at the fiber output.
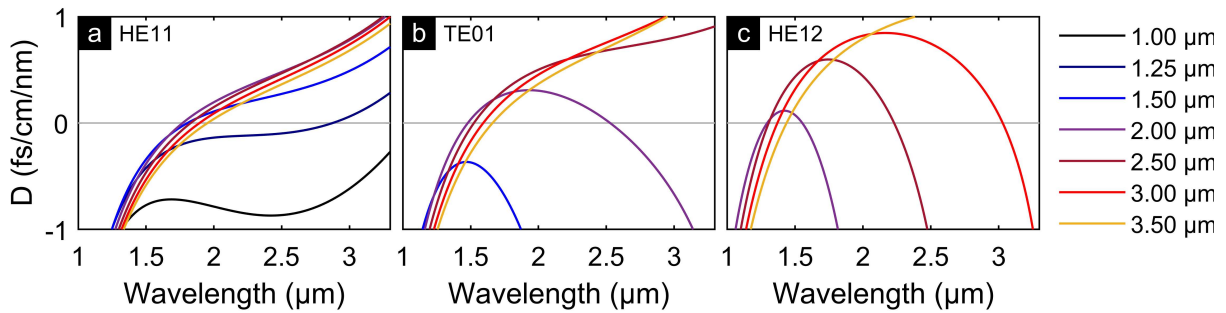
Figure 5.4: **GVD of exemplary modes for different core radii of CS$_2$-core fibers.** Group velocity dispersion parameter D of the HE$_{11}$ mode (a), TE$_{01}$ mode (b), and HE$_{12}$ mode (c). The chosen core radii are given in the legend on the right. The fiber is at room temperature of 20°C. For a core radius of 1 μm only the fundamental mode HE$_{11}$ is guided. The cutoff of the TE$_{01}$ and HE$_{12}$ mode is reached at wavelengths between 2.0 μm and 3.5 μm for the down bent GVD curves. Mode images of the respective modes are shown in figure 2.4 of chapter 2.

The correlation between bent GVD curves and the choice of core radius and mode matches with the conclusions of a 2D waveguide ray model showing that bent GVD curves can be obtained in case of stronger guiding, which typically goes along with a higher fraction of the evanescent and longitudinal field components, e.g. obtained by reducing the core size or increasing the mode order [202]. Furthermore, in that study the bending of the GVD could be correlated to the bent waveguide dispersion, separating material dispersion and waveguide dispersion, which sum up to the total GVD [257]. Using a silica cylinder in air T. Lühder [202] showed that in case of strongly guiding waveguides with small core sizes (comparable to the pump wavelength) the GVD parameter does not continuously increase with increasing wavelength, but it bends downwards and a second ZDW becomes present. Thus, the bending of the GVD for

longer wavelengths can be correlated to the strong bending of the waveguide dispersion. For strongly confined modes the bending of the waveguide dispersion dominates over the continuously increasing material dispersion, see [202] (figure 2.1, p. 10). In contrast, for weakly guiding waveguides the material dispersion dominates.

In conclusion, the waveguide impact on the overall dispersion can either be increased by reducing the core radius or choosing a higher-order mode, which in general is stronger guided, having a steeper ray angle, stronger evanescent fields, as well as stronger longitudinal field components compared to the fundamental mode. Also increasing the refractive index step between core and cladding or changing to another strongly guided waveguide type, can lead to two ZDWs for low-order modes and moderate core sizes.

5.1.3   Comparison with dual dispersive wave generation in other waveguide systems

In standard step-index fibers the group velocity dispersion typically changes from normal dispersive to anomalous dispersive for increasing wavelengths, as seen for the fundamental mode in figure 5.1. This dispersion scheme only allows for DW generation to the short-wavelength normal dispersive domain and the spectra can be only extended towards the long-wavelengths side via self-phase modulation or soliton redshift [28]. Using a fiber design with a second ZDW the long-wavelength DW typically increases the bandwidth significantly [30].

PCFs and tapered fibers with small core sizes are well known to have two ZDWs, which allows to generate dual DWs in the short- and long-wavelength ND regime. Sammut et al. first predicted dual DW generation in waveguides with 2 ZDWs in 1989 [258], but it took until 2002 for the first experimental realization of dual DW generation in tapered silica step-index fibers by Harbold et al. [37]. Before that Mamyshev et al. and Birks et al. already did first experiments in fibers with two ZDWs, using dispersion flattened and tapered single-mode silica core fibers, respectively [36], [204]. In 2003, Skryabin et al. were the first to experimentally demonstrate dual DW generation in PCFs with two ZDWs [194]. Since then many different designs of PCFs were developed and successfully used in the context of dual DW generation [39], [41]–[46], [48], [50], [54], [56], [85], [203], [259]–[261]. Several fiber and waveguide designs, which yield two or even more ZDWs were already used successfully for SCG in tapered fibers [40], [49] and rectangular waveguides [55]. To date, new PCF systems with tailored dispersion properties are introduced, which partly rely on very complex cross section designs with elliptical holes [262]–[264] or spiral orientations of the air holes [265]. Furthermore, dispersion designs with three ZDWs were achieved in nanotapered step-index fibers [49], and three up to four ZWDs were proposed for specially designed PCFs [183], [266], [267]. Also partly CS_2-filled PCFs are introduced [249], which are very promising, because they show two ZDWs for the fundamental mode, but are challenging to fabricate [211], [268]–[271]. In contrast, step-index LCF have a very simple geometry (see figure

2.1, and a large core size (up to 4.0 µm) in comparison to tapered fibers and integrated optical waveguides.

So far, supercontinua with remarkable bandwidths covering more than two octaves have been reported, e.g. using silicon nitride waveguides [55], ZBLAN PCFs [53], chalcogenide step-index fibers [52], and tapered fluorotellurite fibers [57]. All of these systems profited from the flat dispersion between two ZDWs and the low material absorption in the mid infrared. Beside a strong spectral broadening towards ultraviolet and infrared wavelength domains, adaptability of the generated spectra is demanded to meet the requirements of different applications with one and the same fiber. In case of the broadband supercontinuum obtained in the silicon nitride waveguide this was achieved by varying the waveguide geometry [55]. Modification of the group velocity dispersion to control the generated output spectrum by adapting the fiber geometry was reported in many further studies, e.g. by precise design of the dispersion of a microstructured fiber [101], e.g. implementing elliptic or spiral structures [262], [263], [265], or by using alternative waveguide materials like highly nonlinear soft glasses (chalcogenides [52], [134], [272], and tellurites [57]) or liquids [114], [236], [273], [274]. Another common tuning scheme for tailoring supercontinuum spectra is the adaption of the pump wavelength. All these tuning schemes either require a tunable pump laser or to exchange the whole waveguide.

In LCFs, the optical properties can be manipulated by temperature, due to the high thermo-optical coefficient of the core liquids, which are comparable to semiconductors, see chapter 3. Strong temperature-induced tuning of nonlinear effects in LCFs has been already proposed in simulations [120]–[122], but in general only minor shifts up to 4 nm/K have been realized experimentally [113]–[117], [119]. Velazquez-Ibarra et al. demonstrated thermally-induced tuning of four-wave mixing in ethanol-filled PCFs, showing tuning slopes of up to 13.5 nm/K for signal and idler bands [118]. Thermal tuning of LCFs is similar to the pressure tuning of gas-filled hollow-core fibers [106], [107], [125], [127], [275]. But while only smooth pressure changes are possible in gas-filled fibers, temperature tuning in LCFs enables to apply various temperature profiles along the fiber. Using external temperature control, complex dispersion pattern can be implemented that exceed the pressure-based tuning capability of hollow-core fibers. For example, differently steep dispersion steps can be implemented and combined along the fiber length. Via this highly flexible longitudinal control of the dispersion properties, soliton dynamics can be manipulated and cascaded DWs can be generated in one and the same fiber.

5.2 Influence of temperature on dual dispersive wave generation in CS$_2$-core fibers

As the effective index of the core material CS$_2$ strongly depends on temperature, see Sellmeier equation 3.2 in chapter 2, resulting in a high thermo-optical coefficient of -7.7·10$^{-4}K^{-1}$, the group velocity dispersion of HOMs in CS$_2$-core fibers is supposed to be dependent on the temperature as well. This section studies the dependence of their GVD on temperature and discusses the experimental conditions and limitations for temperature tuning of CS$_2$-core fibers given in the experimental setup.

5.2.1 Temperature-induced modifications of the dual dispersive wave generation in CS$_2$-core fibers

In the following, it is shown that the group velocity dispersion of HOMs in CS$_2$-core fibers can be strongly modified by changing the temperature of the fiber. As the TOC of the core material CS$_2$ is much higher than the TOC of the silica cladding (see table 3.1 in chapter 3), only the temperature changes of the core material are taken into account for all following calculations.
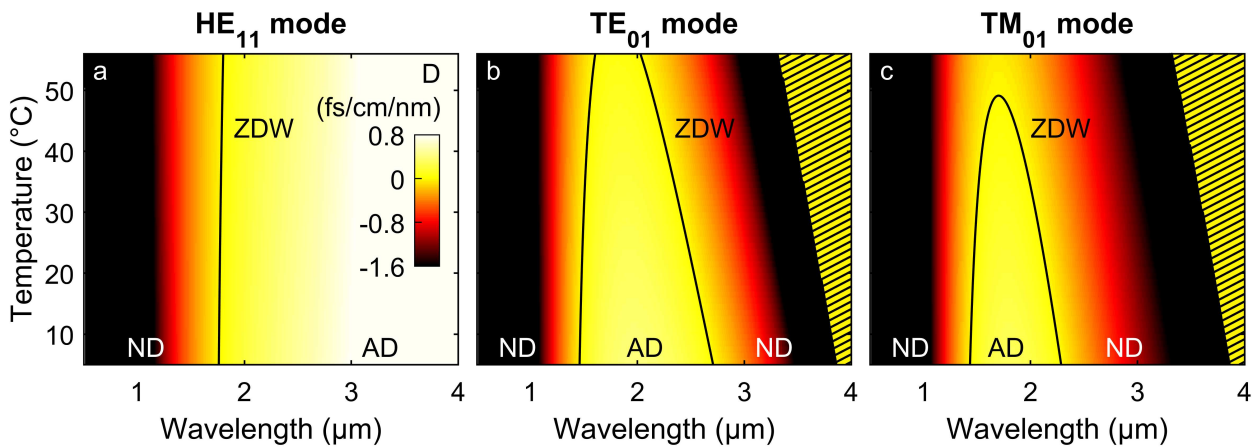
Figure 5.5: **Dependence of GVD on temperature for different modes in a 4.0 µm CS$_2$-core fiber.** Temperature-dependent group velocity dispersion parameter D of HE$_{11}$ (a), TE$_{01}$ (b), and TM$_{01}$ (c) modes. The black line indicates the ZDWs. In the shaded regions the HOMs are not guided any more, because they reached the cutoff. The colormap in (a) refers to all graphs.

Figure 5.5 shows the group velocity dispersion parameter D over wavelength and temperature for the HE$_{11}$, TE$_{01}$, and TM$_{01}$ modes in a 4 µm CS$_2$-core fiber. The ZDW of the HE$_{11}$ mode changes only slightly by approx. 1 nm/K over the whole temperature range. The same implies for the short-wavelength ZDW of the TE$_{01}$ and TM$_{01}$ mode, which only shift by approx. 3 nm/K. In contrast, the long-wavelength ZDWs of the two HOMs shift much more drastically by approx. -12 nm/K, and in case of the TM$_{01}$ mode the GVD becomes all-ND for 47°C, whereas the TE$_{01}$ mode still has a narrow anomalous region at 55°C. The GVD of the HE$_{21}$ mode (not shown here) has a very similar temperature dependence like the TE$_{01}$ mode.
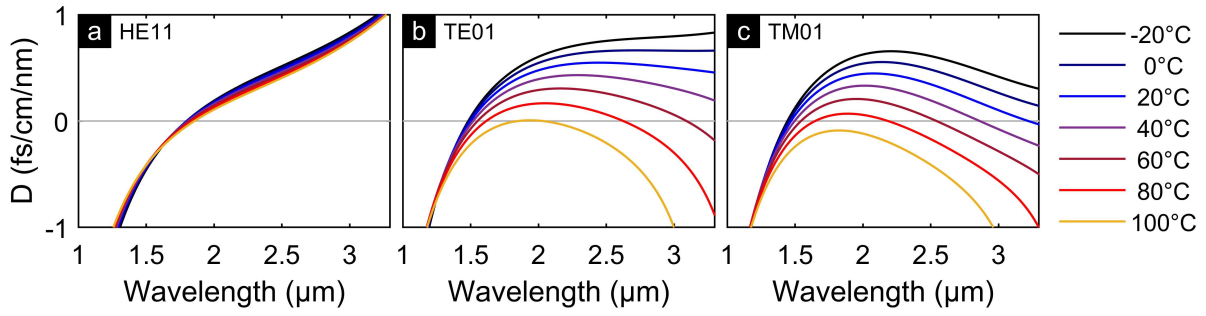
Figure 5.6: **GVD of exemplary modes for CS_2-core fibers at different temperatures.** Group velocity dispersion parameter D of the HE_{11} mode (a), TE_{01} mode (b), and TM_{01} mode (c). The chosen temperatures are given in the legend on the right. The fiber has a core diameter of 4.6 µm.

The stronger shift of the long-wavelength ZDW with temperature can be explained by the temperature-dependent bent of the waveguide dispersion. Small changes of that bending result in a dominant shift of the long-wavelength ZDW while the short-wavelength ZDW remains almost constant. To further prove this temperature-dependent bending of the GVD, the dispersion parameter D is plotted for discrete temperature steps of a CS_2-core fiber with 4.6 µm core diameter in figure 5.6. TE_{01} and TM_{01} modes both show a strong down-bending of D for increasing temperatures, which shifts the long-wavelength ZDW much stronger than the short-wavelength ZDW. The GVD parameter D or the fundamental HE_{11} mode is again much less modified by the temperature changes. Note, that the temperature range chosen in this graph is exceeding the realistic values for a fluid phase of CS_2, which is restricted by its melting and boiling point. The same was observed for modified core diameters as shown in figure 5.4. Furthermore, a longer wavelength has equivalent impact on the mode as a smaller core, because both implies a stronger confinement of the mode in the core (as long as cutoff is not reached). As shown before, a smaller core increases the impact of the bent waveguide dispersion on the overall GVD. Consequently the temperature impact on the GVD is stronger for longer wavelengths [202].

The impact of the temperature-induced GVD modifications on the dual DW generation is studied with the help of figure 5.7, which shows the GVD parameter (blue line) as well as the phase-mismatch of soliton and DWs (red line) for the TM_{01} mode in a 4 µm CS_2-core fiber at 20°C (a,b) and 35°C (c,d). The temperature induced blueshift of long-wavelength ZDWs (blue rectangle) induces a blue shift of the DW-phase-matched wavelength (red dots) at the long-wavelength side, when considering a constant soliton wavelength of 1.9 µm. As seen before, increasing the temperature leads to a shift of both ZDWs towards the pump and a decrease of the AD regime. The phase-matched wavelengths also shift towards the pump for increasing temperatures, so their overlap with the soliton is increased and the generated DWs are expected to have higher powers. As the group velocity dispersion and ZDW of the fundamental mode HE_{11} (blue dashed line) are almost identical for both temperatures, no significant shift of a potential DW is
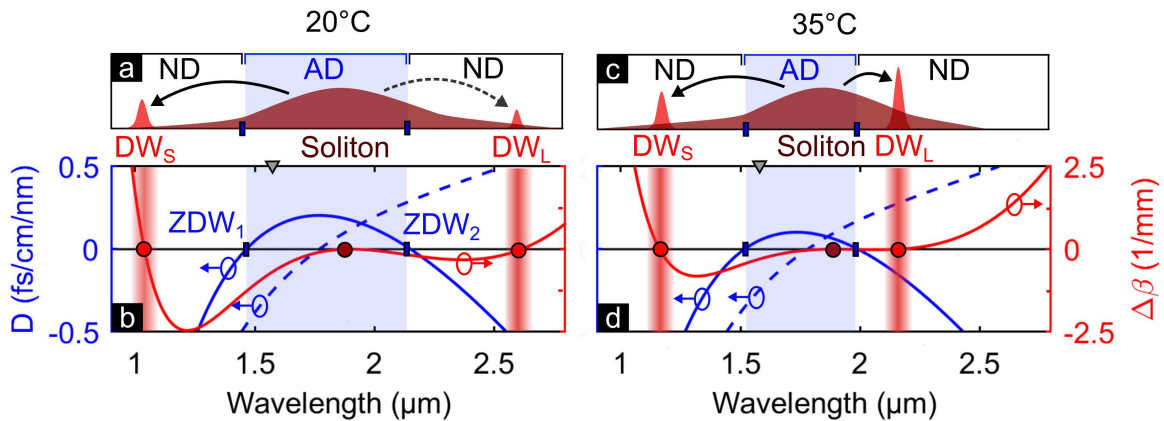
Figure 5.7: **GVD and phase-mismatch of TM$_{01}$ mode for 4.0 μm CS$_2$-core fibers at two different temperatures.** Group velocity dispersion parameter D (blue, left axis) and phase-mismatch between soliton and DWs $\Delta\beta$ (red, right axis) for fiber temperatures of 20°C (a,b) and 35°C (c,d). For the phase matching a soliton wavelength of 1.9 μm is considered. The nonlinear phase is neglected. The blue dashed curve shows the GVD parameter of the HE$_{11}$ mode, for comparison. Reproduced and adapted under the terms of the CC-BY license [205]. Copyright 2023, The Authors, Published by Wiley.

expected.

In conclusion, choosing the right core diameter but also the right temperature range is crucial for detecting temperature-modified DWs. It requires strongly temperature-dependent ZDWs close to the pump wavelength to allow for sufficient overlap between soliton and DW in a variable temperature range. For this reason different core diameters and heating or cooling ranges are chosen for the different higher-order modes in the experiments conducted for this work.

5.2.2   Thermal conditions and limitations in experiments

The maximum temperature which should be applied to the CS$_2$-core fibers is limited by the boiling point of CS$_2$ at 46°C. As the liquid is completely enclosed in the fiber and its mounts it cannot evaporate easily, and guidance in the fiber is still possible at slightly higher temperatures around 50°C. The minimum temperature, which is reached in experiments using the single big Peltier element is around 5°C. The heat generated on the backside of a cooled Peltier element strongly limits its minimum temperature, because the overall temperature of the Peltier element increases if the heat accumulates. So the heat capacity of the cooling body on the heated backside of the Peltier element restricts the minimum temperature, as well as its electrical and thermal properties. Massive metal blocks, which are thermally connected to the optical table are therefore used as heat sinks.

The opto-fluidic mounts enclosing 2 cm of both fiber ends prohibit the fiber ends from being heated or cooled actively. Therefore, these fiber sections are expected to remain at room temperature regardless of the temperature applied in the central fiber section,

which was proven by exemplary thermodynamic simulations using the commercial software COMSOL, not shown here. This implies that in experiments no completely heated or cooled fibers could be studied. Instead a discrete temperature step from room temperature to the applied temperature back to room temperature was realized, which influenced the SCG and will be discussed in simulations and experiment. The temperature of the thermally-controlled central fiber section as well as the room temperature remain constant during the measurements.

6 Numerical study of different soliton dynamics for dual dispersive wave generation

Dual DW generation in GVD systems with two ZDWs can be triggered by soliton fission, and soliton breakdown [42]. Soliton-breakdown can occur prior to the first soliton fission (pre-fission) or afterwards (post-fission), so that either higher-order solitons or fundamental solitons are affected. Repeated temporal compression of a soliton in narrow AD regimes is called soliton breathing. Soliton tunneling can be observed when the AD regime where the solitons are initially excited is interrupted by a locally restricted ND regime. Soliton-fission, soliton breakdown, soliton breathing, and soliton tunneling show different soliton dynamics that lead to different spectral outputs. They strongly depend on core-diameter, excited mode and temperature. To find suitable core sizes for experiments and to understand the processes and their limitations, these soliton dynamics are studied in this chapter using nonlinear simulations. Parameter studies with ultrashort pulses are conducted by numerically solving the GNLSE for HOMs in CS_2-core fibers that have restricted AD regimes with two ZDWs. After studying soliton breathing and pre-fission soliton breakdown for constant dispersion along the whole CS_2-core fiber, temperature-induced post-fission soliton breakdown, as well as soliton tunneling are discussed for partly heated CS_2-core fibers.

6.1 Overview of different soliton dynamics in narrow AD regimes

Figure 6.1 shows a schematic comparison between soliton fission (a-c) and soliton breakdown (g-i). During soliton fission the energy transfer to DWs is triggered by the temporal compression of the soliton and its corresponding spectral broadening, which leads to a significant spectral overlap with the phase-matched wavelengths in the ND domain [30], [276]. A stable fundamental soliton with soliton order N = 1 is created during the soliton fission process. This fundamental soliton or the initial higher-order soliton can be disturbed and temporally compressed again and again, which triggers periodical emission of DWs during so-called soliton breathing [28], [191], see schemes (d-f) in figure 6.1.

In contrast, soliton breakdown occurs, when a soliton approaches or passes the long-wavelength ZDW, where its stability is no longer given [277], and it rapidly loses energy to the ND domain [42], [193], [194], [200], [201], [277], see figure 6.1 (g-i). In general, soliton breakdown can occur, when a significant fraction of the higher-order or fundamental soliton is not located in the AD domain anymore [42], [193], [277], [278]. Higher-order soliton breakdown takes place very close to the fiber input before soliton fission can occur, and is thus called pre-fission breakdown. It is observed for few-cycle pulses [278], and when pumping very close to a ZDW [41]. This pre-fission breakdown of higher-order solitons is less susceptible to noise [278] compared to the post-fission

breakdown of fundamental solitons that emerged from a higher-order soliton during soliton fission. In many fibers solitons continuously redshift due to the Raman-induced soliton self frequency shift [195]–[198]. Step-like soliton redshifts are observed during the fission process [205]. If mayor parts of a soliton pass the ZDW and reach into into the ND regime the soliton will not remain stable, because the nonlinear dispersion can not be compensated, and the soliton solution is not supported in the ND regime. If the soliton remains in the AD regime, but is shifted to a wavelength with drastically reduced dispersion, it is possible that the soliton can not adiabatically adapt its pulse width or peak power to remain stable, and will break down as well. The generation of DWs triggered by soliton breakdown typically shows a strong conversion efficiency, but a smaller spectral distance from the soliton, compared to soliton-fission induced DW generation [42].

In LCFs, the redshift of solitons cannot be explained by Raman-induced redshifts, because the Raman response and nonlinear molecular response of the used liquids are negligible. For CS_2 the non-instantaneous response only has a relevant impact for pulses longer than $1\,ps$ [225], and the classical Raman response shows distinct peaks far from the pump [215], which do not lead to a continuous redshift. Consequently, no classical soliton redshift is observed in CS_2-core fibers pumped with ultrashort pulses. Nevertheless, a step-like redshift of solitons is observed during the fission process of higher-order solitons in LCFs [205], which can lead to the breakdown of solitons at the long-wavelength ZDW. Alternatively, the ZDW can be moved towards the soliton by tapering the fiber or heating it.
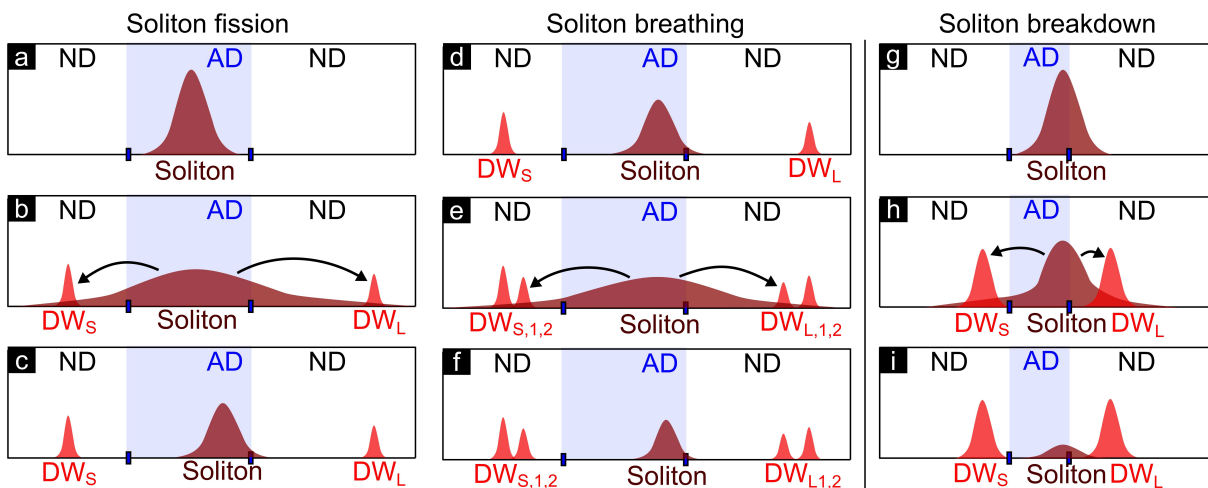
Figure 6.1: **Scheme of dual dispersive wave generation mechanisms.** (a-c) Soliton fission, (d-f) soliton breathing, and (g-i) soliton breakdown. The anomalous dispersion (AD) domain is highlighted in blue. The solitons are given as dark red peaks. The light red peaks representing the short-wavelength and long-wavelength dispersive waves are labeled as DW_S and DW_L, respectively. They are generated in the normal dispersion (ND) domains. The horizontal axes correspond to wavelengths, and the vertical ones to intensity.

DW generation triggered by temporal compression can be also observed after the tunneling of a soliton through a spatially limited ND regime [279], which will be explained in detail in section 6.5. The tunneling induced recompression can be initiated after an initial soliton fission process or before that, depending on the longitudinal position of the ND regime.

All mentioned effects are interesting due to their soliton dynamics, and their broadband spectral output. While soliton breakdown enables a strong energy transfer from the soliton wavelength to the ND regions, and high coherence [41], soliton fission induced DW generation typically yields a broader supercontinuum [280].

6.2 Dual dispersive wave generation based on soliton breathing and soliton breakdown

In this section the temporal and spectral dynamics of soliton breathing are contrasted with those of higher-order soliton breakdown. Both effects can be obtained in AD regimes with two ZDWs without changing the dispersion along the fiber. Before conducting simulations and experiments with temperature-induced dispersion changes, these two very different effects are investigated for the room temperature case. The dynamics of soliton breathing and soliton breakdown will be studied solving the GNLSE for HOMs in different CS_2-core fibers. Furthermore, the differences of numerical pulse propagation results using the experimental input spectrum or an ideal soliton-like sech-squared pulse as simulation input will be discussed. Slightly different peak pump powers are used for the different fibers (8.02 kW for the 3.45 μm case (TE_{01} mode), and 9.70 kW for the 4.0 μm case (TM_{01} mode)), which result from the different incoupling efficiencies. A numerical technique to spectrally filter the temporal pulse evolution results is used to better separate the spectral features in the temporal evolution plots.

Higher-order soliton breakdown is observed in the case of very close ZDWs being separated by less than 200 nm ($ZDW_1 = 1.58$ μm, $ZDW_2 = 1.74$ μm) for the TE_{01} mode in a 3.45 μm CS_2-core fiber, see figure 6.2 (a,b,e,f). The energy pumped to the AD regime is almost completely transferred to the DWs at the short- and long-wavelength side of the spectrum within the first 3 cm of propagation. Neither soliton fission nor a strong temporal soliton compression is observed before this breakdown. Consequently this can be called pre-fission breakdown. The input spectrum is overlapping the short-wavelength ZDW (black dashed line) independent of the used numerical input, which is based on the experimental input spectrum in subfigures (a,e), and on an ideal sech-squared pulse centered at 1.6 μm in (b,f). The soliton number calculated via equation 2.10 yields 11.3 for the experimental input pulse, and 18.3 for the ideal sech-squared input pulse. The corresponding fission lengths $L_{\mathrm{fiss}} \approx L_D / N$ [30] yield approximately 2 cm, and 3 cm, and

Figure 6.2: **Simulated temporal and spectral evolutions of HOMs in exemplary CS$_2$-core fibers using different input pulses.** TE$_{01}$ mode in a 3.45 µm CS$_2$-core fiber (8.0 kW peak power) for experimental input pulse (a,e), and ideal sech-squared pulse at 1600 nm (b,f). TM$_{01}$ mode in a 4.0 µm CS$_2$-core fiber (9.7 kW peak power) for experimental input pulse (c,g), and ideal sech-squared pulse at 1700 nm (d,h). (a,b,e,f) are normalized to their individual maximum at 0.5 cm, and (c,d,g,h) at 1 cm. The fibers are at room temperature of 20°C.

thus lie behind the onset of the observed soliton breakdown at 1.5 cm. This discrepancy might be caused by the unknown chirp of the input pulse, which influences the fission length as shown by Tran et al. [191]. In case of few cycle pulses the soliton breakdown can occur at even shorter distances as demonstrated by Babushkin et al. [278]. Similar to their observations, the temporal evolution plots in (a,b) show no clear soliton formation, but a strong temporal dispersion after the efficient energy transfer to the ND regime. The experimental input pulse and the ideal sech-squared input pulse, which are used as simulation inputs, are show in figure 6.3. The different input spectra have a common peak wavelength and a similar long-wavelength edge, while the short-wavelength edge differs significantly. Two experimental spectra are shown, one measured before 2018 (A), and another one measured in 2022 (B), both having the same main peak, but leading to slightly different output spectra when included in the numerical simulations.

In the case of wider separated ZDWs of the TM$_{01}$ mode in a 4.0 µm CS$_2$-core fiber (ZDW$_1$ = 1.46 µm, ZDW$_2$ = 2.15 µm), cascaded DW generation via soliton breathing is observed, see figure 6.2 (c,d,g,h). As known from waveguide systems with one ZDW, soliton fission based DW generation takes place due to the temporal compression and spectral broadening of a higher-order soliton. In the studied case the soliton number N is around 3.0 to 3.5 for the numerical and experimental input. As seen in the spectral evolution plots (g,h) the spectra are broadest during the first fission process reaching
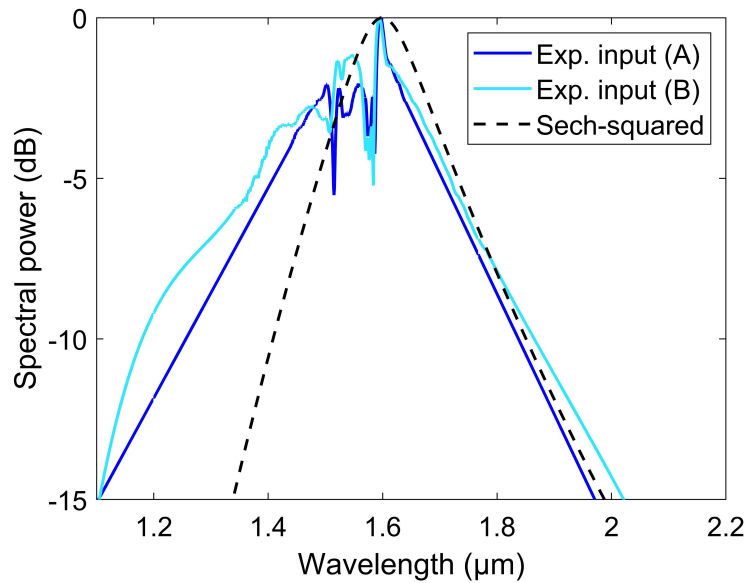
Figure 6.3: **Spectra of experimental input pulses, and of an ideal sech-squared input pulse.** Experimental spectra of the Toptica laser source were measured before 2018 (A) and in 2022 (B). Both spectra are fitted at the short-wavelength and long-wavelength edge. The ideal sech-squared pulse is centered at 1.60 μm.

beyond the DWs at both sides of the spectrum at a propagation distance of 1 cm. The wavelengths of the DWs are given by the phase matching calculations in equation 2.11 of chapter 2. It is known from literature, that for moderately narrow AD regimes bounded by two ZDWs, soliton fission can be followed by periodic recompression of the soliton accompanied by cascaded emission of DWs, called soliton breathing [191]. For the displayed supercontinuum of the TM_{01} mode this soliton breathing manifests in the generation of at least two more, clearly distinguishable, DWs on the long-wavelength side (figure 6.2 (g,h)) and periodic compression of the confined soliton peak (figure 6.2 (c,d)). The breathing period slightly varies for the experimental input (g) and the ideal sech-squared input pulse centered at 1.7 μm (h). This might be caused by the slightly different pulse widths T_0, and spectral positions, the latter leading to a slightly modified $\beta_2(\lambda)$.

To have a closer look into the soliton breakdown and soliton breathing processes, the simulation results obtained in figure 6.2 are further evaluated applying spectral filters to the spectral pulse evolution results before calculating the temporal evolution plots. The filtered evolution plots of both, soliton breakdown and soliton breathing, are shown in figure 6.4.

To spectrally isolate the soliton, filter thresholds are chosen to be 1600 nm - 1750 nm for the narrow AD regime showing soliton breakdown (e,f) and 1600 nm - 2100 nm for the intermediate AD regime showing soliton breathing (g,h). To filter the long-wavelength DW long-pass filters starting at 1800 nm (m,n), and 2300 nm (o,p) are chosen, respectively. The filter thresholds are not chosen identical to the ZDWs, which are given as white dotted lines, but they are adapted to ideally filter soliton and DWs, see spectral plot in figure 6.4 (e-h,m-p). The filtered spectral fields are calculated applying sigmoid
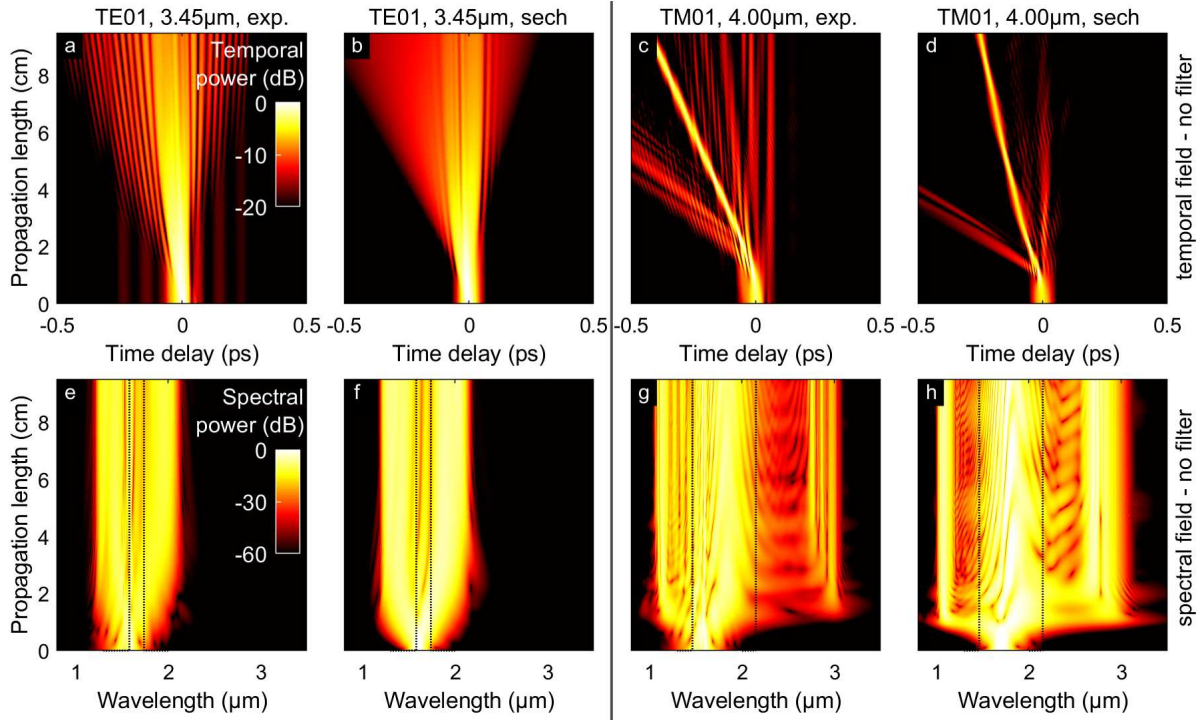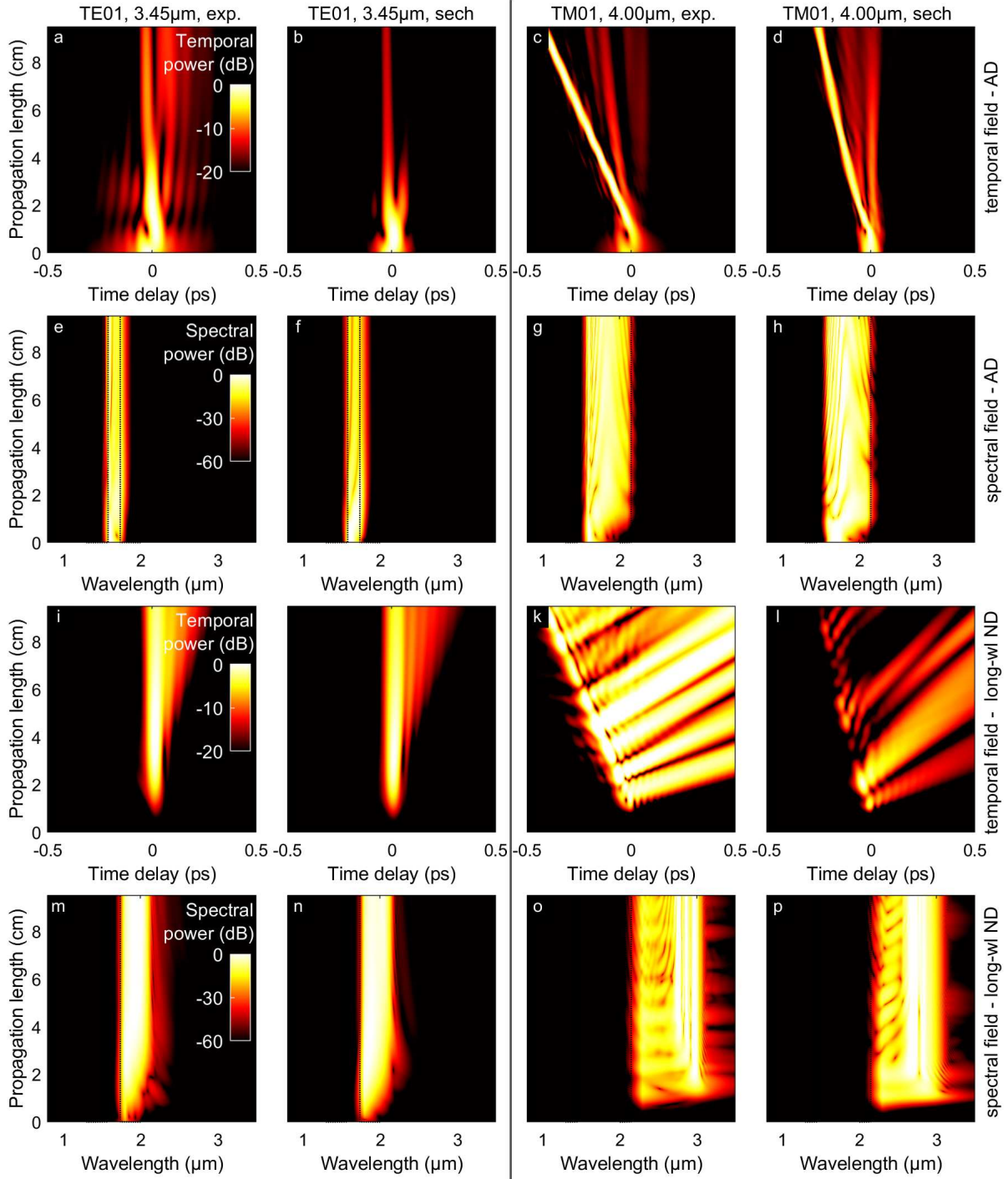
Figure 6.4: **Spectrally filtered simulated temporal and spectral evolution of HOMs in exemplary CS$_2$-core fibers using different input pulses.** TE$_{01}$ mode in a 3.45 μm CS$_2$-core fiber (8.0 kW peak power) for experimental input pulse (a,e,i,m), and ideal sech-squared pulse at 1600 nm (b,f,j.n). TM$_{01}$ mode in a 4.0 μm CS$_2$-core fiber (9.7 kW peak power) for experimental input pulse (c,g,k,o), and ideal sech-squared pulse at 1700 nm (d,h,l,p), as shown without filters in 6.2. Subfigures (a-h) AD regime (TE$_{01}$: 1600 nm < λ < 1750 nm, TM$_{01}$: 1600 nm < λ < 2100 nm), subfigures (i-p) long-wavelength ND regime (TE$_{01}$: λ > 1800 nm, TM$_{01}$: λ > 2300 nm). (a,b,e,f) are normalized to their individual maximum at 1 cm, (c,d,g,h) at 1.5,cm, (i,j,m,n) at 3 cm, and (k,l,o,p) at 2 cm. White dotted lines in the spectral plots (e-h, m-p) show the ZDWs, the temporal evolutions are given in subplots (a-d, i-l). All fibers are at room temperature of 20°C.

functions as long- and short-passes to the initial spectral fields E_S

$$E_{S,\text{filtered}} = E_S \cdot (1 + \exp\left[\pm(X - x_{\text{filter}})\right])^{-0.05}, \tag{6.1}$$

where X and x_{filter} represent the indices of the whole wavelength vector, and of the filter edge wavelengths. The exponent was optimized to obtain a good contrast without implying artificial features due to an abrupt filter edge. The numerically applied spectral filters drastically reduce the overlaps and interferences of different spectral components in the temporal evolution plots of figure 6.4 (a-d, i-l) so that it is easier to distinguish individual effects. Furthermore, hidden weak features become visible by normalizing each spectral region to its own maximum. In this way, the generation and temporal evolution of multiple long-wavelength DWs are observable for the soliton breathing case in figure 6.4 (k,l).

For the case of higher-order soliton breakdown, a significant decay of the higher-order soliton is observed for propagation lengths between 1 cm and 3 cm in the spectrally filtered temporal evolution plots of figure 6.4 (a,b). The long-wavelength components in the ND regime rise already significantly between 1 cm and 2 cm from the fiber start, see figure 6.4 (i,j).

The filtered spectra of the TM_{01} mode in the wider AD regime of the 4.0 µm fiber are shown in figure 6.4 (c,d,g,h). The temporal confined soliton peaks are already resolved in the overall evolution plots of figure 6.2 (c,d,g,h), and do not broaden significantly. Their periodic temporal recompression, matches with the re-emission of long-wavelength DWs that are visible along the whole depicted fiber length in figure 6.4 (c,d,k,l). The filtered evolution plots further unveil that all long-wavelength DWs, which are split off from the soliton, have a similar temporal slope (k,l). Moreover, they are generated at slightly different wavelengths (o,p), due to the power decay of the soliton leading to a reduced nonlinear phase in the phase matching condition.

For a more quantitative analysis of the energy transfer from the solitons in the AD regime to DWs in the ND regimes, the spectral power in the AD regimes are plotted over increasing propagation length in figure 6.5. To do so, the filtered spectral power distributions of the AD regimes from figure 6.4 (e-h) are summed up. While the power in the AD regime continuously decreases almost to zero for the cases of soliton breakdown (blue and red curve of figure 6.5), it oscillates at an intermediately high value for the breathing cases (purple and yellow curve). Similar analysis was conducted by plotting the peak intensity along the propagation distance for the case of soliton breakdown with few-cycle pulses [278]. This showed a continuous decrease of the peak power along the propagation distance for higher-order soliton breakdown. In contrast, an increase of the peak power at the fission point followed by a rather constant peak power plateau was obtained in the same publication for a soliton fission scenario.

Spectrograms at selected positions along the fiber are displayed in figure 6.6 to study the time - wavelength dependence of the optical pulses in more detail. In case of higher-order soliton breakdown (a-h) almost all spectral content is transferred outside of the narrow AD regime (ZDWs shown as white dashed lines) after 3 cm of propagation, see
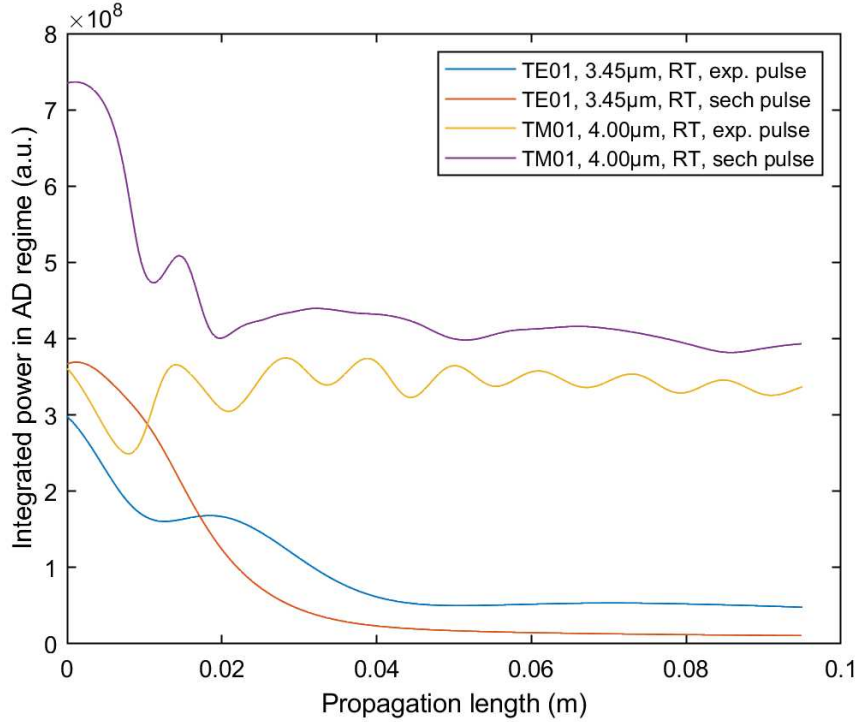
Figure 6.5: **Evolution of the overall power in the AD domain for HOMs in exemplary CS$_2$-core fibers using different input pulses.** Calculated from the filtered power distributions in figure 6.4 (e-h), and displayed in arbitrary units. Mode, core diameter of the CS$_2$-core fibers, and sort of input pulse are given in the legend. All fibers are at room temperature of $20°$ C.

second column of figure 6.6 (b,f). In case of soliton breathing a spectrally and temporally confined soliton is preserved until the fiber end at 9.5 cm (l,p). It remains unclear why the soliton is redshifted for the experimental input pulse within the first 3 cm (i,j), while it almost remains at the same frequency for the ideal input pulse (m-p).

In parallel to the different soliton dynamics, the temporal-spectral evolutions of the DWs also vary between soliton breakdown and soliton breathing. In case of soliton breakdown, the power in the DWs remains temporally confined due to the low dispersion at their spectral positions close to the ZDWs (white dashed lines), see figure 6.6 (c,d,g,h). This is different for the individual DWs generated further apart from the ZDWs in case of the extended AD regime of soliton breathing. Here, the individual DWs are separated in time and spread out during propagation (k,l,o,p).

For the experimental input pulses a temporally broadened pump background remains until the fiber end for both soliton scenarios (figure 6.6 (d,l)). This extended background slightly disturbs the overall appearance, so that the ideal sech-squared input pulses, which show very similar soliton and DW dynamics as the experimental input pulses, are used in the following numerical parameter studies.

Overall, this section shows that very similar spectral evolutions can be obtained using experimental input pulses and analytical ones, but dependent on the spectral width of the AD regime, very different soliton dynamics can be observed. Additional simulations (not included here) proofed that the non-instantaneous molecular response does not
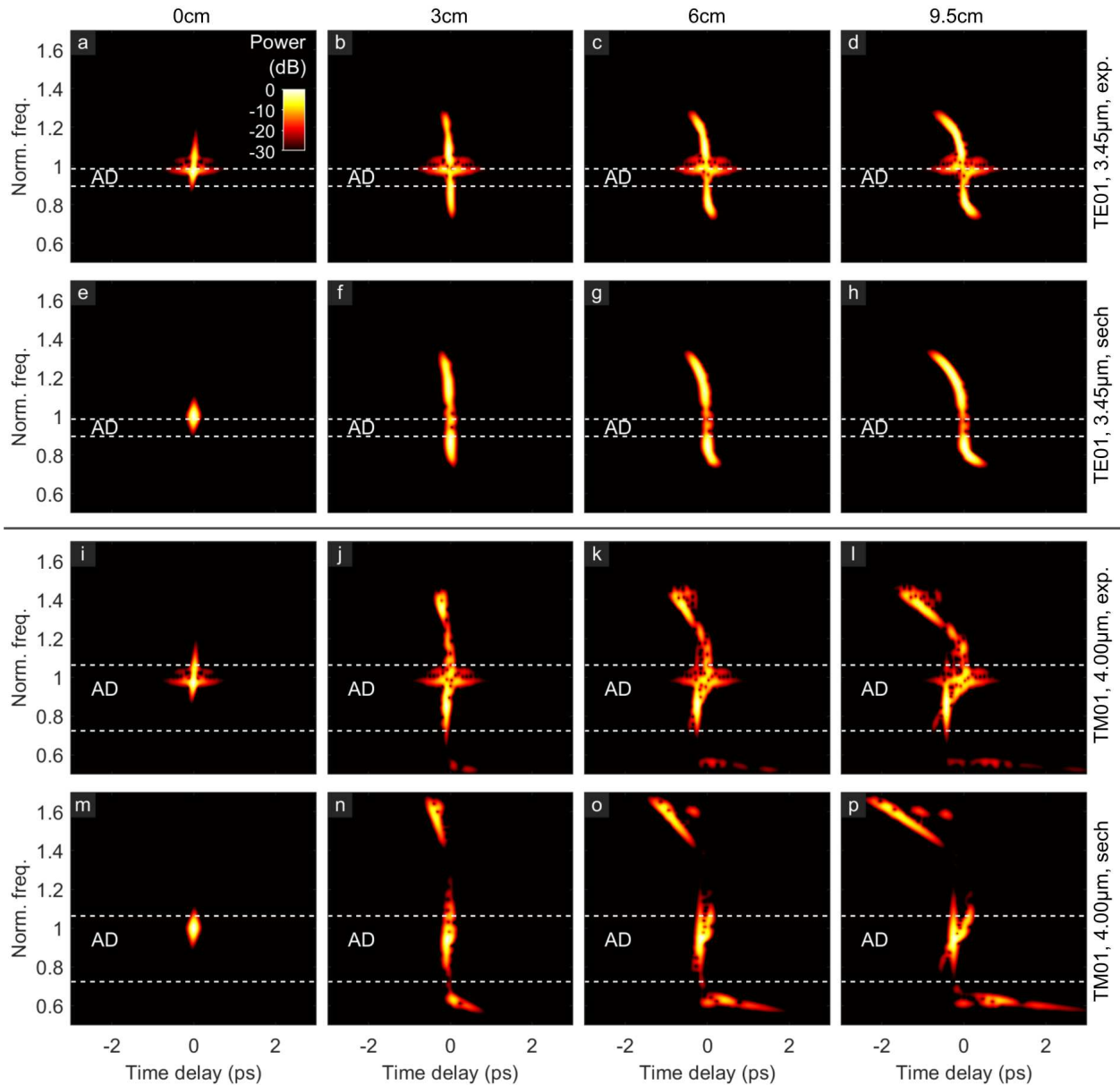
Figure 6.6: **Spectrograms of HOMs at selected positions in exemplary CS$_2$-core fibers using different input pulses.** Spectrograms for experimental input pulses (a-d,i-l) and ideal sech-squared pulses (e-h,m-p) for the TE$_{01}$ mode in a 3.45 μm CS$_2$-core fiber (a-h), and for the TM$_{01}$ mode in the 4.0 μm CS$_2$-core fiber (i-p) calculated from the simulations in figure 6.2. Displayed positions along the fiber length as indicated on the top of each column. All fibers are at room temperature of 20°C.

influence the output spectra and can be neglected in case of the ultrashort pulses of 30 fs to 40 fs used throughout this work.

6.3 Parameter studies on soliton breathing induced cascaded dual dispersive wave generation in CS$_2$-core fibers

The parameter studies of this section will show that the breathing of solitons is dependent on the input power of the soliton, as well as on the spectral position of the soliton

in the AD domain. Spectral filtered temporal evolution plots, and spectrograms at the fiber output indicate that high power prevents soliton breathing due to split-off of several solitons, and an intermediate distance of the soliton from the long-wavelength ZDW is required to obtain repeated temporal compression.

6.3.1   The dependence of soliton breathing on the soliton peak power

It is known that sufficient peak power of the soliton and thus of the input pulse is required to ensure sufficiently strong nonlinear effects for soliton fission [28], which corresponds to a soliton order $N > 1$, see equation 2.10. This lower limit also implied for soliton breathing. Varying the input peak power in simulations shows that there is also an upper limit for soliton breathing. Soliton breathing does not take place for peak powers higher than a certain threshold, as it will be demonstrated by numerical simulations in this section.

Figure 6.7: **Spectrally filtered simulated temporal evolution of the TE$_{01}$ mode in a 3.6 μm CS$_2$-core fiber at different input powers.** An ideal sech-shaped pulse centered at 1.70 μm is used and the input peak powers is varied with respect to the total input peak power of 6.12 kW from 100% (a,e), over 85% (b,f), and 70% (c,g), to 50% (d,h)). The AD regime (1600 nm < λ < 1900 nm, subfigures a-d) and long-wavelength ND domain (λ > 2200 nm, subfigures e-h) are spectrally filtered. All subplots are normalized to their individual maximum at 3 cm. The fiber is at room temperature of 20°C.

Figure 6.7 shows the temporal evolutions in the filtered AD and long-wavelength ND domains for different input peak powers of an input pulse with constant central wavelength of 1.70 μm. While for a maximum peak power of 6.1241 kW the soliton splits into two pulses within the first 5 cm of propagation (a), the soliton remains confined over the whole propagation length for smaller peak powers representing 85% (b), 70% (c),

and 50% (d) of the maximum. For these cases of reduced peak power (b-d), a temporal recompression is observed with a constant periodicity of approx. 10 cm. The soliton number decreases from 3.1 for full power, via 2.8 for 85%, and 2.6 for 70%, down to 2.2 for 50% of input power. So while the soliton number only decreases slightly e.g. from 3.1 to 2.6, the soliton dynamics changes drastically, and influence the DW generation shown in the second row of figure 6.7: For 100% input peak power (e) energy is transferred to three strong long-wavelength DWs during propagation from 2 cm up to 10 cm, and afterwards no further significant energy transfer is observed. In case of reduced peak power (f-h) additional weaker DWs are generated along the whole studied fiber length of 30 cm during soliton breathing. Furthermore, the onset and the period of soliton breathing seems to vary with peak power, which is not expected by the definition of the soliton period [28].
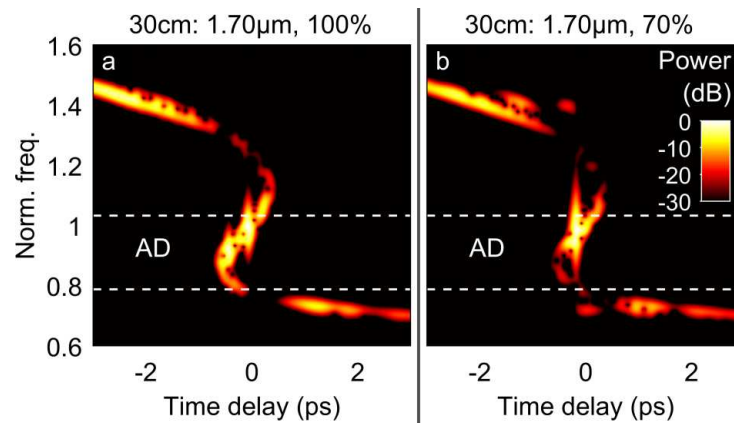
Figure 6.8: **Spectrograms at the fiber output of the TE$_{01}$ mode in a 3.6 μm CS$_2$-core fiber for different input powers.** The spectro-temporal correlations are displayed for the maximal propagation distance of 30 cm at 100% (a) and 70% (b) of the maximal input power (6.12 kW) calculated from the overall field evolutions belonging to the filtered temporal evolution plots shown in figure 6.7 (a,e; and c,g). An ideal sech-squared input pulse centered at 1.70 μm is used as input. The fiber is at room temperature of 20°C.

Figure 6.8 gives a comparison of the spectrograms at the maximum propagation distance of 30 cm for the case of 100%, and 70% input peak power. Whereas a split-off into at least two temporally separated solitons is observed for the maximum peak power (a), one temporally well confined soliton is preserved until the end of the fiber for the breathing case of reduced input peak power of 70% (b). In the latter case, multiple dual DW generation is observed in the spectrogram as well. The split-up in several solitons for high input peak powers leads to a stronger energy transfer to DWs and seems to prevent further soliton breathing.

6.3.2   The dependence of soliton breathing on the soliton wavelength

So far soliton breathing was studied for different peak powers of the input pulse. In literature soliton breathing dynamics are compared for different GVD scenarios by varying the fiber dimensions [42], [281]. In this section, the influence of the soliton wavelength

on its breathing dynamics is investigated. It is shown that soliton breathing is only observed for a certain spectral distance between the soliton and the long-wavelength ZDW. In particular, soliton breathing does not take place if the soliton is too close to the long-wavelength ZDW.
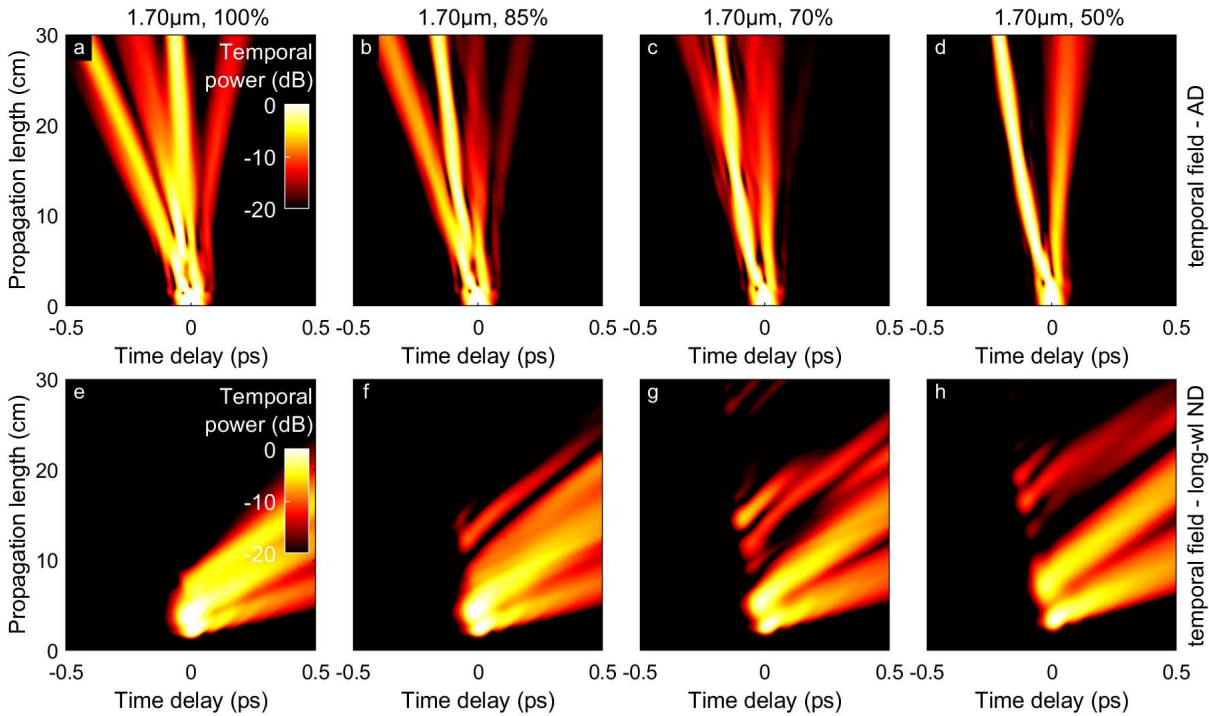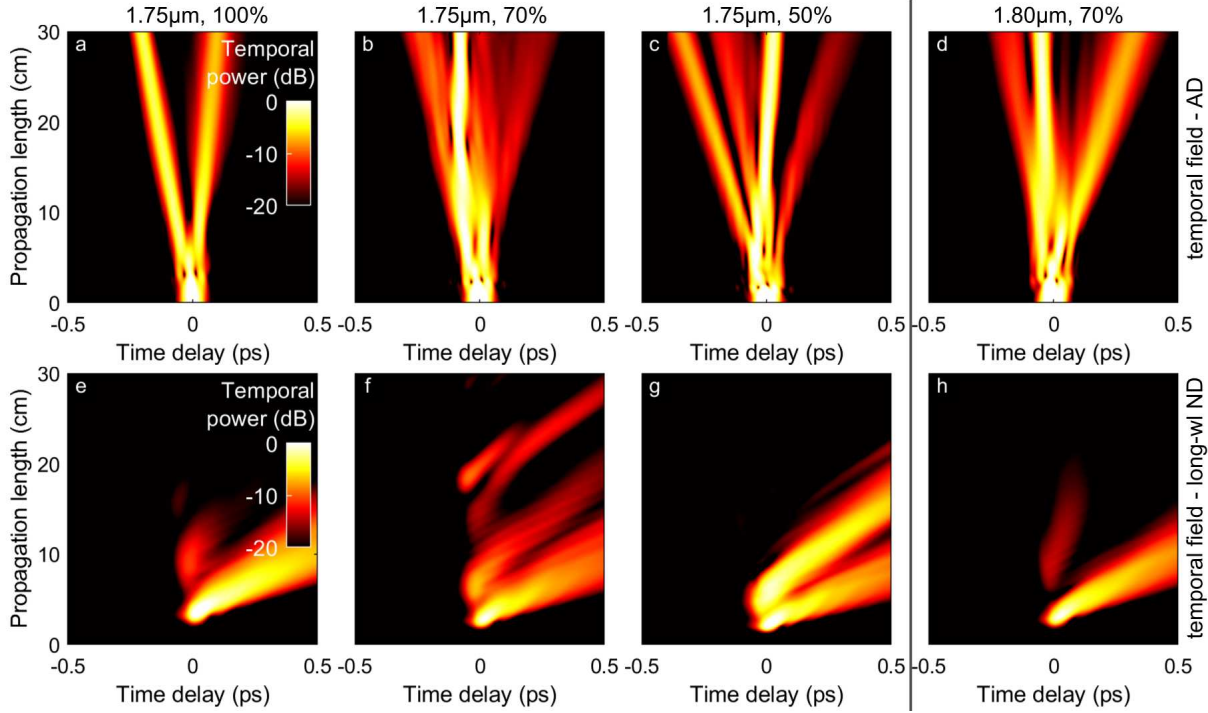

Figure 6.9: **Spectrally filtered simulated temporal evolution of the TE$_{01}$ mode in a 3.6 µm CS$_2$-core fiber for different soliton wavelengths and input powers.** An ideal sech-squared pulse with center wavelength of 1.75 µm is used with input peak powers of 100% (a,e), which equals 6.12 kW, 70% (b,f), and 50% (c,g)). For the central wavelength of 1.80 µm an input peak power of 70% (d,h) is displayed. Spectral filters were applied to isolate the fields in the AD regime (1600 nm < λ < 1900 nm, subfigures a-d) and in the long-wavelength ND domain (λ > 2200 nm, subfigures e-h). All subplots are normalized to their individual maximum at 3 cm. The fiber is at room temperature of 20°C.

Figure 6.9 shows the temporal evolutions in the AD domain (a-d) and the long-wavelength ND domain (e-h) for central wavelengths of 1.75 µm and 1.80 µm, which are closer to the long-wavelength ZDW at 1.98 µm in comparison to the hitherto central input wavelength of 1.70 µm. Again, the TE$_{01}$ mode is studied in a 3.6 µm CS$_2$-core step-index fiber. In subplots (a-c) pulses with input peak powers decreasing from 100% (soliton number N = 2.8) to 50% (soliton number N = 2.1) at the central wavelength of 1.75 µm are investigated. In this case clear soliton breathing is only observed for the intermediate peak power of 70% corresponding to a soliton number N = 2.4 (b,f). In case of a central pump wavelength of 1.80 µm, soliton breathing is neither observed for the same input peak power of 70% (soliton number N = 2.4, subplots d,h), nor for higher or lower peak powers (not shown here). One possible explanation for this behavior is that a short spectral distance of the soliton to the long-wavelength ZDW prevents soliton breathing due to the strong energy transfer to the phase-matched DW in the AD regime and the drastically reduced dispersive effects in the close proximity of the

long-wavelength ZDW. The soliton period z_0 also increases with decreasing absolute value of the GVD (β_2), which might lead to breathing lengths longer than the fiber length for soliton wavelengths closer to the ZDW.

In conclusion, for soliton breathing the soliton power needs to be high enough to obtain strong nonlinear effects, but not too high, because a split-up in several soliton peaks prevents further soliton breathing. Furthermore, its spectral distance to the long-wavelength DW should not be too close to prevent that the majority of its energy is transferred too fast to the phase-matched DWs. In experiments no tunable laser source with suitable pulse duration is available, and the actual soliton wavelength and peak power in the fiber can only be estimated. Therefore, instead of varying the pulse parameters, the fiber parameters and thus the group velocity dispersion will be adjusted by changing the temperature.

6.4 Temperature-induced soliton breakdown

In longitudinally varying fibers or longitudinally dispersion decreasing fibers soliton breakdown can be triggered when the long-wavelength ZDW is shifted towards the soliton due to the modified fiber geometry [34], [145], [282]. In this work, spectral shifts of the ZDWs to yield soliton breakdown are induced by heating a discrete fiber sections. In chapter 5 a significant blueshift of the long-wavelength ZDW is observed for increasing temperatures, resulting in a drastically narrowed AD regime. For the following numerical studies the evolution of the TM_{01} mode in a partly or entirely heated $4.0\,\mu m$ CS_2-core fiber is investigated using an experimental input spectrum with a peak power of $9.7\,kW$.

Figure 6.10 shows the spectral and temporal evolution of the TM_{01} mode when heating a central $5.5\,cm$-long fiber section or the entire fiber to $37\,°C$, and $40\,°C$. The AD regime becomes spectrally constricted in the heated fiber sections. In all thermal cases, the soliton hits the long-wavelength ZDW at propagation distances between $2\,cm$ and $4\,cm$ (e-h). The spectrally filtered temporal pulse evolutions in figure 6.10 (m-p) show that a significant amount of energy is transferred to the long-wavelength ND domain simultaneously. In the experimentally realistic case, where only the central fiber section can be thermally controlled (first and second column of figure 6.10), a first pair of DWs is already generated via soliton fission within the unheated first $2\,cm$ of the fiber (e,f). The long-wavelength phase-matched wavelength lies far in the ND regime at $3.0\,\mu m$. Consequently, the spectral overlap with the soliton is small, and the energy transfer is much weaker compared to the soliton breakdown induced DW generation in the heated fiber section. This post-fission breakdown of the fundamental soliton generates strong spectral peaks at around $2.3\,\mu m$, and $2.2\,\mu m$ for the $37°C$ and $40°C$ cases, respectively. In case of the completely heated fibers, the breakdown induced DW generation is the only
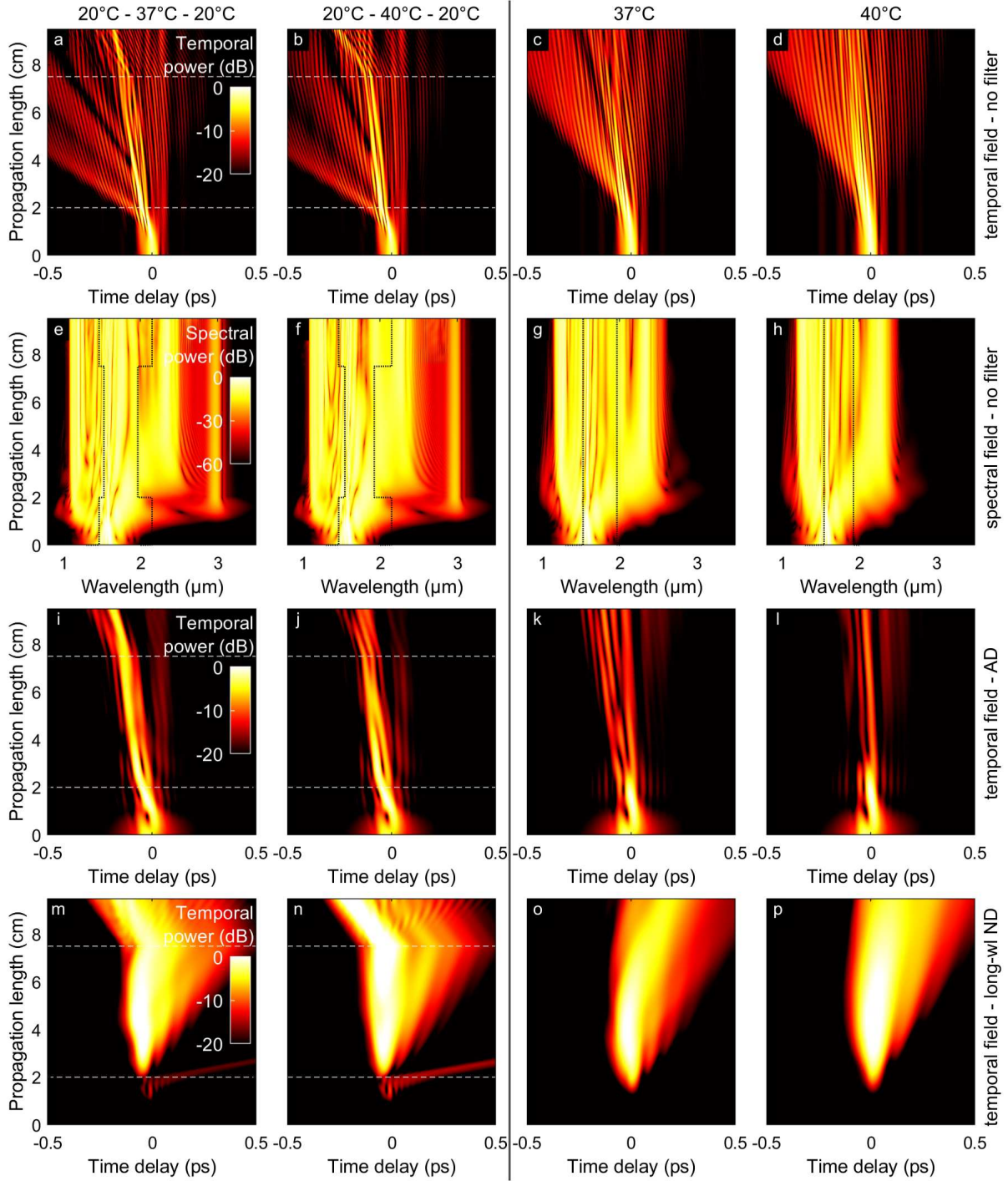
Figure 6.10: Temporal and spectral simulated evolutions of the TM$_{01}$ mode in a 4.0 μm CS$_2$-core fiber with different heating scenarios. Evolution of time delay (a-d, and i-p) and spectrum (e-h) for central section at 37°C (1st column), for central section at 40°C (2nd column), for complete fiber at 37°C (3rd column), and for complete fiber at 40°C (4th column). Different spectral filters are applied: no spectral filters (a-h), AD regime (1600 nm < λ < 1900 nm, subfigures (i-l)), long-wavelength ND regime (λ > 2200 nm, subfigures (m-p)). The subplots (a-l) are normalized to their individual maximum at 1.5 cm, the subplots (m-p) at 3.0 cm. The unheated fiber sections are at a room temperature of 20 °C. The experimental input spectrum is used. Black dotted lines in the spectral plots (e-h) show the ZDWs, black dashed lines in the temporal plots (a-d, i-p) indicate the start and end of the heated fiber section.

significant energy transfer towards the ND regimes (g,h). The pre-fission breakdowns of the higher-order solitons (soliton number 7.0 at 37°C and 12.2 at 40°C) lead to more

significant spectral gaps in the AD regime, compared to the partly heated cases. The temporal evolution plots (i-l) verify the decay of the soliton, which is especially dominant in case of the pre-fission breakdown of the completely heated fibers (k,l). Spectral changes between the different soliton-breakdown cases are also seen in the short-wavelength ND regime, but the individual spectral peaks are closer to each other and thus less easy to differentiate. The breakdown-induced power transfer to the long-wavelength DWs seems comparably efficient for the completely and partly heated fibers (e-h).
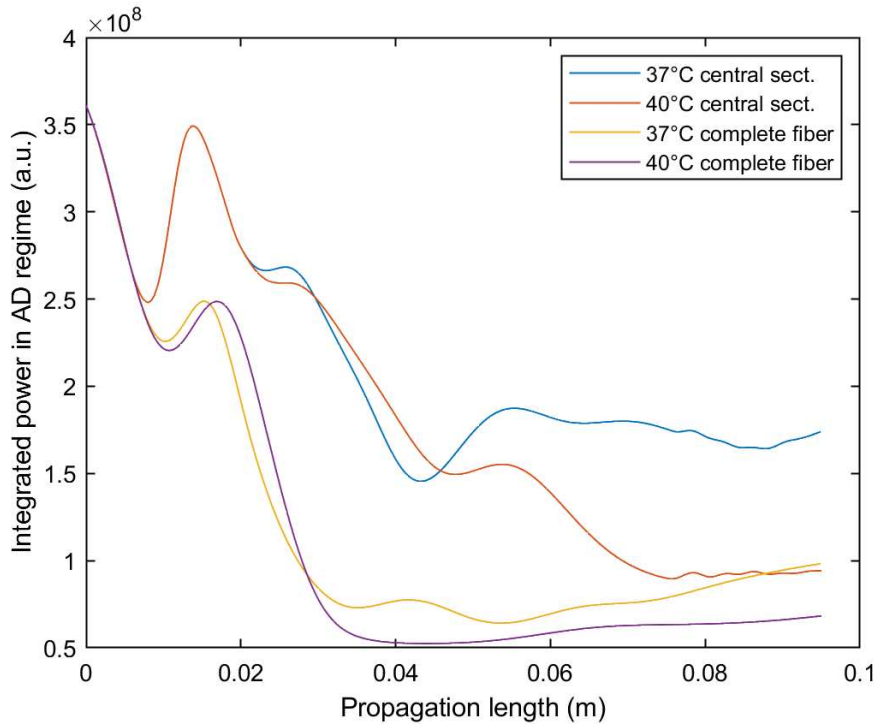
Figure 6.11: **Evolution of the overall power in the AD domain of the TM_{01} mode in a 4.0 μm CS_2-core fiber with different heating scenarios.** Power evolution in AD regime calculated from the filtered fields in figure 6.10 (e-h) with constant filter bandwidth 1600 nm < λ < 1900 nm). Summed up power in arbitrary units. Temperatures (37°C and 40°C) and heating scenario (only central fiber section heated or complete fiber heated) as given in the legend.

The power decay of the soliton is evaluated by integrating the power in a constant wavelength domain (1600 nm - 1900 nm) for all four heating scenarios in figure 6.11. For the completely heated fibers (yellow and purple curves) the power in the AD regime quickly decreases within the first 4 cm of the fiber, and only slightly rises at around 2.1 cm. For the partly heated fibers (blue and red curves), the power significantly increases around 1.9 cm due to the spectral recompression after the initial soliton fission in the unheated fiber section, before it reduces due to soliton-breakdown in the heated fiber section. While the soliton power remains almost constant at an intermediate level for both partly heated fibers, it slightly increases again towards the fiber end for the completely heated fibers. The comparably large remaining power for the partly heated fiber at 37°C can be related to the conservation of several spectral peaks in the narrowed AD regime. No power increase is detected for the higher-order soliton breakdown in the extremely narrow AD regime of the TE_{01} mode in the 3.45 μm CS_2-core fiber at room temperature

(figure 6.5). In that case the experimental input pulse showed a slight increase of the overall power in the AD regime around 2 cm as well, while the soliton power of the ideal sech-pulse reduced continuously. Consequently, the more complex pump spectrum of the experimental pulse might cause this intermediate power increase.
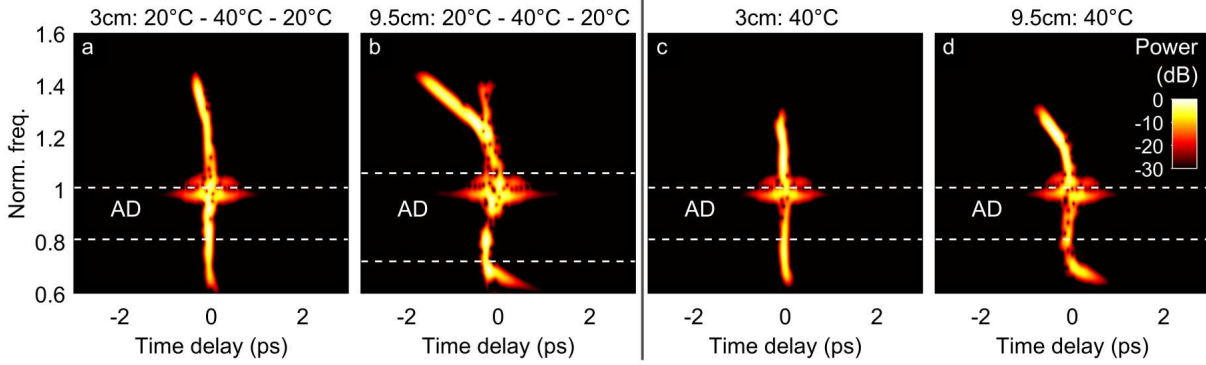
Figure 6.12: **Spectrograms at selected positions of the TM$_{01}$ mode in a 4.0 μm CS$_2$-core fiber with different heating scenarios.** The spectro-temporal correlations are displayed for the central section (a,b) and the complete CS$_2$-core fiber (c,d) heated to 40°C calculated from the temporal and spectral evolution plots shown in figure 6.7 6.10 (b,f, and d,h). The experimental input pulse is used. The white dashed lines indicate the ZDWs for the respective position in the fiber, 3 cm (a,c), and 9.5 cm (c,d).

The spectrograms at 3 cm and 9.5 cm for the partly and completely heated fibers at 40 °C shown in figure 6.12 proof the absence of a confined soliton for the completely heated fiber (c,d). In case of the partly heated fiber (a,b) some energy remains confined in the AD regime. Despite these differences, the spectrograms show a good comparability of the partly and entirely heated fiber cases. If ideal sech-squared soliton pulses are used as input, the remaining energy in the AD regime could be further reduced, as it was seen in figure 6.6 (c,d,g,h).

The simulations showed that by partly or entirely heating a CS$_2$-core fiber, pre-fission breakdown or post-fission breakdown can be obtained. The width of the narrow AD domain influences the soliton breakdown induced dual DW generation, which is much more clearly seen on the long-wavelength side than on the short wavelength side.

6.5   Temperature-induced soliton tunneling

Another soliton dynamics that can be studied in temperature-controlled CS$_2$-core fibers is the longitudinal tunneling of solitons through ND fiber sections. Therefore, the soliton needs to be excited in an AD regime at the fiber start. Afterwards, it tunnels through an ND section, before reentering an AD regime. Such a longitudinal altering GVD profile can be obtained by heating the central section of a fiber with strongly thermo-sensitive GVD or by splicing of three fibers with different GVD (compare work by Marest et al. [279]). The first and third fiber segments need to be AD at the soliton wavelength, while the second fiber section is supposed to be ND at the soliton wavelength. Considering a

HOM with two ZDWs in a CS_2-core fiber, temperature changes in a central fiber section lead to a strong decrease of the AD regime, which can be narrowed strongly enough so that it does not cover the soliton wavelength anymore. In this way tunneling through a locally restricted ND regime can be studied in LCFs.
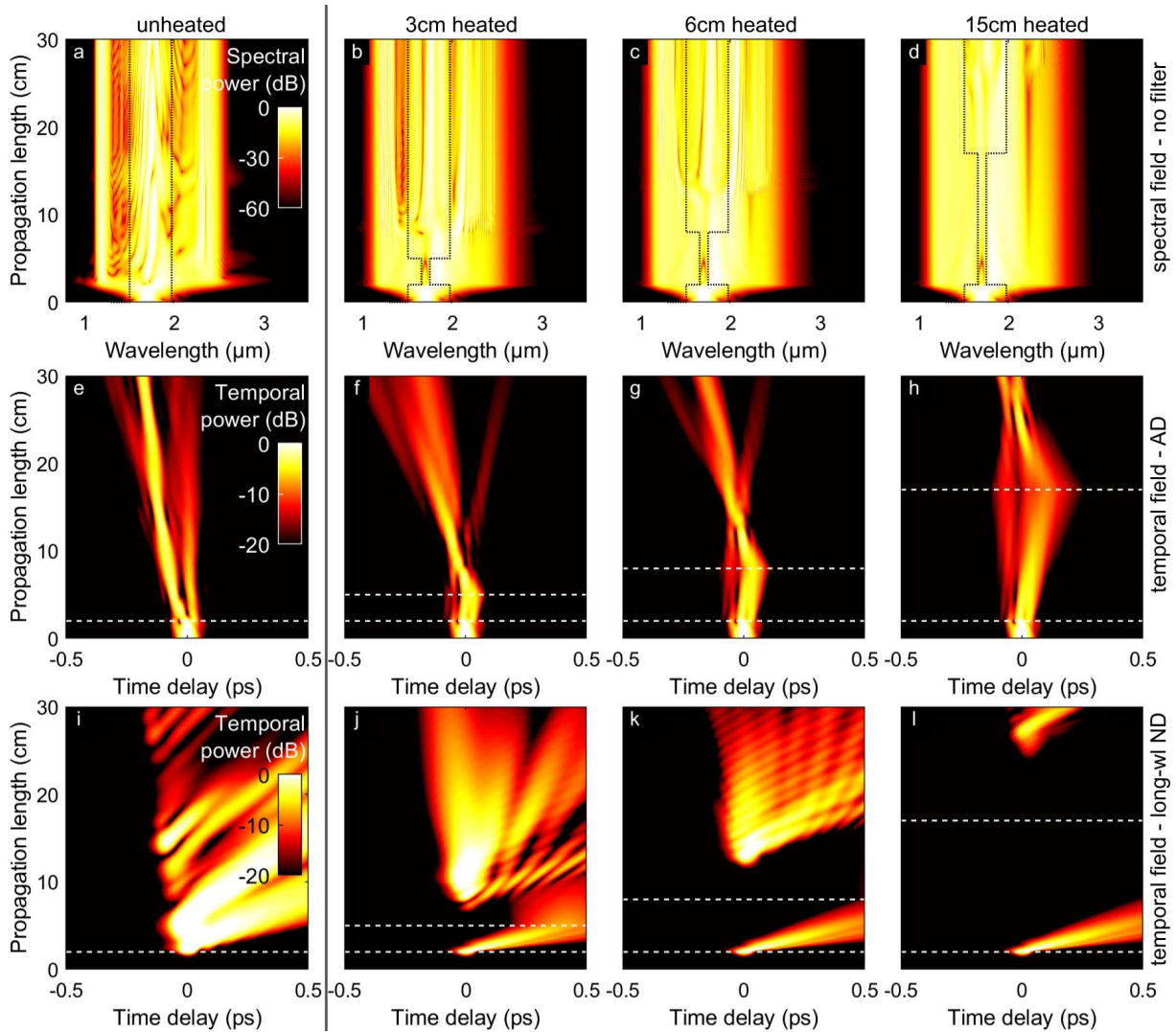
Figure 6.13: **Temporal and spectral evolutions of the TE_{01} mode in a 3.6 µm CS_2-core fiber for differently long fiber sections heated to 40°C.** The length of the heated sections are 0 cm (a,e,i), 3 cm (b,f,j), 6 cm (c,g,k) and 15 cm (d,h,l), all starting 2 cm from the fiber input. An ideal sech-squared input pulse centered at 1.70 µm and a peak power of 4.12 kW corresponding to 70% of the experimentally assumed input peak power of 6.12 kW are used. Spectral filters are applied to select the AD regime (1600 nm $< \lambda <$ 1900 nm, subfigures e-h), and the long-wavelength DWs ($\lambda >$ 2200 nm, subfigures i-l). All plots are normalized to their individual maximum shortly before the temperature step at 2.0 cm. Black dotted lines in the spectral plots (a-d) show the ZDWs, white dashed lines in the temporal plots (e-l) indicate the start and end of the heated fiber section. The unheated fiber sections are at room temperature of 20°C.

.

Figure 6.13 shows the spectral and temporal evolution of the TE_{01} mode in a 3.6 µm CS_2-core fiber with increasingly long central fiber sections that are heated to 40°C. Due to the extremely narrowed AD regime in the heated fiber section (ZDWs at 1.66 µm, and 1.75 µm, see black dashed lines) the soliton at 1.85 µm, which is generated in the wider

AD section at room temperature, propagates into the ND regime of the heated section, where it cannot exist as soliton any more, see subplots (a-d). The temporal plots of the soliton (e-h) verify a temporal broadening of the soliton pulse, followed by a strong recompression few centimeters after reentering the AD regime. This recompression is still detected for a 15 cm-long ND regime, see figure 6.13 (h), and goes along with the emission of additional DWs on the long-wavelength side, see subplots (j-l), and on the short-wavelength side (not shown here due to the relatively low contrast in comparison to the initially generated short-wavelength DW).

Tunneling of optical solitons through an ND regime can be compared with the tunneling of quantum particles through a potential barrier. This analogy was first established in 1993 [283]. Further numerical studies were conducted assuming PCFs with three or more ZDWs, where a spectrally narrow ND regime is enclosed in between two AD regimes, so that a redshifting soliton tunnels from one AD regime at shorter wavelengths to the second AD regime at longer wavelengths [183], [284], [285]. Crossing this barrier spanning a certain wavelength range can also be explained by the energy transfer between two phase-matched wavelengths in different AD regimes [286]. This does not apply for ND barriers extending along a certain propagation length, as studied in the GVD alternating spliced fiber sample by Marest et al. [279], who also referred to this process as soliton tunneling. Experimentally determining the pulse duration of the soliton before and after the ND fiber section, they showed that the soliton is recompressed to a similar temporal width in the second AD regime after being temporally broadened in the ND section. They suggest that this optical invisibility of the GVD barrier can be useful for cloaking information, because the final receiver does not observe the interim temporal broadening of the pulse.

For the temperature-induced tunneling observed in the numerical simulations of figure 6.13, the temporal dynamics of the soliton pulses are indeed modified by the tunneling through the ND regime: After recompression the pulses temporally broaden and do not show any breathing as observed in the room temperature case. So only if the fiber is cut directly at the point of recompression, the temporal profile of the soliton seems to be unchanged.

In conclusion, the numerical studies solving the GNLSE shown in this chapter suggest that cascaded DW generation due to soliton breathing, strong energy transfer due to soliton breakdown, as well as soliton tunneling can be obtained for HOMs in CS_2-core step-index fibers, if the fiber and pulse parameters are carefully adjusted. Temperature-induced modifications of the GVD can be applied to realize fine-tuning of the GVD, and longitudinal transitions to different GVD regimes allowing for soliton breakdown and soliton tunneling.

7 Experimental and numerical results on thermally controlled supercontinuum generation

By controlling the temperature of defined sections of a LCF the GVD can be modified locally. In that way, different parts of the fiber can show different dispersion regimes and changes from one dispersion regime to another can be realized within less than a minute. By using different Peltier elements, it is possible to study complex mechanisms of soliton-based SCG with a high flexibility in space and time without changing the coupling conditions to the selected LCF. In this chapter, first, the temperature is changed in a fiber section of fixed length and position, which gives control over the phase-matched wavelengths of dual DW generation. It also enables to study soliton breakdown and allows to realize a temperature-induced transition from AD to all-ND regimes. Parts of these results were published in the journal article "Temperature-Sensitive Dual Dispersive Wave Generation of Higher-Order Modes in Liquid-Core Fibers" [205]. Second, the length and position of a short temperature-controlled section is varied to manipulate the spatial and temporal delay of DW generation and to study the tunneling of optical solitons through locally restricted ND regimes. The experimental results are complemented with numerical simulations and phase matching calculations.

7.1 Influence of temperature on dual dispersive wave generation

Applying different temperatures to a fiber section of constant length and position, nonlinear soliton fission dynamics and DW generation within higher-order modes are studied dynamically in experiments and simulations. The experimental setup follows the description in section 4.2. Due to the opto-fluidic mounts, 2 cm at both fiber ends remain at room temperature of $20\,°C$, while a 5.5 cm long central section of the 9.5 cm long LCFs is cooled or heated to temperatures between $5\,°C$ and $46\,°C$. The nonlinear simulations give access to the spatio-spectral and spatio-temporal evolutions along the fiber, and provide a detailed look into the thermally modified nonlinear dynamics. Soliton breakdown and dispersive wave generation are thermally controlled.

7.1.1 Temperature-induced shifts of dispersive waves

The wavelengths of dispersive waves generated in the thermally controlled central fiber section depend on the temperature-dependent GVD of the excited mode. This thermal tuning of DWs is first studied by exciting the TM_{01} mode in a $4.0\,\mu m$ CS_2-core fiber. The commercial ultrashort fiber laser FemtoFiber pro IRs-II from Toptica (center wavelength 1570 nm, pulse duration $<40\,fs$, repetition rate 80 MHz) is used as pump in this and all following experiments.
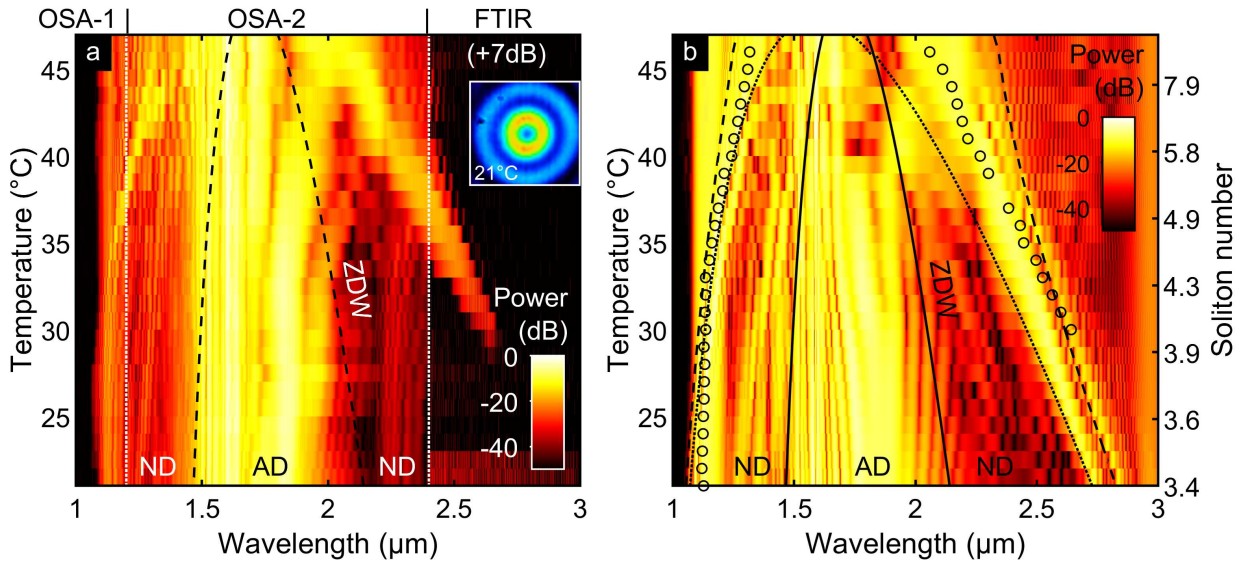
Figure 7.1: **Experimental and numerical output spectra of the TM$_{01}$ mode in a 4.0 μm CS$_2$-core fiber with different temperatures.** The ultrashort input pulse (λ_p = 1.57 μm, pulse width: 31 fs) is coupled with an in-fiber energy of 331 pJ to the 9.5 cm-long CS$_2$-core fiber, which has a temperature-controlled central section of 5.5 cm length. (a) Experimental output spectra measured with three spectrometers (as indicated at the top). For wavelengths larger than 2.4 μm, a constant offset of 7 dB is added. The dashed lines refer to the corresponding calculated ZDWs of the temperature-controlled region. The inset shows an image of the output mode at a room temperature of 21°C. (b) Corresponding simulated output spectra using the experimental input pulse. The open circles show the intensity maxima of the experimentally measured DWs, extracted from (a). The solid lines refer to the calculated ZDWs of the temperature-controlled region. The calculated phase matching wavelengths are represented by the black dashed (dotted) lines, including (excluding) nonlinear phase, assuming a constant soliton wavelength of 1.83 μm. The soliton numbers at the right axis are calculated for the first split-off fundamental soliton at an initial soliton wavelength of 1.75 μm. Reproduced and adapted under the terms of the CC-BY license [205]. Copyright 2023, The Authors, Published by Wiley.

Figure 7.1 shows experimentally recorded (a) and simulated (b) output spectra of the TM$_{01}$ mode for a fixed in-fiber pulse energy of 331 pJ (taking coupling losses into account). The temperature of the central fiber section is step-wise increased from 21 °C to 46 °C, each line of the color plot corresponding to one distinct temperature. Increasing the temperature of the central fiber section induces a shift of the two main spectral features on the long- and short-wavelength side of the spectrum towards the central AD region. These two temperature-dependent peaks can unambiguously be associated with two DWs located in the ND domains right and left of the central AD regime. The temperature-dependent ZDWs separating the different dispersion regimes are indicated as dashed and solid line in figures (a) and (b), respectively. The DWs are pumped by a soliton which is spectrally confined in the AD domain before it seems to break down at the blueshifted long-wavelength ZDW for high temperatures, which will be further evaluated later.

A beam profile of the ring-shaped measured output beam is given as inset of figure 7.1 (a) captured at a room temperature of 21°C. The additional ring around the actual TM$_{01}$ mode is artificial and resulted from imperfect imaging conditions (clipping at the lens holder). By the use of a rotatable linear polarizer its radial polarization state

could be confirmed. An additional analysis using different spectral filters proved that all characteristic wavelength features (i.e. DWs, soliton, and pump) show a TM_{01} mode profile at the fiber output, see figure 4.3 in section 4.2.3, where output spectra were demonstrated for step-wise increased input power at 37°C.

Figure 4.3 of chapter 4.2.3 shows output spectra for increasing input pulse energies for the 37°C temperature case. The observed decay of the long-wavelength DW demonstrates that the elevated noise floor of the FTIR spectrometer prevents to see weak DWs on the long-wavelength side. In addition, the absorption losses of CS_2 beyond 2.7 μm further reduce the possibility to observe the long-wavelength DWs for temperatures below 27°C in figure 7.1 (a). Simulations in (b) show that at 21°C the long-wavelength DW is supposed to be located at around 2.8 μm, which is in good agreement with phase matching conditions (dashed and dotted black lines). Furthermore, the simulation results show a weak and temperature-independent peak around 3.0 μm corresponding to a DW generated in the first 2 cm at a room temperature of 20°C. It has a slightly longer wavelength than the temperature-dependent DW at 21°C. This DW could not be detected experimentally due to the noise level of the used FTIR spectrometer. A room temperature of 20°C was chosen for the simulations even if the room temperature varied between 20°C and 21°C in experiments. The soliton numbers at the right axis of figure 7.1 are calculated for the first split-off fundamental soliton at an initial soliton wavelength of 1.75 μm considering the post-fission breakdown case. They increase from 3.4 at 21°C to 7.9 at 44°C. Exemplary values for the soliton number can be also obtained from table 7.1. Those post-fission soliton numbers are significantly lower compared to the pre-fission soliton numbers calculated for the completely heated fiber in section 6.4, where the full power of the higher-order soliton is considered as input peak power for the calculation. The soliton numbers vary slightly, when the soliton wavelength, the pulse duration or the input power, which both cannot be directly measured, are adjusted.

Table 7.1: **System parameters of two fiber configurations at selected temperatures.** Case 1: TE_{01}-mode in a CS_2-core fiber with core diameter d_{core} = 3.5 μm. Case 2: TM_{01} mode in a CS_2-core fiber (d_{core} = 4.0 μm). In both cases 2 cm at start and end of fiber remain at room temperature of 20 °C. The coupling efficiency to the respective fiber mode ϵ_c leads to a incoupled pulse energy E_f, and a soliton number N. The ZDWs are given as λ_{ZD1}, and λ_{ZD2}. The assumed soliton wavelengths λ_S are obtained from figure 7.1, and figure 7.3. The same applies for the wavelengths of the dispersive waves λ_{DWS} and λ_{DWL}, which belong to the short-wavelength side (S), and long-wavelength side (L), and were obtained from the experimentally measured spectra and the simulated spectra (sim), respectively. Reproduced and adapted under the terms of the CC-BY license [205]. Copyright 2023, The Authors, Published by Wiley.

d_{core} (μm)	mode	ϵ_c (%)	E_f (pJ)	T (°C)	λ_{ZD1} (μm)	λ_{ZD2} (μm)	λ_S (μm)	N @λ_S	λ_{DWS} (μm)	$\lambda_{DWS,sim}$ (μm)	λ_{DWL} (μm)	$\lambda_{DWL,sim}$ (μm)
3.5	TE_{01}	25%	283	5	1.47	2.01	1.75	3.9	1.07	1.16	2.47	2.44
3.5	TE_{01}	25%	283	20	1.54	1.83	1.75	9.0	1.30	1.38	2.10	2.09
4.0	TM_{01}	29%	331	21	1.47	2.14	1.83	2.7	1.13	1.12	-	2.76
4.0	TM_{01}	29%	331	37	1.53	1.97	1.83	6.3	1.19	1.20	2.38	2.35

Overall, a strong blueshift of the long-wavelength DW from 2.7 μm to 2.1 μm is experimentally detected for temperatures increasing from 28°C to 46°C, resulting in a tuning slope of $\Delta\lambda/\Delta T \approx -33$ nm/K. This surpasses other shifts reported experimentally for

thermally controlled DWs so far [118]. The circles in the simulation results of figure 7.1 (b) display the experimentally measured peak wavelengths of both DWs, which match very well with the spectral peaks obtained from simulations. For a quantitative comparison of simulation and experiment, table 7.1 shows the obtained wavelength of both DWs at two exemplary temperatures, which deviate by less than 100 nm. More important than the exact match of the wavelength is to observe comparable shifts of the DWs with temperature, which is the case at both, the short and long-wavelength side. The temperature induced shift of the DWs can unambiguously be associated with a change of the phase matching condition of soliton and DWs (i.e., Equation 2.11). Dashed (dotted) lines in figure 7.1 (b) give the phase matching wavelengths with (without) nonlinear phase $\gamma P_S/2$. The phase matching calculations confirm the strong, almost linear shift of the long-wavelength DW, as well as the weaker shift of the short-wavelength DW. The experimentally detected short-wavelength DW shifts from 1.1 μm at 20-30 °C to 1.3 μm at 46 °C. A weak spectral peak remains at 1.1 μm for all temperatures, which can be associated with a constant short-wavelength DW that is generated in the room temperature section covering the first 2 cm of the fiber.

For a more detailed analysis of the dynamics along the temperature-controlled fiber simulated spectral and temporal pulse evolutions are given for exemplary temperature scenarios in figure 7.2. A comparison of the spectra for the whole fiber at room temperature (d) and the partly heated fiber (e) (temperature of the central fiber section at 37°C) confirms that the outermost peaks of the partly heated fiber at 1.1 μm and 3.0 μm belong to DWs generated in the first 2 cm at room temperature. The pulse evolutions further show that these early generated DWs are not influenced by the following temperature section.

Another known feature of dual-ZDW systems is the soliton breathing, which is visible in the spectral evolution plot of the room temperature case in figure 7.5 (d). It manifests in the generation of additional DWs on the long-wavelength side. All long-wavelength DWs of the room temperature case lay beyond 2.5 μm and thus within the spectral domain where only the FTIR OSA with reduced contrast is available (as indicated by the gray shaded region in figure7.2(c-f)). Spectrally filtered evolution plots of this room temperature case can be found in figure 6.4 (c,g,k,o) of chapter 6, where soliton breathing was discussed using the same fiber and input pulse parameters. In subplot (k) of that figure, which shows the evolution of the temporal power distributions in the long-wavelength ND domain, the breathing induced generation of additional DWs is clearly seen. In contrast, soliton breakdown is observed for the partly and entirely heated fibers at 37°C shown in subplot (e,f) of figure 7.2. This will be discussed in more detail in the following section.
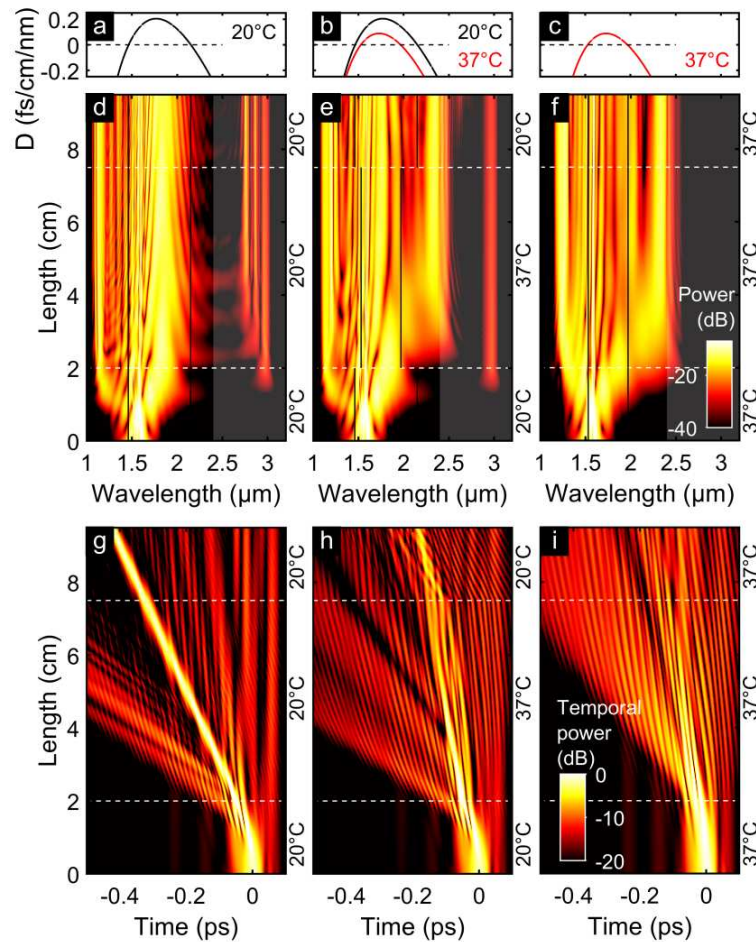
Figure 7.2: **Temporal and spectral evolutions of the TM$_{01}$ mode in a 4.0 µm CS$_2$-core fiber with different heating scenarios.** The CS$_2$-core fiber is entirely heated (right, T = 37°C, N = 6.7), partly heated (mid, T = 20 - 37 - 20 °C, N = 6.3), and non-heated (left, T = 21°C, N = 2.7). An experimental input pulse with in-fiber energy of 331 pJ is used. (a)-(c) GVD parameter D for room temperature (black) and 37 °C (red). (d)-(f) Spectral and (g)-(h) Temporal evolutions over fiber length. Note that the vertical black lines refer to the ZDWs. The location of abrupt temperature steps 2 cm apart from fiber start and fiber end are marked by white dashed lines. The color bars on the right correspond to all figures of the respective row. Reproduced and adapted under the terms of the CC-BY license [205]. Copyright 2023, The Authors, Published by Wiley.

7.1.2 Temperature-induced post-fission soliton breakdown

Besides the significant temperature-induced shift of DWs, temperature-induced soliton breakdown can be observed for the TM$_{01}$ mode in the partly heated 4.0 µm CS$_2$-core fiber shown in figure 7.1. Experimental evidence for the temperature-induced soliton breakdown is given by the lack of spectral content around the long-wavelength ZDW (1.85-1.95 µm) for temperatures above 42°C in subfigure (a). For increasing temperatures below 42°C the strong soliton peak is redshifted from 1.75 µm at room temperature to 1.9 µm at 40°C. At 42°C the soliton output peak seems to match the thermally blueshifted ZDW and strongly decays in power, while the experimentally detected long-wavelength DW strongly increases in power. Already around 34°C a weaker soliton peak is shifted outside of the AD regime while simultaneously decaying. For the simulated output spectra in figure 7.1 (b) the spectral gap around the long-wavelength ZDW

is much more prominent for temperatures above 38°C, but at the same time the power increase of the long-wavelength DW is vanishing in the simulations.

The temporal and spectral evolution plots for the central section at 37°C and the entire fiber at 37°C in figure 7.2 indicate two different scenarios of soliton breakdown: soliton breakdown of a higher-order soliton in the entirely heated fiber (f,i) and soliton breakdown of a temporally confined fundamental soliton after initial soliton fission in the partly heated fiber (e,h). The temperature-dependent ZDWs are given as black lines, the corresponding dispersion parameters D are shown in the subfigures (b-c) on the top. Spectrally filtered temporal power distributions were already discussed in figure 6.10 for partly and completely heated fibers at 37°C and 40°C.

For the experimentally implemented case of the partly heated fiber in figure 7.2 (e,h), soliton fission is observed in the room temperature section, which leads to the temporal compression of the soliton pulses and emission of dual dispersive wave. Moreover, the soliton is slightly redshifted to 1.83 µm during the fission process. This wavelength is chosen as soliton wavelength for phase matching calculations (equation 2.11) of the DWs generated in the temperature-controlled fiber section (dashed and dotted lines in figure 7.1 (b). Choosing the same soliton wavelengths for all temperature cases is justified, because the first fundamental soliton enters the heated zone under identical conditions, see spectral evolution in figure 7.2 (e). For 37°C the long-wavelength ZDW approaches and partly crosses the soliton wavelength, so that post-fission breakdown is triggered. Furthermore, the soliton number, which is supposed to be N = 1 after fission, increases due to the reduced absolute value of the GVD in the heated fiber section. This may increase the post-fission breakdown, which leads to an efficient energy transfer to an additional long-wavelength DW at 2.5 µm, seen in figure 7.2 (e). The wavelength of this secondary long-wavelength DW is strongly dependent on the temperature of the central fiber section, as observed in the experimentally and numerically obtained output spectra shown in figure 7.1. Comparing figures 7.2 (e) and (f), the temperature-dependent long-wavelength DW generated at 2.5 µm in the partly heated fiber matches the long-wavelength DW in the entirely heated fiber.

While post-fission and pre-fission breakdown result in the same wavelength of the dispersive wave, the temporal dynamics differ significantly for both cases, as seen in (h,i). Comparing the output spectra, for the completely heated fiber the power in the AD regime is significantly reduced.

The temporal dynamics of the solitons in the heated fiber sections are better resolved in figure 6.10 of chapter 6, where spectral filters for the AD regime are applied. Its subplots (i,k) unveil that the main soliton pulse remains more or less temporally confined but reduces in power when hitting the ZDW in the partly heated fiber at 37°C (i). In the completely heated fiber at 37°C (k) the temporally broad higher-order soliton broadens even stronger after its breakdown. The corresponding integrated power in the AD regime shown in figure 6.11 confirms a stronger decay of the soliton in the pre-fission

breakdown case of the completely heated fiber. The additional evolution plots for 40°C in figure 6.10 (f,h,j,l) show an even stronger decay of the temporal power in the AD region for pre-fission breakdown.

In conclusion, the analysis of the nonlinear simulations support the experimental observation of soliton breakdown, which is initiated by the heating-induced spectral narrowing of the AD regime of the TM_{01} mode in 4.0 µm CS_2-core fibers.

7.1.3   Temperature-tunable soliton fission and pre-fission soliton breakdown

Another CS_2-core fiber system is used to study the temperature-induced longitudinal transition from a narrow AD regime to a broadened AD regime and to an all-ND regime. An all-ND regime can be reached via moderate heating when exciting the TE_{01} mode in a CS_2-core fiber with a core diameter of 3.5 µm. In this case, the ZDWs are only separated by 290 nm at room temperature (see Table 7.1), and their distance can be further reduced by heating the fiber until for temperatures above 26 °C all-ND is obtained. By heating the fiber and reducing the AD regime pre-fission soliton breakdown can be tuned. Cooling the same fiber the ZDWs are shifted away from the pump leading to a significantly broadened AD regime and thermal-control over soliton fission. In the experimental case, again the first 2 cm of the fiber remain at room temperature and only the temperature in the central section of 5.5 cm length is heated or cooled. Consequently, a soliton can be excited in the narrow AD regime of the 2 cm long room temperature section at the fiber start and will be propagating into the all-ND regime of the heated fiber section or into the broadened AD regime of the cooled section.

Figure 7.3 shows the experimental and simulated output spectra for the central fiber section being heated up to 55°C and cooled down to 5°C. Due to the slightly lower coupling efficiency of $\epsilon_{coupl}(TE_{01}) = 25\%$ to the smaller fiber core of 3.5 µm, the in-fiber energy considered for experiments and simulations is 283 pJ, and thus slightly lower in comparison to the TM_{01} mode investigations in the 4.0 µm fiber (details in Table 7.1). As observed in the previous fiber setup, both ZDWs approach each other for increasing temperatures, see black dashed/solid line in figure 7.3 (a/b). The two ZDWs merge for 26°C at a wavelength of 1.67 µm, inducing an all-ND regime for higher temperatures. Cooling the fiber, both ZDWs shift away from the pump leading to a broader AD regime with increased absolute dispersion at the pump wavelength. Due to the experimental restrictions, again, the fiber start (and end) always remain at room temperature. Consequently, for all temperatures between 27 °C and 55 °C, the pulse undergoes an abrupt transition from AD within the first 2 cm of the LCF at room temperature towards an all-ND domain in the following heated region. Thus, in the first section a higher-order soliton can be generated (soliton number $N \approx 9$), which is expected to disperse in time in the heated section, because stable soliton propagation is not supported in the all-ND regime. Also tunneling through the all-ND region is an option, but is not observed in this case. A reason for this is most probably the narrow AD regime at room temperature,
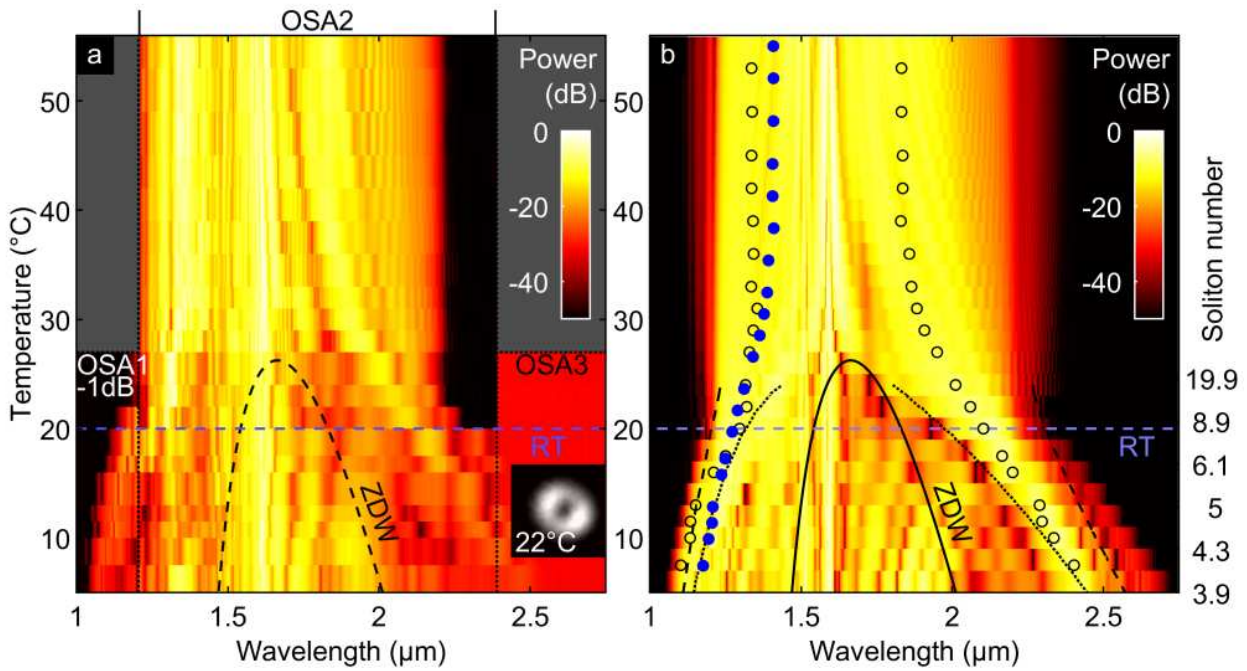
Figure 7.3: **Experimental and numerical output spectra of the TE$_{01}$ mode in a 3.5 μm CS$_2$-core fiber with different temperatures.** The 9.5 cm-long CS$_2$-core fiber includes a temperature-controlled central section of 5.5 cm length. (a) Experimentally measured spectra for temperature ranging from 6 °C to 56 °C. The inset shows an image of the output mode at 22°C. The black dashed line indicates the calculated temperature-dependent ZDWs. The blue dashed line indicates the room temperature (RT) of 20°C. Note that above 26 °C the heated region is all-ND across the entire spectral region of interest. The spectra are obtained with three different spectrometers. No data is available in the gray regions. (b) Corresponding simulated output spectra using the experimental input pulse. The black solid line indicates the calculated temperature-dependent ZDWs. Open black circles show the intensity maxima of the experimentally measured peaks, extracted from (a). The blue filled dots show the four-wave mixing phase matching wavelengths with pump and long-wavelength DW. The dashed (dotted) lines in (b) refer to DW phase matching including (excluding) nonlinear phase, assuming a constant soliton wavelength of 1.75 μm. The same soliton wavelength is used to calculate the soliton numbers at the right axis. Reproduced and adapted under the terms of the CC-BY license [205]. Copyright 2023, The Authors, Published by Wiley.

and the short fiber section behind the all-ND section. In the case of a centrally cooled fiber segment, the pulses in the AD domain abruptly transit from a narrow AD regime to a wider broadened AD regime, where temporally compressed solitons are observed in the temporal evolution plots, see figure 7.5 (l).

The most prominent features of figure 7.3 showing experimentally and numerically obtained output spectra for varying temperature in the central fiber section are the significantly shifting DWs at both sides of the spectrum. Step-wise decreasing the temperature in the central fiber section from 26 °C to 6 °C, both DWs, which are located at the short- and long-wavelength side of the spectrum, shift away from the pump. The experimental spectra in (a) are measured with three different spectrometers (OSA-1: Q6317B, OSA-2: AQ6375, OSA-3: OSA205) as indicated by the black dotted lines, and no data is obtained in the gray regions. The inset shows the ring-shaped intensity profile of the output pulse at 22°C, whose azimuthal polarization distribution could be verified by observing the intensity distribution behind a rotating linear polarizer. In contrast to the former case

with the TM$_{01}$ mode in a 4.0 µm fiber, both short- and long-wavelength DWs can already be detected experimentally at room temperature (figure 7.3 (a)) because of the stronger spectral overlap of the soliton to the closer phase-matched wavelengths. The phase matching wavelengths for the temperature-modified fiber sections are given as dashed (dotted) lines considering (no) nonlinear phase in figure 7.3 (b). They are calculated for a fixed soliton wavelength of 1.75 µm and shift towards the ZDWs with increasing temperature due to the decreasing AD regime. The phase matched wavelengths of DWs with the soliton can only be calculated in the temperature range that shows an AD-regime by using equation 2.11. The calculated phase matching wavelengths show similar spectral positions and temperature-induced shifts as the experimentally and numerically detected DW peaks.

For the central fiber section being heated above 26°C the spectral peaks in the short- and long-wavelength side are still present in the experimental and numerical output spectra, and continue shifting towards the central pump wavelength. They result from the breakdown of the soliton excited in the unheated fiber start, when propagating into the heated all-ND fiber section. The spectral positions of these peaks match very well in experiments and simulations, see black circles in figure 7.3 (b) representing the experimentally obtained peak wavelengths. The blue filled circles indicate the temperature-dependent phase-matched wavelengths λ_{FWM} of degenerated four-wave mixing between a pump at $\lambda_{pump} = 1600$ nm and the experimentally obtained long-wavelength DW at λ_{DW2} as idler (black circles on the right). The underlying phase matching equation for the propagation constant β reads: $\beta(\lambda_{FWM}) = 2 \cdot \beta(\lambda_{pump}) - \beta(\lambda_{DW2})$. As the calculated four-wave mixing wavelengths match with the experimentally and numerically obtained short-wavelength peaks this suggests a coupling between DW generation and degenerated four-wave mixing in the case of soliton breakdown induced energy transfer from the AD to the ND-regime. For all temperatures cases above 26 °C that evolve an all-ND domain the overall spectral bandwidth ranging from 1.2 µm to 2.2 µm (measured at 20 dB spectral contrast) remains constant. The output spectra for the temperature cases with a narrow AD regime (15°C < T < 25°C) do not show a strong soliton peak in the AD regime, which can be explained by soliton breakdown at the close long-wavelength ZDW.

This soliton breakdown can be studied in experimental measurements and numerical simulations of the room temperature case, when the in-fiber pulse energy is step-wise increased, see figure 7.4. For increasing pulse energy the soliton peak in the AD regime shifts towards longer wavelengths until it hits the long-wavelength ZDW at approximately 100 pJ. For further increasing pulse energies the peak does not continue to redshift continuously, but transfers a lot of its energy to wavelengths in the ND domains. A slight power transfer to both ND domains is already observed for lower energies where the soliton is barely overlapping the long-wavelength ZDW. In this case soliton fission might be the driving force for the energy transfer to the DWs. The power transfer drasti-
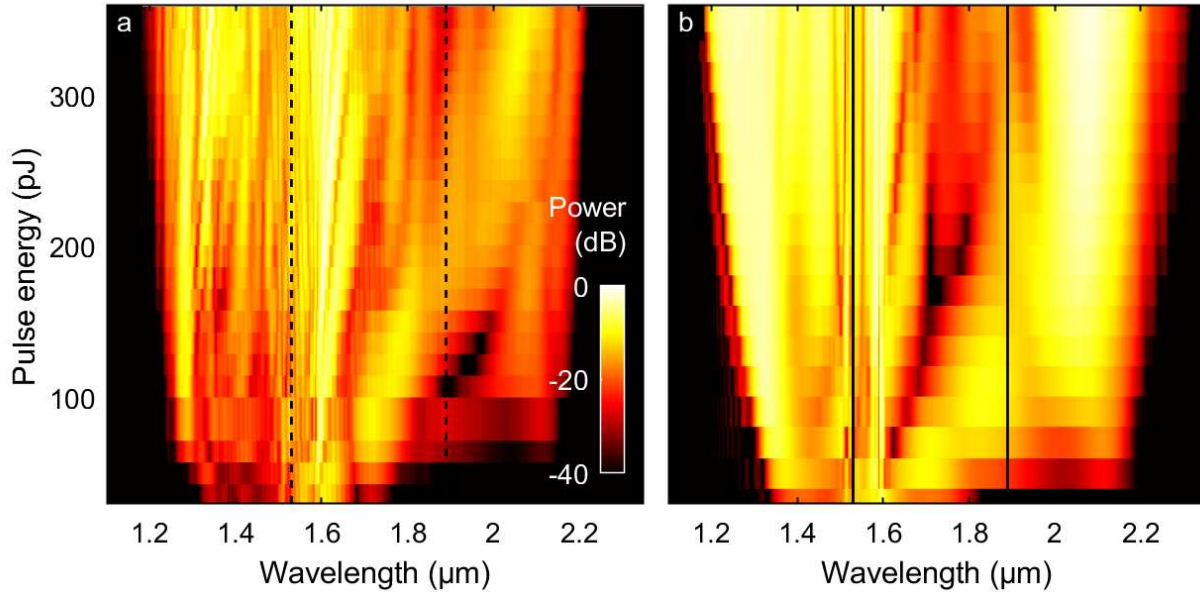
Figure 7.4: **Experimental and numerical output spectra of the TE$_{01}$ mode in a 3.5 μm CS$_2$-core fiber at room temperature with different input pulse energy.** Output spectra of the 9.5 cm-long CS$_2$-core fiber at room temperature are given for increasing in-fiber energies. (a) Experimentally measured spectra. The black dashed lines indicate the ZDWs. The spectra are obtained with the spectrometers AQ6317B, and AQ6375, see table 4.1. (b) Corresponding simulated output spectra using the experimental input pulse. The black solid lines indicates the ZDWs. Reproduced and adapted under the terms of the CC-BY license [81]. Copyright 2021, The Authors, Published by Springer Nature.

cally increases due to soliton-breakdown at around 100 pJ for the short-wavelength and long-wavelength side simultaneously in experiments, as well as in simulations. Additional wavelength peaks are observable at the short-wavelength side between the short-wavelength DW and the ZDW. Both studies show a clear spectral gap between 1.7 μm and 1.9 μm for pulse energies above 200 pJ.

More insights into the nonlinear dynamics of this system can be obtained from the simulated spectral and temporal pulse evolutions along the temperature modified fiber, which are shown for exemplary temperatures in figure 7.5.

A comparison between SCG in the partly and completely temperature-controlled fiber is given for exemplary temperatures (and room temperature) in figure 7.5. If the whole fiber is at room temperature (a,f,k), higher-order soliton breakdown is observed around 2.5 cm after the fiber start. At this propagation distance a strong long-wavelength DW at 2.1 μm is generated when the peak in the AD regime hits the ZDW and gets almost completely depleted. As no soliton fission is observed in the first 2 cm of the room temperature case, also no DW generation takes place in this fiber before the temperature-controlled central fiber section starts. After 2 cm at room temperature the pulse is slightly spectrally broadened and the soliton is shifted towards the long-wavelength ZDW. Numerical pulse evolution plots for the room temperature case in a very similar CS$_2$-core fiber of 3.45 μm core diameter were already discussed in chapter 6, see figures 6.2 (a,b,e,f), and 6.4 (a,b,e,f,i,j,m,n) with spectral filters applied.
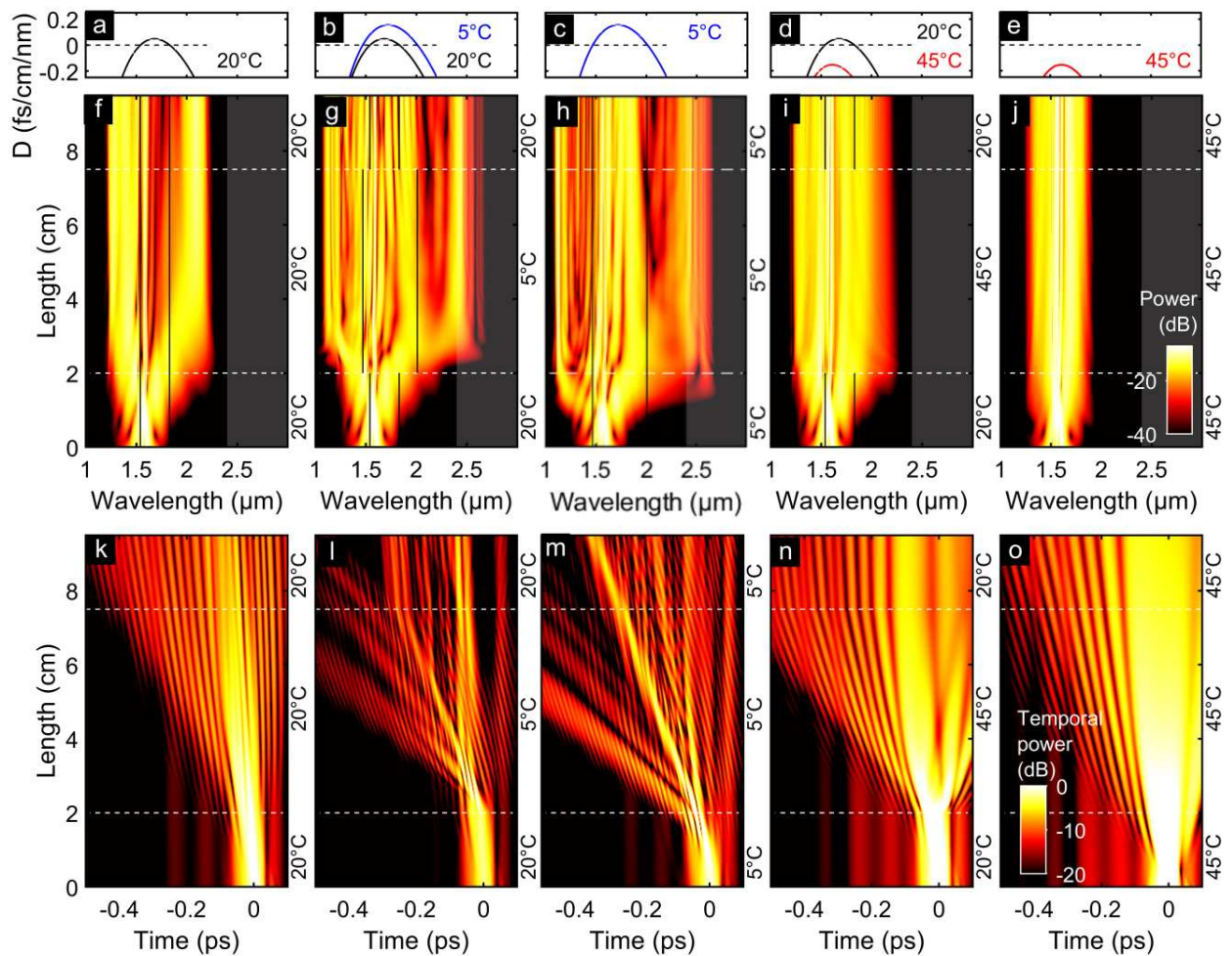
Figure 7.5: **Temporal and spectral simulated evolutions of the TE$_{01}$ mode in a 3.5 μm CS$_2$-core fiber for different temperature scenarios.** Simulations for room temperature (a,f,k), for a partly cooled fiber (b,g,l), and a party heated fiber (d,i,n), which correspond to selected output spectra of figure 7.3. To investigate the influence of the unheated fiber start and end, simulation results for an entirely cooled fiber (c,h,m) and for an entirely heated fiber (e,j,o) are shown as well. The solid black lines in the spectral evolution plots show the local ZDWs. The white dashed lines in the temporal plots indicate the start and end of the temperature controlled fiber section. Figures (a-e) show the corresponding GVD parameters for room temperature of 20 °C (black), for 5 °C (blue), and for 45 °C (red). Reproduced and adapted under the terms of the CC-BY license [205]. Copyright 2023, The Authors, Published by Wiley.

Studying the partly heated fiber case spectral and temporal evolution plots are shown in figure 7.5 (i,n) for the transition to an all-ND regime (central fiber section at 45°C). The evolution plots demonstrate that the spectral bandwidth is not increased in the all-ND fiber section, and the initially temporally confined pulse splits into at least two pulses at the beginning of the all-ND region, which disperse strongly during their further propagation. The last 2 cm at room temperature with narrow AD region do not influence the spectral or temporal distribution significantly, and no soliton recompression and thus tunneling is observed.

For the completely heated fiber (figure 7.5 (e,j,o) at 45°C), which is all-ND over the whole fiber length, there is less spectral broadening at the beginning of fiber and the overall bandwidth remains narrow, spanning 600 nm only. To obtain significant broadening

via self-phase modulation in a completely all-ND fiber higher peak powers might be required [253], [287], [288].

In the partly cooled fiber, choosing 5°C as exemplary temperature in figure 7.5 (b,g,l), dual-DW generation takes place in the broadened AD domain of the cooled fiber section After the fission process, the soliton remains close to the long-wavelength ZDW in the AD regime, but has reduced in energy. When passing through the fiber end section at room temperature this soliton does no more lie within the narrowed AD regime, but its temporal dispersion seems negligible due to the short propagation distance in the ND regime. In case of the entirely cooled fiber (figure 7.5 (c,h,m) at 5°C) both, long- and short-wavelength DWs, are generated at a propagation distance of around 1.8 cm at comparable wavelength than in the partly heated fiber. Surprisingly, the intensity of the long-wavelength DW is significantly lower compared to the partly cooled fiber.

In conclusion, temperature control of the soliton dynamics of a TE_{01} mode in the 3.5 µm CS_2-core fiber is demonstrated experimentally, and shows soliton transitions from narrow AD regimes to broadened AD regimes, as well as to all-ND regimes. The experimentally obtained shifts of the generated DWs are in excellent agreement with simulations. The simulations unveil the soliton dynamics, e.g. the breakdown at the transition to all-ND regimes. The partly temperature-controlled fiber cases are compared with theoretically homogeneously heated or cooled scenarios. For both cases the narrow AD regime at the initial room temperature section is favorable for the spectral broadening, increasing either the bandwidth or the coupling efficiency to the long-wavelength domain.

Summarizing the whole section, heating and cooling a constantly long fiber section of CS_2-core fibers leads to modifications of the nonlinear dynamics of solitons excited in HOMs with curved GVD profiles. Strong tuning slopes of temperature-modified DWs up to 33 nm/K are obtained experimentally, and supported by simulations and phase-matching calculations. Experimental results and simulations solving the GNLSE match well, when studying soliton breathing, soliton breakdown and transition to all-ND regimes in temperature-controlled fibers. Pre-fission and post-fission soliton breakdown is observed and modified via temperature.

7.2   Dependence on heating length and heating position

Apart from absolute changes in temperature, which homogeneously modify the dispersion of a certain fiber section, also the location and length of the dispersion-modified fiber section influences the nonlinear dynamics of soliton-driven SCG. A first proof for this gave the comparison of simulated SCG in completely and partly temperature-controlled LCFs discussed in the previous sections. This will be further extended by varying the length and position of heated fiber sections.

Longitudinal tuning of the GVD has already been realized in differently modified fibers to study various special nonlinear effects: Tapering is one common longitudinal waveguide tuning method, where the locally strongly reduced core size leads to dispersion changes as well as strong mode area confinement [37]. Similar to the tapering technique, core diameters are continuously reduced along the fiber to obtain dispersion decreasing fibers [34], [58], [289] that are for example compressing chirped pulses [290]. Fibers with periodically varying diameters are used to study quasi-phase matching in dispersion varying fibers [142], [145]. Another approach to realize quasi-phase matching is modulating the coating thicknesses along exposed core fibers [291]. Furthermore, splicing of fiber sections with different core sizes, e.g. to study soliton tunneling on a ND barrier [279], was realized before. In comparison to these static fiber (post) processing techniques, the temperature approach benefits from its flexibility and reconfigurability. Here, experiments and simulations with different heating lengths and heating positions are conducted with the same 3.6 μm CS_2-core fiber under unchanged coupling conditions.

7.2.1   Local and temporal fission control via modified heating lengths

In this section the influence of the length of a dispersion modified region is studied exemplarily for the TE_{01} mode in a 3.6 μm CS_2-core fiber. In fact, for short heating lengths (< 3 cm), for which the AD regime of the excited TE_{01} mode is strongly narrowed, there is no prominent change of the soliton dynamics detected inside the heated fiber section. But it is observed that the length of the heated fiber section determines the onset of a retarded fission, which is triggered in the room temperature section following the heated zone. A recompression of the pulse after the heated fiber section leads to the generation of additional DWs. The propagation distance at which this recompression-induced fission takes place can be shifted along the fiber by extending the heated fiber section. This thermal approach gives control over the retarded soliton dynamics in a very flexible way.

Figure 7.6 shows output spectra and thermal images for increasing lengths of a constantly heated fiber section. In the experimental setup more and more small Peltier elements are heated to successively increase the length of the temperature-controlled fiber section. The temperature of all heated elements is either set to 30°C (a-c) or 40°C (d-f). The first heated element is constantly located 2.3 cm from the fiber start, and each element is considered to heat a 3 mm-long fiber section homogeneously. Consequently, when the maximum of 10 Peltier elements is activated, the heated zone is 10 cm long. The CS_2-core fiber is placed above this Peltier element row and covered by small heat mats which match the dimensions of the individual Peltier elements, see figure 4.4 in chapter 4.2.3. The fiber cannot be seen in the thermal images of figure 7.6 (c,f). Its incoupling side is on the left. Due to thermal coupling between the Peltier elements, the neighboring element right of the last heated element has a temperature higher than
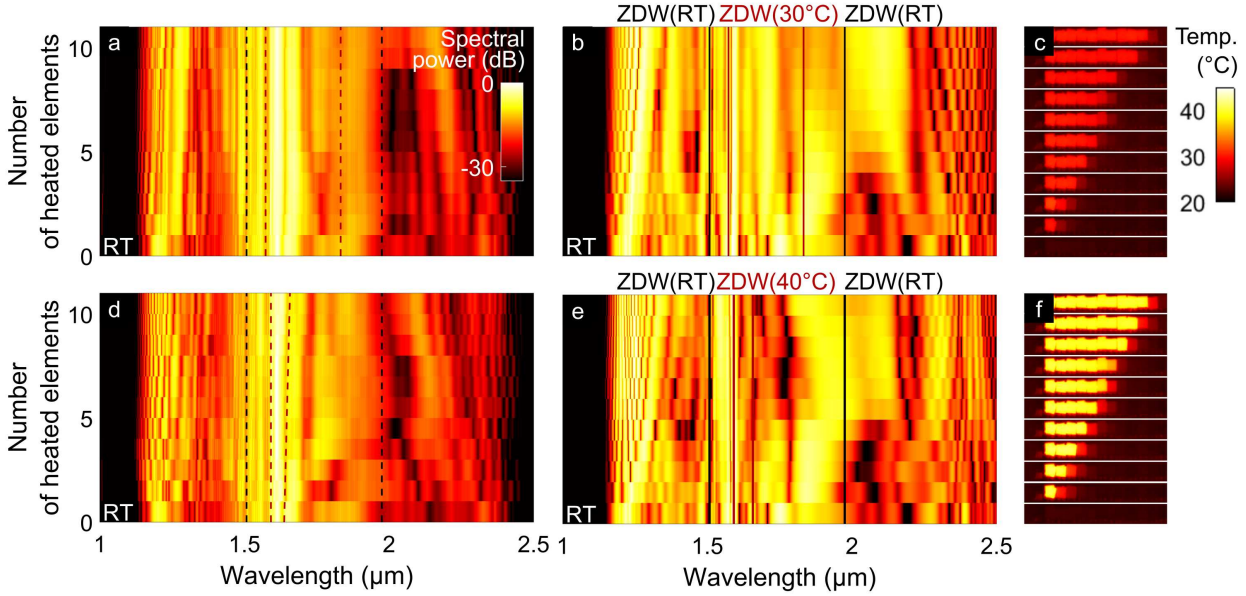
Figure 7.6: **Experimental and numerical output spectra of the TE$_{01}$ mode in a 3.6 μm CS$_2$-core fiber with different heating lengths.** From bottom to top, one to ten consecutive Peltier elements of 3 mm length are heated to 30°C (a-c) and 40°C (d-f) starting 2.3 cm from the fiber start. The first line shows the output spectra for the whole fiber at room temperature. (a,d) Experimental output spectra measured with OSA AQ6375. (b,e) Numerical spectra are obtained using experimental input spectrum with a peak power of 6.124 kW. The ZDWs for heated/unheated fibers are given as red/black (dashed) lines. All spectra have the same color scale as shown in (a). (c,f) Experimentally detected thermal images showing a top view of the increasing number of heated Peltier elements on a room temperature (RT) background of 20°C. The color bar at the right corresponds to all thermal images.

room temperature, which is actively set to a constant value of 25°C in (c) and 30°C in (f) for all heating lengths in the experiments to guarantee comparability of the results. Test simulations (not shown here) proved that this intermediate step between the heated section and the following fiber section at room temperature does not affect the simulation results significantly, hence a single temperature step from 30°C or 40°C to room temperature is implemented in the simulations. Figure 7.6 shows the experimental (a,d) and simulated (b,e) output spectra for an increasing number of heated elements. Pulses relying on the experimental input spectrum are used as simulation input. In experiments and simulations a TE$_{01}$ mode is excited with a pulse energy of 216 pJ (and peak power of 6.124 kW) in a 13.5 cm long CS$_2$-core fiber with 3.6 μm core diameter using the commercial femtosecond Toptica laser as shown in figure 4.1 of chapter 4.2.3.

The simulation results of 30°C in figure 7.6 (b) match well with the experimental results in (a): the soliton peak around 1.88 μm is slightly shifted to longer wavelengths for short heating lengths between 3 mm and 12 mm, the long-wavelength edge of the long-wavelength DW is blue shifted from approximately 2.26 μm to 2.16 μm and the short-wavelength side shows a constant short-wavelength edge with increasing modulated width for increasing heated length. The long-wavelength ZDW for 30°C indicated as black dotted line in figure 7.6 (b) is overlapping the soliton peak at 1.83 μm, thus its long-wavelength side experiences weak ND in the heated fiber section. Both, experiments and simulations, show fringes on the short- and long-wavelength edge of the

spectra, which are caused by temporal interference. These fringes become narrower for increasing heated lengths, and are an indicator for the temporal delay between an initial DW generation before or within the heated fiber section and another retarded DW generation behind the heated fiber section. The interference fringes are caused by the additional DW generation after tunneling. Even if no additional clearly separated DW peaks could be detected on the short-wavelength side, the fringes can be interpreted as experimental evidence for soliton tunneling. Note that no fringes are detected on the short-wavelength side for the room temperature case, neither in experiments nor in simulations.

For 40°C the long-wavelength ZDW is blueshifted to 1.66 µm and thus the soliton wavelength is completely in the ND region for the length of the heated region. In the 40°C case the simulation result in figure 7.6 (d) matches the experimental results in (e) less well than for 30°C. Nevertheless, both show similar fringes on the short-wavelengths side and a redshift of the soliton output wavelength for intermediate heating lengths. The evolution of the long-wavelength side with increasing heating length is not perfectly matching in experiments and simulations with 40°C. One reason might be the discrepancies between the real temperature distribution along the fiber and the constantly heated fiber section used in simulations or slight deviations of the room temperature, which was set to 20°C, for the overall best match, even if the manually measured room temperature of 22°C was slightly above. Further uncertainties that justify the differences between simulation and experiment are the unknown exact pulse duration and peak power at the incoupling position of the fiber, as well as deviations of the TOC model of CS_2 from its real temperature dispersion. Also slight mismatches of the other material properties, e.g. the nonlinear parameter, can lead to differences between simulations and experiments.

The evolutions of temporal and spectral power distributions are shown for selected heating lengths at 40°C in figure 7.7. The AD regime and the long-wavelength ND regime are spectrally filtered, as described in the figure caption to discuss the influence of the reduced AD regime and the expected soliton tunneling dynamics. In contrast to the simulated pulse evolutions shown in figure 6.13 of section 6.5, here, an experimental input pulse is used. Moreover, the heating and fiber lengths discussed in the previous chapter, were chosen to be approximately three times longer than in the real setup. To anticipate the outcome: The soliton passes the ND regime in the heated fiber section without broadening significantly, and further DWs are generated once it reentered the AD regime. This results in a spatial delay of the additional DWs, which are only generated behind the dispersion decreased fiber section but not within. Consequently, the location of the additional fission points and the temporal delay between the first and second fission can be controlled by the length of the heated fiber section.

For the room temperature case in figure 7.7 (a,e,i,m) multiple DWs are generated at the
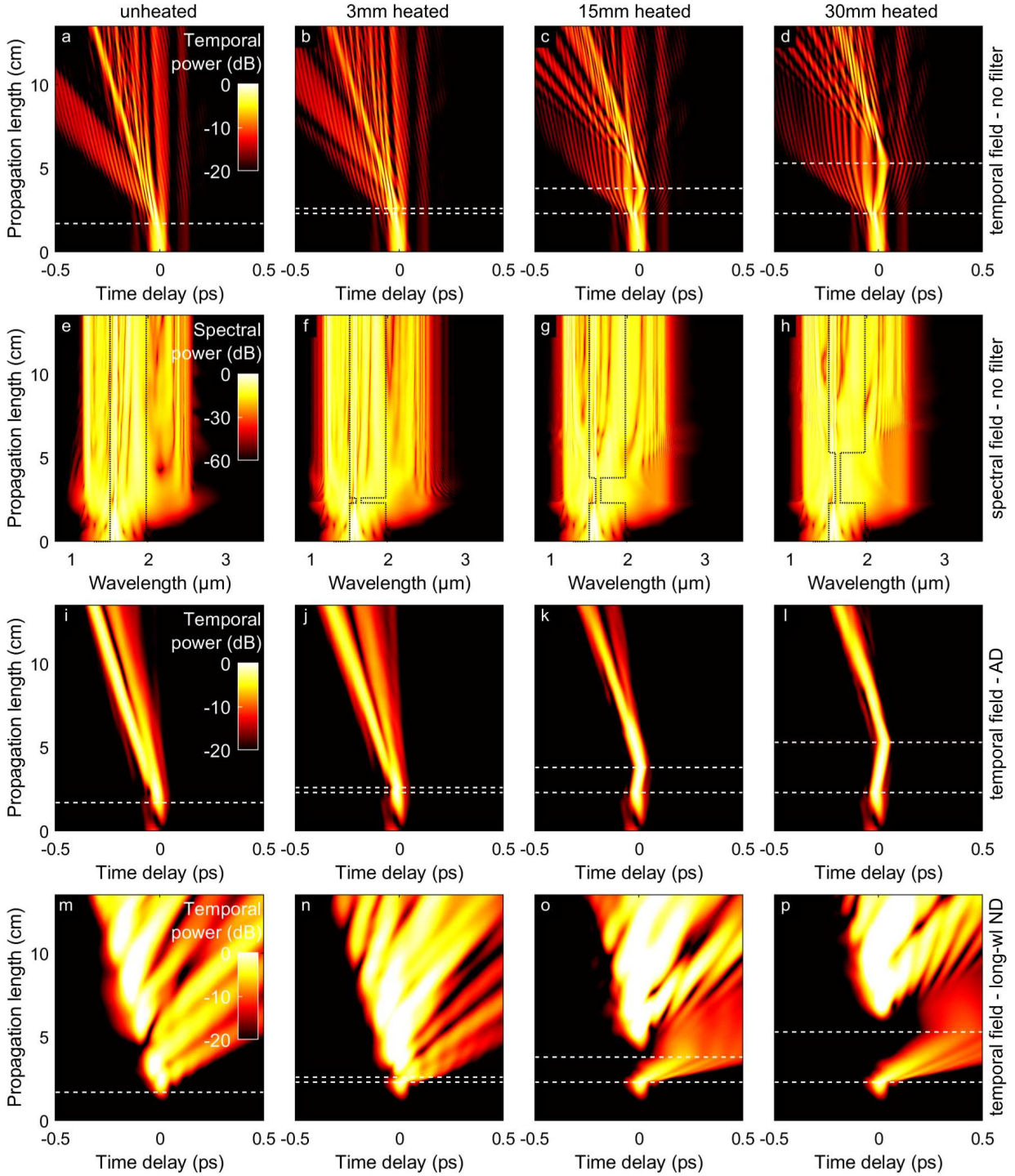
Figure 7.7: **Spectrally filtered simulated temporal and spectral evolutions of the TE$_{01}$ mode of a 3.6 µm CS$_2$-core fiber for different heating lengths.** Differently long fiber sections heated to 40°C: 0 mm (a,e,i,m), 3 mm (b,f,j,n), 15 mm (c,g,k,o), and 30 mm (d,h,l,p), corresponding to the output spectra of 0, 1, 5 and 10 heated elements in figure 7.6. Full temporal (a-d) and spectral (e-h) power distribution evolutions with fiber length, as well as spectrally filtered temporal power distributions (i-p) are shown. Spectral filters are applied to select the AD regime (1600 nm < λ < 1900 nm, subfigures i-l), and the long-wavelength ND regime (λ > 2200 nm, subfigures m-p). All power distribution evolution plots are displayed in logarithmic scale, and normalized to their own maximum at 2.3 µm, right before the heated section starts.

long-wavelength side, see spectrally filtered temporal pulse evolution in (m). The soliton remains temporally confined, but no periodic temporal compression is observed in (c). Clear breathing of the soliton is only observed in the longer fiber shown in figure 6.13.

This stability of the soliton is in contrast to the previous studies shown with TE_{01} modes in 3.45 µm and 3.50 µm CS_2-core fibers, which both showed soliton breakdown, due to the slightly smaller core diameter. For this fiber which has a core diameter of 3.6 µm, the ZDWs are located at 1.51 µm, and 1.98 µm, see vertical lines. Consequently, the AD regime is wide enough to maintain the soliton after the first fission process and support soliton breathing at room temperature for a soliton number of $N = 4.8$, and a nonlinear length of $N_{NL} = 2.6$ mm. The first soliton fission occurs at around 1.6 cm and generates a short- as well as a long-wavelength DW. The calculated fission lengths $L_{fiss} = 1.35$ cm is a bit shorter. The initial soliton shown in (c) seems to splits into two at around 5 cm and while the stronger soliton pulse remains temporally confined, the weaker pulse seems to weakly disperse in time for increasing propagation lengths.

The pulse evolutions for selected heating lengths of 3 mm, 15 mm, and 30 mm in figure 7.7 show the tunneling of the soliton through the differently long ND regimes at 40°C. At this temperature the AD region is extremely narrow and centered around 1.63 µm. For an increasing long heated fiber section that is tunneled by the soliton, the additional soliton fission taking place afterwards is successively delayed. This implies that the generation of additional long-wavelength DWs (n-p) is shifted to longer propagation lengths from around 3 cm (f,n) to 7 cm (h,p), when the heated length is increased from 3 mm to 30 mm. At the second fission point the soliton also shows a splitting in the temporal domain (j-l) and a step-like redshift in the spectral domain (f-h). The generation of additional short-wavelength DWs can be barely seen in the overall spectral evolutions (e-h), but as new modulated features splitting to the right in the temporal plots (b-d).

The controllable delay of the second soliton fission influences the interference of the initially excited DW with the DWs triggered after the heating section, which results in decreasing fringe distances for increasing delay along the propagation length. This can be seen at the short- and long-wavelength side in the experimental and numerical overall output spectra of figure 7.6 for 30°C (a,b) and 40°C in (g,h). The interference fringes can be also seen in the spectral evolution of the long-wavelength DW for one heated Peltier element (m), but they become too narrow to be displayed in the chosen wavelength scale for longer fission delays in (n) to (p). In the temporal evolution plots of figure 7.7 narrowed interference fringes can be also seen in (d) compared to (c).

For all cases, the soliton does not experience any dominant spectral broadening while propagating through the ND regime. The calculated dispersive length is 3.3 cm at 40°C, and 6.5 cm at room temperature. Even if this matches the length scales of the maximum 3 cm long temperature-controlled section of this 13.5 cm-long CS_2-core fiber the dispersion seems to play a minor role and other effects like the temporal recompression behind the ND region dominate.

As shown in figure 6.13 of chapter 6 soliton tunneling and resultant recompression-induced fission can be achieved for even longer heating length of up to 15 cm. This can be realized experimentally with CS_2-core fibers, by increasing the fiber length and the

amount or length of the lined-up Peltier elements.

7.2.2 Local fission control via modified heating position

The influence of the spatial position of the dispersion modified region is examined in this section. For all cases the temperature step is kept constant from 20°C to a 3 mm-long section at 40°C, and back to 20°C, while its position is shifted along the fiber. Studying the output spectra of experiments and simulations, both are influenced by the heating location. It is found that the transition from the short heated region with ND at the soliton wavelength back to AD in the remaining fiber section at room temperature, triggers energy transfer to long-wavelength DWs few millimeters behind the heated region as know from soliton tunneling [279]. As the heated section has a constant length no significant change of the temporal delay is observed as it had been the case for the different heating lengths in the previous section 7.2.1. These findings will be discussed comparing experimental and numerical output spectra, and evaluating selected simulated pulse evolutions.

The experiment to study the influence of the heating position is conducted, using the same row of 3 mm-long Peltier elements as in section 7.2.1. Now, one element after each other is heated to 40°C to realize the changing heating position in the experiment. Due to thermal coupling of neighboring Peltier elements, the temperature of the direct neighbors are set to 30°C for comparability. The first heated Peltier element is located 2 cm from fiber start and does not have any neighboring Peltier element towards the fiber start, as it can be seen from the thermal images in figure 7.8 (c). The thermal images also show that there was an erroneous temperature pattern applied for heating position 7 and a slightly reduced temperature applied for position 9. In simulations a direct step from 20°C to 40°C at correspondingly shifting heating positions is analyzed. As in the previously discussed experiments a TE_{01} mode is excited in a CS_2-core fiber with 3.6 μm core diameter and 13.5 cm length at a peak power of 6.124 kW.

Figure 7.8 shows the direct comparison of experimental (a) and simulated output spectra (b) with increasing distance of the 3 mm-long heated Peltier element from the fiber start. In experiments and simulations the bandwidth of the short-wavelength DW is decreases for more distant heating positions and the width of the spectral gap between the soliton and the long-wavelength DW increases for fiber positions 5 to 8 ($3.5 - 4.4$ cm from the fiber input), which results in a good match of experiments and simulations.

The output spectra for heating position 10 still varies from the room temperature case, even if the change in dispersion is induced 3.5 cm after the initial fission process at around 1.5 μm. This can be explained by the weak dispersion of the TE_{01} mode in this fiber (dispersive length 6.5 cm at 20°C) and the recompression-induced fission after the soliton tunneled through the ND temperature domain. Further simulations with an ideal
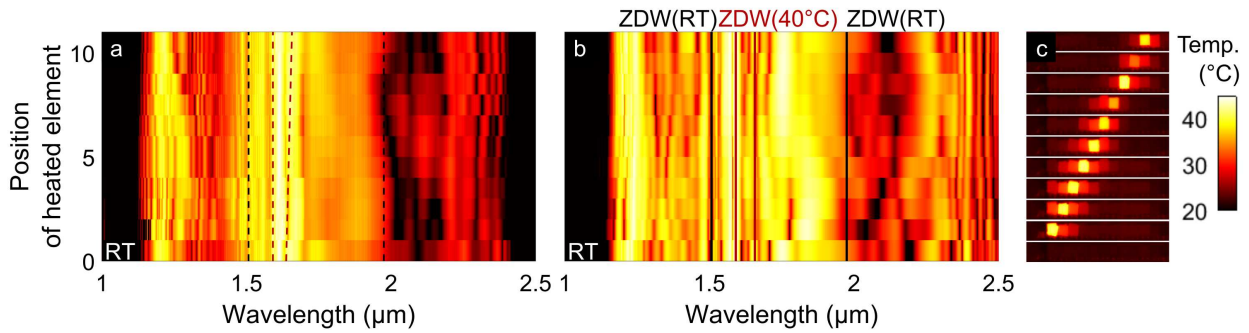
Figure 7.8: **Experimental and numerical output spectra of the TE$_{01}$ mode in a 3.6 μm CS$_2$-core fiber for different heating positions.** 3 mm-long fiber sections are heated to 40°C. The first heated section starts 2 cm from the fiber input. (a) Experimental output spectra were detected with OSA AQ6375. (b) Numerical spectra are obtained using an experimental input spectrum with a peak power of 6.124 kW. The ZDWs for heated/unheated fibers are given as red/black (dashed) lines. All spectra have the same color scale as shown in figure 7.6 (a). (c) Experimentally detected thermal images showing a top view of the individually heated Peltier elements on a room temperature (RT) background of 20°C. The color scale at the right corresponds to all thermal images in (c,f).

.

input pulse showed that even for longer distances of up to 9 cm from the first fission to the end of the heated region recompression and DW triggering is possible for the TE$_{01}$ mode in this fiber.
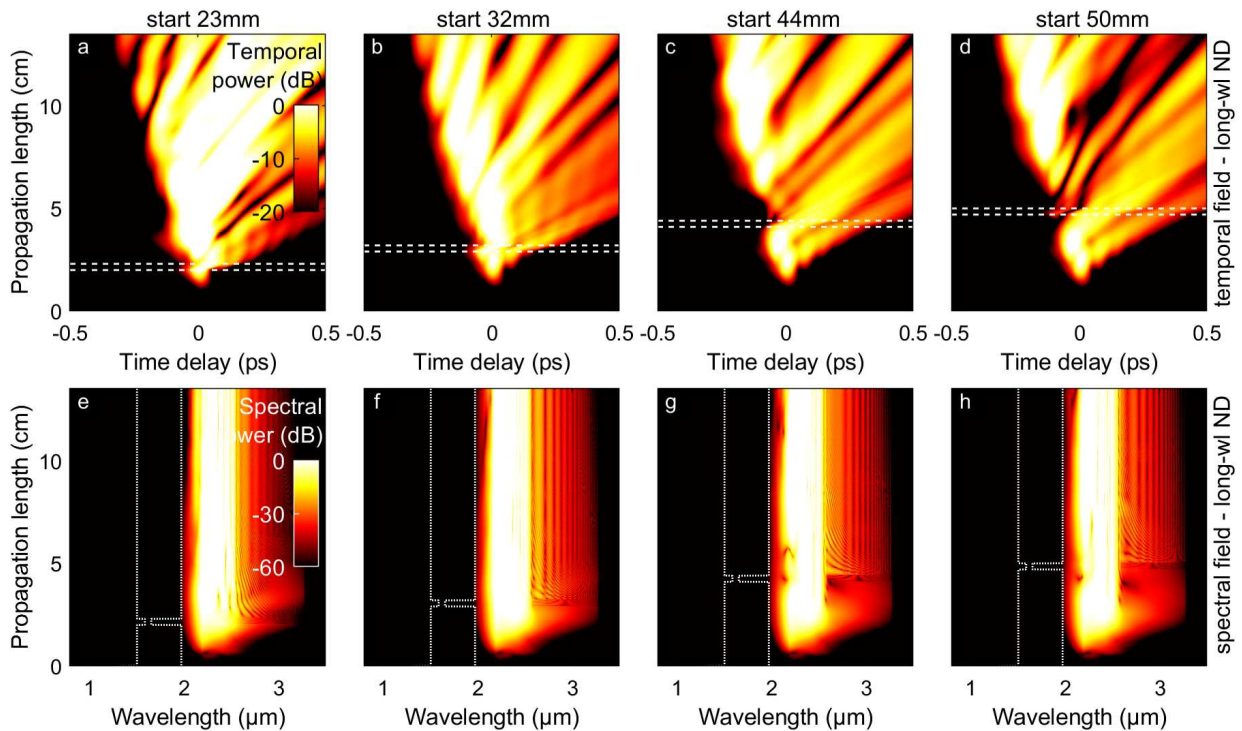
Figure 7.9: **Spectrally filtered simulated temporal and spectral evolutions of the TE$_{01}$ mode in the long-wavelength ND domain of a 3.6 μm CS$_2$-core fiber with different heating positions.** Different starting positions of a 3 mm-long fiber section heated to 40°C starting 23 mm (a,e), 32 mm (b,f), 44 mm (c,g), and 50 mm (d,h) from the front fiber end, corresponding to the positions 1, 4, 8, and 10. The long-wavelength ND regime is isolated similar to figure 7.7 applying a filter for $\lambda > 2200$ nm. All evolution plots are plotted in logarithmic scale, and normalized to their own maximum at 2.3 μm, which is right before the closest heating section starts.

Spectral and temporal evolutions for the heating positions 1, 4, 8, 10 are shown in figure 7.9 starting 2 cm (a,e), 3.2 cm (b,f), 4.4 cm (c,g) and 5.0 cm (d,h) from the fiber start, respectively. In the temporal plots the delayed DW generation after the heated region is very prominent. In the spectral plots this additional DW generation after the domain of modified dispersion induces interference fringes at the long-wavelength edge, whose distancing is almost unaffected by the heating position, but whose onset position is clearly shifted along the fiber. In comparison to the different heating lengths discussed in chapter 7.2.1, the shifted heated position at a fixed heating length induces a local delay between the generated DWs only, but the temporal delay remains almost constant, due to the constant length of the heated fiber section.

To conclude, the length and position of dispersion decreased fiber segments does influence the soliton dynamics and resulting output spectra for dual DW generation in fibers with narrow AD regimes. Even far behind the initial fission point temperature and thus dispersion changes lead to a modification of the output spectra. Recompression of the soliton pulse after traveling through a locally restricted ND region triggers the generation of additional DWs also if this AD regime is reached far behind the initial fission.

In this chapter, experiments with HOMs in temperature-controlled CS_2-core fibers showed that the soliton dynamics can be significantly modified by local dispersion changes. The phase matching wavelength can be shifted by thermally adjusting the dispersion. Furthermore, the position and length of the thermally controlled region influences the dynamics. Soliton breathing, soliton breakdown and soliton tunneling is modified by discrete temperature steps and all experiments were matched with simulations that gave additional insights into the spectral and temporal evolutions of the pulse inside the fiber.

8 Conclusion

This work demonstrates strong modifications of soliton dynamics and supercontinuum generation via external temperature-control. All experimental results are supported by numerical simulations. The used platform consists of higher-order modes that are excited with ultrashort pulses in approximately 10 cm-long step-index CS_2-core fibers. CS_2-core fibers with core diameters around 4.0 μm yield bent group velocity dispersion profiles with two zero-dispersion wavelengths for the TE_{01} and TM_{01} mode, so that the pump pulses centered around 1.57 μm experience flat anomalous group velocity dispersion. The solitons, which are excited in this anomalous dispersion regime, efficiently transfer energy to dispersive waves at the long- and short-wavelength side of the spectrum. Thermally induced modifications of the curved group velocity dispersion give precise control over the soliton dynamics, the wavelengths of the generated dispersive waves and the resulting supercontinuum spectra. Soliton fission, soliton breathing, soliton tunneling, and soliton breakdown in pre-fission and post-fission scenarios are studied numerically and experimentally.

The most dominant temperature-induced effect demonstrated in this thesis, is the strong thermal shift of the long-wavelength dispersive waves. Exciting the TM_{01} mode, the dispersive waves are redshifted by up to 33 nm/K when increasing the temperature of a 4.0μm CS_2-core fiber from 20°C to 45°C. The experimental results showing these strong thermo-spectral shifts are in good agreement with simulations solving the GNLSE, and calculations of the corresponding phase matching conditions. Numerical studies of the nonlinear fiber optics community already suggested strong spectral shifts of dispersive waves in thermally controlled liquid-core optical fibers [122]. Nevertheless, the present experimental results surpass all known publications of experimentally obtained temperature-induced shifts of soliton-based supercontinuum generation in liquid-core fibers [118]. Simulations conducted for the present fiber system lead to the conclusion that the strongly temperature-dependent dispersive waves do not originate from the initial soliton fission at the fiber start. Instead, additional dispersive waves with temperature-dependent wavelengths are generated in the temperature-controlled fiber section, which starts 2 cm after the fiber input due to the shrinking of the anomalous dispersion region. A modified group velocity dispersion regime can force a fundamental soliton to adapt its power, and even break down leading to a strong transfer of energy to phase-matched dispersive waves (post-fission soliton breakdown). For suitable system parameters additional dispersive waves can also be generated by the temporal breathing of solitons, which does not necessarily require a temperature step. At the location in the fiber where the additional dispersive waves are generated, the group velocity dispersion can be modified by the applied temperature. This affects the phase-matching condition with the soliton and leads to temperature-dependent shifts of the short-wavelength and long-wavelength dispersive waves with respect to the room temperature case.

Simulations showed that post-fission tuning in temperature-controlled sections several centimeters behind the fiber input can be more efficient than changing the temperature of the whole fiber. Thus, the initial compression of the soliton in the room temperature section at the fiber has a positive impact of the following thermally controlled soliton dynamics.

For narrow group velocity dispersion regimes efficient energy transfer to wavelengths in the normal dispersion regime takes place via breakdown of higher-order solitons before the fission into fundamental solitons (pre-fission). This is demonstrated in experiments and simulations by exciting the TE_{01} mode in CS_2-core fibers with core diameters of $3.45\,\mu m$ and $3.50\,\mu m$. Narrow anomalous dispersion regimes can be either obtained for small core diameters at room temperatures or for larger core diameters, when the fiber is heated. A temperature-induced blueshift of the long-wavelength zero-dispersion wavelength can lead to a breakdown of the soliton. When the zero dispersion wavelength reaches the soliton wavelength, strong energy transfer to dispersive waves is observed. In some cases no significant power remains at the soliton wavelength, in other cases a weakened soliton survives close to the shifted zero dispersion wavelength in the anomalous dispersion regime. Another experimentally and numerically demonstrated temperature-induced effect is soliton tunneling. By heating a fiber section normal dispersion can be obtained at the soliton wavelength. In case a soliton propagates into this section, it disperses and strictly speaking cannot be called a soliton any more. Simulations showed that the soliton gets recompressed when reentering a fiber section with anomalous group velocity dispersion. Dispersive waves that are triggered by this recompression are detected experimentally. The offset between the initially excited dispersive waves at the fiber start and the tunneling-induced dispersive waves is controlled by the length and position of the heated section.

In summary, different soliton dynamics are experimentally and numerically investigated in CS_2-core fibers. The soliton dynamics and associated dispersive wave generation processes are strongly modified via external temperature-control. While the different effects like soliton fission, soliton breathing, soliton breakdown and soliton tunneling have been already studied individually in therefore specialized waveguides, e.g. customized PCFs, it is a new achievement to obtain, modify and switch between all these effects via temperature, core-diameter and mode adjustment in the same CS_2-core liquid-core fiber system. This work proves that thermally tuned liquid-core fibers are an excellent platform to dynamically modify and fine-tune soliton dynamics due to the outstanding temperature-dependence of the group velocity dispersion of their higher-order modes. Besides adding a new degree of freedom by changing the temperature along the fiber, thermal post-fission tuning of dispersive waves with record wavelength shifts of $33\,nm/K$ was demonstrated experimentally.

9 Outlook

This chapter proposes additional studies building on the present results of temperature-controlled supercontinuum generation in liquid-core fibers, and gives an outlook to promising applications.

Characterization and optimization of temporal power distributions and pulse-to-pulse stability

Following the presented results on soliton-driven supercontinuum generation, the present study can be extended by experimentally analyzing and optimizing the temporal power distribution at the fiber output and the pulse-to-pulse stability of the generated pulses. In this work, the spectral power distribution of soliton-driven supercontinuum generation is analyzed in detail, both experimentally and numerically. However, simulations of the temporal power distributions are only evaluated with regard to better understand the soliton dynamics. But, as temporal distributions define the recompressibility of optical pulses, they are of great importance for applications on their own, and can be determined experimentally, e.g. via XFROG or TG-FROG measurements [292], [293]. Moreover, a high pulse-to-pulse stability of supercontinuum spectra is crucial for many applications in telecommunication and ultrafast spectroscopy [66]. The nonlinear effects causing the spectral broadening also strongly affect the pulse-to-pulse stability. For example, rapid soliton breakdown in fiber systems with two very close zero-dispersion wavelengths is known to produce pulses with high pulse-to-pulse stability [128], [278]. For its characterization, the mutual degree of pulse-to-pulse coherence can be calculated from a large set of noise-seeded simulation results [294], [295]. Experimentally, the optical power fluctuations of a pulsed light source can be for example characterized by measuring the relative intensity noise [296]. On one hand, knowledge of the pulse-to-pulse stability and the temporal distribution of soliton-based supercontinua are important parameters for applications, like optical coherence tomography [64], [165]–[170]. On the other hand, modifications of the temporal width and noise of the input pulses can lead to optimized spectral and temporal power distributions, as well as to improved pulse-to-pulse stability. Soliton fission based supercontinuum generation is known to be highly susceptible to noise of the input pulse [297], which reduces the pulse-to-pulse stability. Injecting input pulses with pulse durations longer 150 fs to CS_2-core fibers, non-instantaneous effects extend the spectral broadening and significantly increase the pulse-to-pulse stability [225]. Cutting the fiber at a length of maximal temporal compression or tuning the input parameters and temperature profile so that maximal temporal compression is obtained at the fiber output, supercontinuum spectra with ultrashort pulse duration shorter 5 fs can be obtained, as demonstrated in similar fiber systems [123], [282], [293], [298]–[300]. Those few cycle pulses are highly interesting to monitor ultrafast chemical processes and conduct experiments in strong-field physics [301].

Advanced longitudinal modifications of the temperature profile

The conducted experiments can be further extended by exploiting the full potential of the introduced setup to locally control the temperature along the liquid-core fibers. Due to the opto-fluidic mounts that are used here to seal the LCF, the temperature is not adjustable in the first 2 cm of the fiber, and in many cases post-fission tuning is observed. To study pre-fission tuning either the fission point needs to be shifted to longer fiber lengths (e.g. via reducing the input power), or the sealing of the fiber needs to be adapted so that the fiber start remains accessible. In the following, alternative sealing methods are discussed. Existing opto-fluidic cells [79], [233], [238], [288], [302] can be reduced in length. Preliminary tests with alternative opto-fluidic cells showed that sealing via pressure using elastic sealing rings is more efficient than using glues or tapes, which often dissolve in CS_2. Another option is to splice LCFs with solid-core delivery fibers [118], [303] or short core-less fiber rods [304]. Here, the main challenge is to avoid air inclusions at the splicing point. Therefore, a small open edge can be left at the splicing point, which is connected to a liquid reservoir [232], [303]. In all-spliced systems air inclusions can be avoided by contracting the liquid before the splicing, and expanding it afterwards [305]. As liquid-contraction based splicing requires fiber lengths of at least 30 cm, absorption losses are stronger than in the 10 cm-long LCFs used in this work [211]. Spliced LCFs further profit from the integrability into all-fiber systems. If the fiber temperature can be controlled from the very beginning, pre-fission tuning can be compared to post-fission tuning at constant input power in the same fiber. Furthermore, the whole fiber can be temperature-controlled homogeneously, which reduces the complexity of the studied system.

Flexible temperature gradients, gratings and random temperature pattern can be realized along the fiber by applying different voltages to each of the small Peltier elements. One possible temperature pattern achievable with the present setup is a grating with alternating high and low temperatures leading to a GVD with periodically changing dispersion. In such a system quasi-phase matching can be obtained, as it was demonstrated using waveguides with periodically changing core sizes [145], [148] or alternated coating [291]. Quasi-phase matching leads to cascaded dispersive wave generation which is favorable to close spectral gaps between soliton and dispersive waves or obtain several tunable wavelength peaks at the long- and short-wavelength side [145]. It is necessary to check if a periodicity of 3 mm is sufficient for quasi-phase-matching in CS_2-core fibers or if a finer temperature grating is required. Moreover, dispersion decreasing fibers [34], [135]–[143] can be realized via temperature control, which are known to yield optimized bandwidth of supercontinua.

With the present setup diverse temperature profiles can be realized and quickly modified to explore nonlinear dynamics in highly complex dispersion profiles. In a first proof of principle experiment different random temperature profiles with 3 mm resolution (according to the length of the Peltier elements) are applied to a 3.6 µm CS_2-core

fiber. Figure 9.1 shows the generated supercontinua for two exemplary temperature landscapes in comparison to an output spectrum at room temperature. The TE_{01} mode is excited with the same pulse parameters as in section 7.2. The temperatures of the
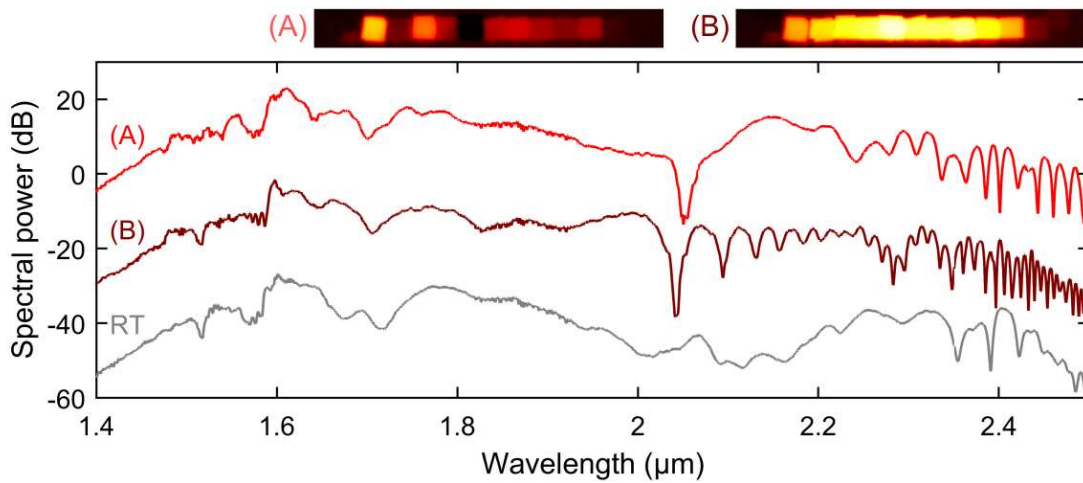
Figure 9.1: **Output spectra of the TE_{01} mode in a 3.6 μm CS_2-core fiber for two random temperature profiles.** Long-wavelength side of the supercontinuum spectra at room temperature (RT) in gray, compared to two exemplary temperature pattern (A), and (B) in red, as shown in the thermal images on top. An offset of 25 dB is added to the spectra for better visibility.

fiber sections vary between 18°C and 58°C. The spectra between 1.9 μm and 2.3 μm vary significantly for the three different temperature cases. This demonstrates the flexibility of the system and opens the door for further investigations with various temperature pattern.

The possibility to flexibly adjust the temperature of individual Peltier elements attached along the liquid-core fiber sets the basis for adapting the temperature profile in an iterative way to reach a tailored output spectrum. By implementing an optimization algorithm the temperature profile can be varied in several iteration steps so that the output spectrum continuously approaches the targeted spectrum. Alternatively, deep learning methods can be used to yield customized spectral or temporal outputs by applying an optimized temperature distribution along the fiber. In the past few years, machine learning concepts and neural networks have been investigated to tailor supercontinuum generation via optimizing the parameters of the used input pulses [306]–[309] and by designing specialized hollow core-fibers [310]. The temperature-tunability represents a new degree of freedom for these optimization methods, and has already been used to shape supercontinua in chirped fiber Bragg gratings [311].

Applications of temperature-tunable supercontinuum generation in liquid-core fibers

Applications of thermally controlled supercontinuum generation in liquid-core fibers are manifold [211]. The flexible control of the group velocity dispersion can be used for fundamental research of nonlinear dynamics, e.g. to further determine the nature of hybrid

soliton dynamics [225]. New coherent operation regimes, like noise robust supercontinuum generation, are expected from the solitons in non-instantaneous nonlinear liquids. In addition, flexible pulse compressors can be realized with tunable liquid-core fibers [299], and their adaptable spectra can be optimized with respect to bandwidth, and defined wavelengths. Photon pair generation with reduced noise (in comparison to solid-core fibers) can be in principle obtained via four wave mixing outside the Raman-bands of the core-liquids [229], [312]. Furthermore, temperature-tunable SCG in liquid-core fibers can possibly be used as neural network itself. Deep neural networks are limited by their huge energy consumption, when intense training cycles are conducted. Optical neural networks are expected to have a reduced energy consumption compared to conventional electrical processors [313]. The research group of Dr. Mario Chemnitz investigates how SCG in optical fibers can substitutes hidden layers between input and output of an optical neural network [314]. The thermal tuning along the fiber length could serve as additional input decoding platform. The thermal control of dispersive wave generation can also be applied for efficient carrier envelope stabilization [171], [315], [316] to form a self-referenced light sources [317]. For example, the long-wavelength dispersive wave can be spectrally shifted via thermal fine-tuning so that the short-wavelength dispersive wave is exactly located at its doubled frequency, which maximizes the beating signal for f–2f interferometry [318]. The same concept can be used to obtain efficient difference-frequency generation of a femtosecond pulse with net-zero carrier-envelope offset phase [317], [319], which has the potential to increase the precision of frequency metrology and optical clocks.

Bibliography

[1] J. Gowlett, "The discovery of fire by humans: A long and convoluted process", *Philosophical Transactions of the Royal Society B: Biological Sciences*, **371**, (0164), 1–12, 2016.

[2] J. Hecht, "Short history of laser development", *SPIE Reviews*, **1**, (1), 1–23, 2010.

[3] M. Jiang, H. Wu, Y. An, *et al.*, "Fiber laser development enabled by machine learning: review and prospect", *PhotoniX*, **3**, (16), 1–27, 2022.

[4] H. Cao, R. Chriki, S. Bittner, A. A. Friesem, and N. Davidson, "Complex lasers with controllable coherence", *Nature Reviews Physics*, **1**, (2), 156–168, 2019.

[5] F. O. Olsen, K. S. Hansen, and J. S. Nielsen, "Multibeam fiber laser cutting", *Journal of Laser Applications*, **21**, (3), 133–138, 2009.

[6] L. Zhu, P. Xue, Q. Lan, *et al.*, "Recent research and development status of laser cladding: A review", *Optics and Laser Technology*, **138**, 106915, 2021.

[7] A. P. Mackwood and R. C. Crafer, "Thermal modelling of laser welding and related processes: A literature review", *Optics and Laser Technology*, **37**, (2), 99–115, 2005.

[8] I. Bernardeschi, M. Ilyas, and L. Beccai, "A Review on Active 3D Microstructures via Direct Laser Lithography", *Advanced Intelligent Systems*, **3**, (9), 2100051, 2021.

[9] Z. Du, S. Zhang, J. Li, N. Gao, and K. Tong, "Mid-infrared tunable laser-based broadband fingerprint absorption spectroscopy for trace gas sensing: A review", *Applied Sciences*, **9**, (338), 1–33, 2019.

[10] S. Peñarrocha-Oltra, R. Soto-Peñaloza, A. Alonso-Arroyo, A. Vidal-Infer, and J. Pascual-Segarra, "Laser-based refractive surgery techniques to treat myopia in adults. An overview of systematic reviews and meta-analyses", *Acta Ophthalmologica*, **100**, (8), 878–893, 2022.

[11] T. H. Maiman, "Stimulated Optical Radiation in Ruby", *Nature*, **187**, (4736), 493–494, 1960.

[12] A. Javan, W. R. Bennett, and D. R. Herriott, "Population inversion and continuous optical maser oscillation in a gas discharge containing a He-Ne mixture", *Physical Review Letters*, **6**, (3), 106–110, 1961.

[13] Y. Lu, C. Yang, H. Wang, L. Ma, M. Xu, and L. Xi, "Structure, principle, and application of magnetic field-assisted pulsed laser deposition: An overview", *Vacuum*, **211**, (111912), 1–11, 2023.

[14] M. D. Radmilović, I. T. Drvenica, M. D. Rabasović, *et al.*, "Interactions of ultrashort laser pulses with hemoglobin: Photophysical aspects and potential applications", *International Journal of Biological Macromolecules*, **244**, (125312), 1–12, 2023.

[15] Z. Luo, D. Wang, K. Li, *et al.*, "Three-Dimensional Nanolithography with Visible Continuous Wave Laser through Triplet Up-Conversion", *Journal of Physical Chemistry Letters*, **14**, (3), 709–715, 2023.

[16] Y. Zhen, Z. Ma, L. Gao, *et al.*, "Ablation behavior and microwave absorption performance of metamaterials irradiated by high-energy continuous-wave laser", *Materials and Design*, **225**, 111502, 2023.

[17] J.-u. Shin, W. Cho, K. Yeom, and K. T. Kim, "Tailoring octave-spanning ultrashort laser pulses using multiple prisms", *Optics Express*, **31**, (14), 22855–22862, 2023.

[18] B. Han, S. Dong, Y. Liu, and Z. Wang, "Cascaded Random Raman Fiber Laser With Low RIN and Wide Wavelength Tunability", *Photonic Sensors*, **12**, (4), 220414, 2022.

[19] M. Xiang, Y. Zhang, G. Li, *et al.*, "Wide-waveguide high-power low-RIN single-mode distributed feedback laser diodes for optical communication", *Optics Express*, **30**, (17), 30187–30197, 2022.

[20] D. Mahgerefteh, Y. Matsui, X. Zheng, and K. McCallion, "Chirp managed laser and applications", *IEEE Journal on Selected Topics in Quantum Electronics*, **16**, (5), 1126–1139, 2010.

[21] S. Petrakis, M. Bakarezos, M. Tatarakis, E. P. Benis, and N. A. Papadogiannis, "Electron quantum path control in high harmonic generation via chirp variation of strong laser pulses", *Scientific Reports*, **11**, (23882), 1–9, 2021.

[22] R. W. Boyd, *Nonlinear Optics*. Academic Press, Elsevier, 2008.

[23] P. D. Maker, R. W. Terhune, and C. M. Savage, "Intensity-dependent changes in the refractive index of liquids", *Physical Review Letters*, **12**, (18), 507–509, 1964.

[24] K. Sala and M. C. Richardson, "Optical Kerr effect induced by ultrashort laser pulses", *Physcal Review A*, **5**, (3), 1036–1047, 1975.

[25] E. P. Ippen, C. V. Shank, and T. K. Gustafson, "Self-phase modulation of picosecond pulses in optical fibers", *Applied Physics Letters*, **24**, (4), 190–192, 1974.

[26] M. N. Islam, J. R. Simpson, H. T. Shang, L. F. Mollenauer, and R. H. Stolen, "Cross-phase modulation in optical fibers", *Optics Letters*, **12**, (8), 625–627, 1987.

[27] O. Aso, M. Tadakuma, and S. Namiki, "Four-wave mixing in optical fibers and its applications", *Furukawa Review*, (19), 63–68, 2000.

[28] G. Agrawal, *Nonlinear Fiber Optics*. Academic Press, Elsevier, 2013.

[29] R. R. Alfano, *The Supercontinuum Laser Source: The Ultimate White Light*. Springer, 2006.

[30] J. M. Dudley, G. Genty, and S. Coen, "Supercontinuum generation in photonic crystal fiber", *Reviews of Modern Physics*, **78**, 1135–1184, 2006.

[31] A. Hasegawa and F. Tappert, "Transmission of stationary nonlinear optical pulses in dispersive dielectric fibers. II. Normal dispersion", *Applied Physics Letters*, **23**, (4), 171–172, 1973.

[32] L. F. Mollenauer, R. H. Stolen, and J. P. Gordon, "Experimental observation of picosecond pulse narrowing and solitons in optical fibers", *Physical Review Letters*, **45**, (13), 1095–1098, 1980.

[33] D. Mogilevtsev, T. A. Birks, and P. S. J. Russell, "Group-velocity dispersion in photonic crystal fibers", *Optics Letters*, **23**, (21), 1662–1664, 1998.

[34] K. Mori, H. Takara, S. Kawanishi, M. Saruwatari, and T. Morioka, "Flatly broadened supercontinuum spectrum generated in a dispersion decreasing fibre with convex dispersion profile", *Electronic Letters*, **33**, (21), 1806–1808, 1997.

[35] T. Okuno, M. Onishi, and M. Nishimura, "Generation of ultra-broad-band supercontinuum by dispersion-flattened and decreasing fiber", *IEEE Photonics Technology Letters*, **10**, (1), 72–74, 1998.

[36] T. A. Birks, W. J. Wadsworth, and P. S. J. Russell, "Supercontinuum generation in a short tapered fibre", *Optics Letters*, **25**, (19), 1415–1417, 2000.

[37] J. M. Harbold, F. Ö. Ilday, F. W. Wise, T. A. Birks, W. J. Wadsworth, and Z. Chen, "Long-wavelength continuum generation about the second dispersion zero of a tapered fiber", *Optics InfoBase Conference Papers*, **27**, (17), 1558–1560, 2002.

[38] L. Tartara, I. Cristiani, and V. Degiorgio, "Blue light and infrared continuum generation by soliton fission in a microstructured fiber", *Applied Physics B: Lasers and Optics*, **77**, 307–311, 2003.

[39] G. Genty, M. Lehtonen, H. Ludvigsen, and M. Kaivola, "Enhanced bandwidth of supercontinuum generated in microstructured fibers", *Optics Express*, **12**, (15), 3471–3480, 2004.

[40] S. G. Leon-Saval, T. A. Birks, W. J. Wadsworth, P. S. Russell, and M. W. Mason, "Supercontinuum generation in submicron fibre waveguides", *Optics Express*, **12**, (13), 2864–2869, 2004.

[41] K. M. Hilligsøe, T. V. Andersen, H. N. Paulsen, *et al.*, "Supercontinuum generation in a photonic crystal fiber with two zero dispersion wavelengths", *Optics Express*, **12**, (6), 1045–1054, 2004.

[42] T. Schreiber, T. V. Andersen, D. Schimpf, J. Limpert, and A. Tünnermann, "Supercontinuum generation by femtosecond single and dual wavelength pumping in photonic crystal fibers with two zero dispersion wavelengths", *Optics Express*, **13**, (23), 9556–9569, 2005.

[43] J. Y. Leong, P. Petropoulos, J. H. Price, *et al.*, "High-nonlinearity dispersion-shifted lead-silicate holey fibers for efficient 1-μm pumped supercontinuum generation", *Journal of Lightwave Technology*, **24**, (1), 183–190, 2006.

[44] B. A. Cumberland, J. C. Travers, S. V. Popov, and J. R. Taylor, "High power 29 W CW supercontinuum source", *Optics Express*, **16**, (8), 1353–1355, 2008.

[45] P. Falk, M. H. Frosz, O. Bang, *et al.*, "Broadband light generation at 1300 nm through spectrally recoiled solitons and dispersive waves", *Optics Letters*, **33**, (6), 621–623, 2008.

[46] S. Martin-Lopez, L. Abrardi, P. Corredera, M. Gonzalez Herraez, and A. Mussot, "Spectrally-bounded continuous-wave supercontinuum generation in a fiber with two zero-dispersion wavelengths", *Optics Express*, **16**, (9), 6745–6755, 2008.

[47] A. Boucon, D. Alasia, J. C. Beugnot, *et al.*, "Supercontinuum Generation From 1.35 to 1.7μm by Nanosecond Pumping Near the Second Zero-Dispersion Wavelength of a Microstructured Fiber", *IEEE Photonics Technology Letters*, **20**, (10), 842–844, 2008.

[48] A. Boucon, T. Sylvestre, K. P. Huy, *et al.*, "Supercontinuum generation by nanosecond dual-pumping near the two zero-dispersion wavelengths of a photonic crystal fiber", *Optics Communications*, **284**, (1), 467–470, 2011.

[49] N. Granzow, M. A. Schmidt, W. Chang, *et al.*, "Mid-infrared supercontinuum generation in As2S3-silica "nano-spike" step-index waveguide", *Optics Express*, **21**, (9), 10969–10977, 2013.

[50] J. H. Yuan, X. Z. Sang, Q. Wu, *et al.*, "Widely tunable broadband deep-ultraviolet to visible wavelength generation by the cross phase modulation in a hollow-core photonic crystal fiber cladding", *Laser Physics Letters*, **10**, (8), 085402, 2013.

[51] R. K. W. Lau, M. R. E. Lamont, A. G. Griffith, Y. Okawachi, M. Lipson, and A. L. Gaeta, "Octave-spanning mid-infrared supercontinuum generation in silicon nanowaveguides", *Optics Letters*, **39**, (15), 4518–4521, 2014.

[52] C. R. Petersen, U. Møller, I. Kubat, *et al.*, "Mid-infrared supercontinuum covering the 1.4-13.3 μm molecular fingerprint region using ultra-high NA chalcogenide step-index fibre", *Nature Photonics*, **8**, (11), 830–834, 2014.

[53] X. Jiang, N. Y. Joly, M. A. Finger, *et al.*, "Deep-ultraviolet to mid-infrared supercontinuum generated in solid-core ZBLAN photonic crystal fibre", *Nature Photonics*, **9**, (2), 133–139, 2015.

[54] S. Kedenburg, T. Steinle, F. Mörz, *et al.*, "Solitonic supercontinuum of femtosecond mid-IR pulses in W-type index tellurite fibers with two zero dispersion wavelengths", *APL Photonics*, **1**, (8), 086101, 2016.

[55] M. A. G. Porcel, F. Schepers, J. P. Epping, *et al.*, "Two-octave spanning supercontinuum generation in stoichiometric silicon nitride waveguides pumped at telecom wavelengths", *Optics Express*, **25**, (2), 1596–1603, 2017.

[56] F. Köttig, D. Novoa, F. Tani, *et al.*, "Mid-infrared dispersive wave generation in gas- filled photonic crystal fibre by transient ionization- driven changes in dispersion", *Nature Communications*, **8**, (813), 1–8, 2017.

[57] Z. X. Jia, C. F. Yao, S. J. Jia, *et al.*, "Supercontinuum generation covering the entire 0.4-5 μm transmission window in a tapered ultra-high numerical aperture all-solid fluorotellurite fiber", *Laser Physics Letters*, **15**, (2), 025102, 2018.

[58] D. Korobko, V. Kamynim, M. Salganski, *et al.*, "(Invited) Control of supercontinuum generation due to soliton propagation in fibers with varying dispersion", *Optik*, **287**, 171032, 2023.

[59] R. Borrego-Varillas, A. Nenov, L. Ganzer, *et al.*, "Two-dimensional UV spectroscopy: A new insight into the structure and dynamics of biomolecules", *Chemical Science*, **10**, (43), 9907–9921, 2019.

[60] A. Kudlinski, M. Lelek, B. Barviau, L. Audry, and A. Mussot, "Efficient blue conversion from a 1064 nm microchip laser in long photonic crystal fiber tapers for fluorescence microscopy", *Optics Express*, **18**, (16), 16640–16645, 2010.

[61] S. Hashimoto, K. Hamada, I. Iwakura, *et al.*, "Photochemical reaction mechanisms of 4,5-dimethoxy-2-nitrobenzyl acetate analysed by a sub-10 fs near-ultraviolet pulse laser", *Chemical Physics*, **524**, 70–76, 2019.

[62] S. Lambert-Girard, M. Allard, M. Piché, and F. Babin, "Differential optical absorption spectroscopy lidar for mid-infrared gaseous measurements", *Applied Optics*, **54**, (7), 1647–1656, 2015.

[63] S. Dupont, C. Petersen, J. Thøgersen, C. Agger, O. Bang, and S. R. Keiding, "IR microscopy utilizing intense supercontinuum light source", *Optics Express*, **20**, (5), 4887–4892, 2012.

[64] N. M. Israelsen, C. R. Petersen, A. Barh, *et al.*, "Real-time high-resolution mid-infrared optical coherence tomography", *Light: Science & Applications*, **8**, (11), 1–13, 2019.

[65] T. Ohara, H. Takara, and T. Yamamoto, "Over-1000-Channel Ultradense WDM Transmission With Supercontinuum Multicarrier Source", *Journal of Lightwave Technology*, **24**, (6), 2311–2317, 2006.

[66] A. Rampur, D. M. Spangenberg, B. Sierro, P. Hänzi, M. Klimczak, and A. M. Heidt, "Perspective on the next generation of ultra-low noise fiber supercontinuum sources and their emerging applications in spectroscopy, imaging, and ultrafast photonics", *Applied Physics Letters*, **118**, (24), 2021.

[67] Norm, *ISO 20473:2007 Optics and photonics - Spectral bands*, 2021. [Online]. Available: https://www.iso.org/standard/39482.html (visited on 07/06/2021).

[68] R. Paschotta, *RP Photonics Encyclopedia Infrared Light*, 2023. [Online]. Available: https://www.rp-photonics.com/infrared%7B%5C_%7Dlight.html (visited on 03/05/2023).

[69] O. Mouawad, F. Amrani, C. Strutynski, *et al.*, "Multioctave midinfrared supercontinuum generation in suspended-core chalcogenide fibers", **39**, (9), 2684–2687, 2014.

[70] T. Cheng, K. Nagasaka, T. H. Tuan, *et al.*, "Mid-infrared supercontinuum generation spanning 2.0 to 15.1 μm in a chalcogenide step-index fiber", *Optics Letters*, **41**, (9), 2117–2120, 2016.

[71] L. Zhang, T. H. Tuan, L. Liu, *et al.*, "Widely tunable dispersive wave generation and soliton self-frequency shift in a tellurite microstructured optical fiber pumped near the zero dispersion wavelength", *Journal of Optics*, **17**, (12), 125501, 2015.

[72] G. Qin, X. Yan, C. Kito, *et al.*, "Ultrabroadband supercontinuum generation from ultraviolet to 6.28 μm in a fluoride fiber", *Applied Physics Letters*, **95**, (16), 1–4, 2009.

[73] J. Swiderski and M. Michalska, "Over three-octave spanning supercontinuum generated in a fluoride fiber pumped by Er & Er:Yb-doped and Tm-doped fiber amplifiers", *Optics and Laser Technology*, **52**, 75–80, 2013.

[74] R. Salem, Z. Jiang, D. Liu, *et al.*, "Mid-infrared supercontinuum generation spanning 18 octaves using step-index indium fluoride fiber pumped by a femtosecond fiber laser near 2 μm", *Optics Express*, **23**, (24), 30592–30602, 2015.

[75] Y. Tang, L. G. Wright, K. Charan, T. Wang, C. Xu, and F. W. Wise, "Generation of intense 100 fs solitons tunable from 2 to 4.3 μm in fluoride fiber", *Optica*, **3**, (9), 948–951, 2016.

[76] Z. Eslami, P. Ryczkowski, C. Amiot, L. Salmela, and G. Genty, "High-power short-wavelength infrared supercontinuum generation in multimode fluoride fiber", *Journal of the Optical Society of America B*, **36**, (2), 72–78, 2019.

[77] L. Yang, Y. Li, B. Zhang, T. Wu, Y. Zhao, and J. Hou, "30-W supercontinuum generation based on ZBLAN fiber in an all-fiber configuration", *Photonics Research*, **7**, (9), 1061–1065, 2019.

[78] I. D. Rukhlenko, M. Premaratne, and G. P. Agrawal, "Effective mode area and its optimization in silicon-nanocrystal waveguides", *Optics Letters*, **37**, (12), 2295–2297, 2012.

[79] M. Chemnitz, R. Scheibinger, C. Gaida, *et al.*, "Thermodynamic control of soliton dynamics in liquid-core fibers", *Optica*, **5**, (6), 695–703, 2018.

[80] A. Mussot, M. Conforti, S. Trillo, F. Copie, and A. Kudlinski, "Modulation instability in dispersion oscillating fibers", *Advances in Optics and Photonics*, **10**, (1), 1–42, 2018.

[81] R. Scheibinger, N. M. Lüpken, M. Chemnitz, *et al.*, "Higher-order mode supercontinuum generation in dispersion-engineered liquid-core fibers", *Scientific Reports*, **11**, (5270), 1–11, 2021.

[82] Y. Sun, C. F. Booker, S. Kumari, R. N. Day, M. Davidson, and A. Periasamy, "Characterization of an orange acceptor fluorescent protein for sensitized spectral fluorescence resonance energy transfer microscopy using a white-light laser", *Journal of Biomedical Optics*, **14**, (5), 054009, 2009.

[83] R. Vidano, D. B. Fishbach, L. J. Willis, and T. M. Loehr, "Observation of Raman band shifting with excitation wavelength for carbons and graphites", *Solid State Communications*, **39**, (2), 341–344, 1981.

[84] A. B. Fedotov, A. N. Naumov, A. M. Zheltikov, *et al.*, "Frequency-tunable supercontinuum generation in photonic-crystal fibers by femtosecond pulses of an optical parametric amplifier", *Journal of the Optical Society of America B*, **19**, (9), 2156–2164, 2002.

[85] S. Murugkar, C. Brideau, A. Ridsdale, M. Naji, P. K. Stys, and H. Anis, "Coherent anti-Stokes Raman scattering microscopy using photonic crystal fiber with two closely lying zero dispersion wavelengths", *Optics Express*, **15**, (21), 14028–14037, 2007.

[86] S. C. Warren-Smith, K. Schaarschmidt, M. Chemnitz, *et al.*, "Tunable multi-wavelength third-harmonic generation using exposed-core microstructured optical fiber", *Optics Letters*, **44**, (3), 626–629, 2019.

[87] S. Duval, J.-C. Gauthier, L.-R. Robichaud, *et al.*, "Watt-level fiber-based femtosecond laser source tunable from 2.8 to 3.6 μm", *Optics Letters*, **41**, (22), 5294–5297, 2016.

[88] A. Fuerbach, P. Steinvurzel, J. A. Bolger, A. Nulsen, and B. J. Eggleton, "Nonlinear propagation effects in antiresonant high-index inclusion photonic crystal fibers", *Optics Letters*, **30**, (8), 830–832, 2005.

[89] G. K. L. Wong, S. G. Murdoch, R. Leonhardt, J. D. Harvey, and V. Marie, "Fiber Optical Parametric Oscillator Ω Ω", *Optics Express*, **15**, (6), 2947–2952, 2007.

[90] S. M. Kobtsev, S. V. Kukarin, and S. V. Smirnov, "Fiber supercontinuum generator with wavelength-tunable pumping", *Laser Physics*, **18**, (11), 1257–1259, 2008.

[91] S. Kedenburg, T. Steinle, F. Mörz, A. Steinmann, and H. Giessen, "High-power mid-infrared high repetition-rate supercontinuum source based on a chalcogenide step-index fiber", *Optics Letters*, **40**, (11), 2668–2671, 2015.

[92] S. Pricking, M. Vieweg, and H. Giessen, "Influence of the retarded response on an ultrafast nonlinear optofluidic fiber coupler", *Optics Express*, **19**, (22), 21673–21679, 2011.

[93]   A. Apolonski, B. Povazay, A. Unterhuber, *et al.*, "Spectral shaping of supercontinuum in a cobweb photonic-crystal fiber with sub-20-fs pulses", *Journal of the Optical Society of America B*, **19**, (9), 2165–2170, 2002.

[94]   M. Lehtonen, G. Genty, H. Ludvigsen, and M. Kaivola, "Supercontinuum generation in a highly birefringent microstructured fiber", *Applied Physics Letters*, **82**, (14), 2197–2199, 2003.

[95]   V. L. Kalashnikov, P. Dombi, T. Fuji, *et al.*, "Maximization of supercontinua in photonic crystal fibers by using double pulses and polarization effects", *Applied Physics B: Lasers and Optics*, **77**, (2-3), 319–324, 2003.

[96]   D. Stoliarov, A. Koviarov, D. Korobko, D. Galiakhmetova, and E. Rafailov, "Fibre laser system with wavelength tuning in extended telecom range", *Optical Fiber Technology*, **72**, (102994), 1–6, 2022.

[97]   G. Genty, M. Lehtonen, H. Ludvigsen, J. Broeng, and M. Kaivola, "Spectral broadening of femtosecond pulses into continuum radiation in microstructured fibers", *Optics Express*, **10**, (20), 1083–1098, 2002.

[98]   F. G. Omenetto, N. A. Wolchover, M. R. Wehner, *et al.*, "Spectrally smooth supercontinuum from 350 nm to 3 μm in sub-centimeter lengths of soft-glass photonic crystal fibers", *Optics Express*, **14**, (11), 4928, 2006.

[99]   D. R. Carlson, D. D. Hickstein, A. Lind, *et al.*, "Photonic-Chip Supercontinuum with Tailored Spectra for Counting Optical Frequencies", *Physical Review Applied*, **8**, (1), 1–10, 2017.

[100] G. Moille, D. Westly, N. G. Orji, and K. Srinivasan, "Tailoring broadband Kerr soliton microcombs via post-fabrication tuning of the geometric dispersion", *Applied Physics Letters*, **119**, (12), 2021.

[101] A. Mussot, M. Beaugeoix, M. Bouazaouv, and T. Sylvestre, "Tailoring strong cw supercontinuum generation in microstructured fibers with two-zero dispersion wavelengths", *Optics InfoBase Conference Papers*, **15**, (18), 11553–11563, 2007.

[102] T. A. K. Lühder, K. Schaarschmidt, S. Goerke, E. P. Schartner, H. Ebendorff-Heidepriem, and M. A. Schmidt, "Resonance-Induced Dispersion Tuning for Tailoring Nonsolitonic Radiation via Nanofilms in Exposed Core Fibers", *Laser & Photonics Review*, **14**, (1900418), 1–9, 2020.

[103] K. Schaarschmidt, H. Xuan, J. Kobelke, M. Chemnitz, I. Hartl, and M. A. Schmidt, "Long-term stable supercontinuum generation and watt-level transmission in liquid-core optical fibers", *Optics Letters*, **44**, (9), 2236, 2019.

[104] S. Junaid, K. Schaarschmidt, M. Chemnitz, M. Chambonneau, S. Nolte, and M. A. Schmidt, "Tailoring modulation instabilities and four wave mixing in dispersion-managed composite liquid-core fibers", *Optics Express*, **28**, (3), 3097–3106, 2020.

[105] M. Chemnitz, N. Walther, R. Scheibinger, *et al.*, "Tailoring soliton fission at telecom wavelengths using composite-liquid-core fibers", *Optics Letters*, **45**, (11), 2985–2988, 2020.

[106] J. C. Travers, W. Chang, J. Nold, N. Y. Joly, and P. S. J. Russell, "Ultrafast nonlinear optics in gas-filled hollow-core photonic crystal fibers [Invited]", *J. Opt. Soc. Am. B*, **28**, (12), A11–A26, 2011.

[107] P. S. J. Russell, P. Hölzer, W. Chang, A. Abdolvand, and J. C. Travers, "Hollow-core photonic crystal fibres for gas-based nonlinear optics", *Nature Photonics*, **8**, 278–286, 2014.

[108] A. I. Adamu, M. S. Habib, C. R. Petersen, *et al.*, "Deep-UV to Mid-IR Supercontinuum Generation driven by Mid-IR Ultrashort Pulses in a Gas-filled Hollow-core Fiber", *Scientific Reports*, **9**, (4446), 1–9, 2019.

[109] J. Hammer, M. V. Chekhova, D. R. Häupl, R. Pennetta, and N. Y. Joly, "Broadly tunable photon-pair generation in a suspended-core fiber", *Physical Review Research*, **2**, (1), 1–5, 2020.

[110] S. Pumpe, M. Chemnitz, J. Kobelke, and M. A. Schmidt, "Monolithic optofluidic mode coupler for broadband thermo-and piezo-optical characterization of liquids", *Optics Express*, **25**, (19), 22932–22946, 2017.

[111] T. Handa, H. Tahara, T. Aharen, and Y. Kanemitsu, "Large negative thermo-optic coefficients of a lead halide perovskite", *Science Advances*, **5**, (7), 1–9, 2019.

[112] C. Wang, "Effect of Temperature on Supercontinuum Generation in CS 2 -Core Optical Fiber", *IEEE Photonics Journal*, **10**, (5), 1–11, 2018.

[113] X. Chen, X. Yan, X. Zhang, *et al.*, "Microstructured optical fiber temperature sensor based on the self-phase modulation effect", *Optics Express*, **29**, (10), 15653–15663, 2021.

[114] T. Cheng, X. Chen, X. Yan, *et al.*, "Microstructured optical fiber filled with glycerin for temperature measurement based on dispersive wave and soliton", *Optics Express*, **29**, (26), 42355–42368, 2021.

[115] A. Kudlinski, A. Mussot, R. Habert, and T. Sylvestre, "Widely tunable parametric amplification and pulse train generation by heating a photonic crystal fiber", *IEEE Journal of Quantum Electronics*, **47**, (12), 1514–1518, 2011.

[116] J. Abreu-Afonso, A. Díez, J. L. Cruz, and M. V. Andrés, "Effects of temperature and axial strain on four-wave mixing parametric frequencies in microstructured optical fibers pumped in the normal dispersion regime", *Photonics*, **1**, (4), 404–411, 2014.

[117] A. Loredo-Trejo, A. Díez, E. Silvestre, and M. V. Andrés, "Broadband tuning of polarization modulation instability in microstructured optical fiber through thermal heating", *Advanced Photonics Congress, Optics*, **NpM2D.4**, 2020.

[118]   L. Velazquez-Ibarra, A. Diez, E. Silvestre, and M. V. Andres, "Tuning four-wave mixing through temperature in ethanol-filled photonic crystal fiber", *International Conference on Transparent Optical Networks*, 16–17, 2016.

[119]   S. Martin-Lopez, M. Gonzalez-Herraez, P. Corredera, M. L. Hernanz, A. Carrasco, and J. A. Mendez, "Temperature effects on supercontinuum generation using a continuous-wave Raman fiber laser", *Optics Communications*, **267**, (1), 193–196, 2006.

[120]   G. J. Raj, R. V. J. Raja, P. Grelu, R. Ganapathy, and K. Porsezian, "Effect of Temperature on Supercontinuum Generation in Water-Core Photonic Crystal Fiber", *IEEE Photonics Technology Letters*, **28**, (11), 1209–1212, 2016.

[121]   S. Singh, V. Mishra, and S. Varshney, "Mid-IR multipeak and stepwise blueshifted dispersive wave generation in liquid-filled chalcogenide capillary optical fibers", *Journal of the Optical Society of America B*, **33**, (11), D65–D71, 2016.

[122]   N. Nallusamy, R. V. J. Raja, and G. J. Raj, "Highly Sensitive Nonlinear Temperature Sensor Based on Modulational Instability Technique in Liquid Infiltrated Photonic Crystal Fiber", *IEEE Sensor Journal*, **17**, (12), 3720–3727, 2017.

[123]   S. Bohman, A. Suda, T. Kanai, S. Yamaguchi, and K. Midorikawa, "Generation of 5-fs, 5-mJ pulse using hollow-fiber pulse compression at 1 kHz", *Optics Letters*, **35**, (11), 1887–1889, 2010.

[124]   S. Fang, K. Yamane, J. Zhu, C. Zhou, Z. Zhang, and M. Yamashita, "Generation of sub-900-μJ supercontinuum with a two-octave bandwidth based on induced phase modulation in argon-filled hollow fiber", *IEEE Photonics Technology Letters*, **23**, (11), 688–690, 2011.

[125]   K. F. Mak, J. C. Travers, P. Hölzer, N. Y. Joly, and P. S. J. Russell, "Tunable vacuum-UV to visible ultrafast pulse source based on gas-filled Kagome-PCF", *Optics Express*, **21**, (9), 10942–10953, 2013.

[126]   S. F. Gao, Y. Y. Wang, F. Belli, C. Brahms, P. Wang, and J. C. Travers, "From Raman Frequency Combs to Supercontinuum Generation in Nitrogen-Filled Hollow-Core Anti-Resonant Fiber", *Laser and Photonics Reviews*, **16**, (4), 2022.

[127]   R. Sollapur, D. Kartashov, M. Zürch, *et al.*, "Resonance-enhanced multi-octave supercontinuum generation in antiresonant hollow-core fibers", *Light: Science & Applications*, **6**, (12), 1–7, 2017.

[128]   G. Genty, S. Coen, and J. M. Dudley, "Fiber supercontinuum sources (Invited)", *Journal of the Optical Society of America B*, **24**, (8), 1771–1785, 2007.

[129]   U. Møller, S. T. Sørensen, C. Larsen, *et al.*, "Optimum PCF tapers for blue-enhanced supercontinuum sources", *Optical Fiber Technology*, **18**, (5), 304–314, 2012.

[130] J. Wei, C. Ciret, M. Billet, F. Leo, B. Kuyken, and S.-P. Gorza, "Supercontinuum generation assisted by dispersive waves trapping in dispersion-managed integrated silicon waveguides", *Physical Review Applied*, **14**, (5), 054045, 2020.

[131] F. Lu and W. H. Knox, "Generation of a broadband continuum with high spectral coherence in tapered single-mode optical fibers", *OSA Trends in Optics and Photonics Series*, **97**, (2), 1137–1139, 2004.

[132] J. C. Travers, A. B. Rulkov, S. V. Popov, *et al.*, "Multi-watt supercontinuum generation from 0.3 to 2.4 μm in PCF tapers", *Quantum Electronics and Laser Science Conference*, 7–8, 2007.

[133] H. H. Chen, Z. L. Chen, X. F. Zhou, and J. Hou, "Ultraviolet-extended flat supercontinuum generation in cascaded photonic crystal fiber tapers", *Laser Physics Letters*, **10**, (085401), 1–7, 2013.

[134] T. S. Saini, T. H. Tuan, T. Suzuki, and Y. Ohishi, "Coherent Mid-IR Supercontinuum Generation using Tapered Chalcogenide Step-Index Optical Fiber: Experiment and modelling", *Scientific Reports*, **10**, (1), 1–9, 2020.

[135] J. Lou, T. Xia, B. 0., C.-X. Shi, G. Nowak, and M. Islam, "Broader and flatter supercontinuum spectra in dispersion-tailored fibers", *OFC '97 Technical Digest*, (Di), 32–34, 2021.

[136] A. Kudlinski, A. K. George, J. C. Knight, *et al.*, "Zero-dispersion wavelength decreasing photonic crystal fibers for ultraviolet-extended supercontinuum generation", *Optics Express*, **14**, (12), 5715–5722, 2006.

[137] L. Abrardi, S. Martín-López, A. Carrasco-Sanz, P. Corredera, M. L. Hernanz, and M. González-Herráez, "Optimized all-fiber supercontinuum source at 1.3 μm generated in a stepwise dispersion-decreasing-fiber arrangement", *Journal of Lightwave Technology*, **25**, (8), 2098–2102, 2007.

[138] S. P. Stark, A. Podlipensky, and P. S. J. Russell, "Soliton blueshift in tapered photonic crystal fibers", *Physical Review Letters*, **106**, (8), 1–4, 2011.

[139] A. Bendahmane, A. Mussot, M. Conforti, and A. Kudlinski, "Observation of the stepwise blue shift of a dispersive wave preceding its trapping by a soliton", *Optics Express*, **23**, (13), 16595, 2015.

[140] D. A. Korobko, O. G. Okhotnikov, D. A. Stoliarov, A. A. Sysolyatin, and I. O. Zolotovskii, "Broadband infrared continuum generation in dispersion shifted tapered fiber", *Journal of the Optical Society of America B*, **32**, (4), 692, 2015.

[141] M. Eftekhar, Z. Sanjabi-Eznaveh, H. Lopez-Aviles, *et al.*, "Accelerated nonlinear interactions in graded-index multimode fibers", *Nature Communications*, **10**, 1–10, 2019.

[142] X. Qi, R. Scheibinger, J. Nold, S. Junaid, M. Chemnitz, and M. A. Schmidt, "Axial dispersion-managed liquid-core fibers: A platform for tailored higher-order mode supercontinuum generation", *APL Photonics*, **7**, (116106), 1–9, 2022.

[143] I. V. Zhluktova, V. A. Kamynin, D. A. Korobko, *et al.*, "Broadband Supercontinuum Generation in Dispersion Decreasing Fibers in the Spectral Range 900–2400 nm", *Photonics*, **9**, (773), 1–12, 2022.

[144] A. A. Sysoliatin, A. K. Senatorov, A. I. Konyukhov, L. A. Melnikov, and V. A. Stasyuk, "Soliton fission management by dispersion oscillating fiber", *Optics Express*, **15**, (25), 16302–16307, 2007.

[145] A. Bendahmane, F. Braud, M. Conforti, B. Barviau, A. Mussot, and A. Kudlinski, "Dynamics of cascaded resonant radiations in a dispersion-varying optical fiber", *Optica*, **1**, (4), 243–249, 2014.

[146] M. Billet, F. Braud, A. Bendahmane, M. Conforti, A. Mussot, and A. Kudlinski, "Emission of multiple dispersive waves from a single Raman-shifting soliton in an axially-varying optical fiber", *Optics Express*, **22**, (21), 25673–25678, 2014.

[147] T. A. K. Lühder, H. Schneidewind, E. P. Schartner, H. Ebendorff-Heidepriem, and M. A. Schmidt, "Longitudinally thickness-controlled nanofilms on exposed core fibres enabling spectrally flattened supercontinuum generation", *Light: Advanced Manufacturing*, **2**, (21), 1–12, 2021.

[148] D. D. Hickstein, G. C. Kerber, D. R. Carlson, *et al.*, "Quasi-Phase-Matched Supercontinuum Generation in Photonic Waveguides", *Physical Review Letters*, **120**, (053903), 1–6, 2018.

[149] H. Zia, N. M. Lüpken, T. Hellwig, C. Fallnich, and K.-J. Boller, "Supercontinuum generation in media with sign-alternated dispersion", *Laser & Photonics Review*, **14**, (7), 2000031, 2019.

[150] V. A. Bogatyrjov, M. M. Bubnov, S. L. Semenov, and A. A. Sysoliatin, "Length-varying computer-controlled fibre drawing", *Measurement Science and Technology*, **5**, (11), 1370–1374, 1994.

[151] D. Colladon, "On the reflections of a ray of light inside a parabolic liquid stream", *Comptes Rendus*, **15**, 800–802, 1842.

[152] W. K. Johnston, "The birth of fiberoptics from "light guiding".", *Journal of endourology*, **18**, (5), 425–426, 2004.

[153] T. Miya, Y. Terunuma, T. Hosaka, and T. Miyashita, "Ultimate low-loss single-mode fibre at 1.55µm", *Electronics Letters*, **15**, (4), 106–108, 1979.

[154] B. Debord, F. Amrani, L. Vincetti, F. Gérôme, and F. Benabid, "Hollow-core fiber technology: The rising of "gas photonics"", *Fibers*, **7**, (16), 1–58, 2019.

[155] K. M. Kiang, K. Frampton, T. M. Monro, *et al.*, "Extruded single-mode non-siloca glass holey optical fibers", *Electronics Letter*, **38**, (12), 546–547, 2002.

[156] J. K. Ranka, R. S. Windeler, and A. J. Stentz, "Efficient visible continuum generation in air-silica microstructure optical fibers with anomalous dispersion at 800 nm", *Optics Letters*, **25**, (1), 25–27, 2000.

[157] A. D. Pryamikov, A. S. Biriukov, A. F. Kosolapov, V. G. Plotnichenko, S. L. Semjonov, and E. M. Dianov, "Demonstration of a waveguide regime for a silica hollow - core microstructured optical fiber with a negative curvature of the core boundary in the spectral region > 35 μm", *Optics Express*, **19**, (2), 1441–1448, 2011.

[158] R. Cregan, B. J. Mangan, T. Birks, *et al.*, "Single-Mode Photonic Band Gap Guidance of Light in Air.", *Science*, **285**, (5433), 1537–1539, 1999.

[159] T. A. Birks, J. C. Knight, and P. S. J. Russell, "Endlessly single-mode photonic crystal fiber", *Optics Letters*, **22**, (13), 961–963, 1997.

[160] A. W. Snyder and J. D. Love, *Optical Waveguide Theory*. Chapman and Hall, 1983.

[161] R. R. Alfano and S. L. Shapiro, "Observation of self-phase modulation and small-scale filaments in crystals and glasses", *Physical Review Letters*, **24**, (11), 592–594, 1970.

[162] B. C. Van, T. T. Hai, N. T. Thao, Q. H. Dinh, D. T. Nguyen, and H. Van Le, "Experimental study of supercontinuum generation in water-filled-cladding photonic crystal fiber in visible and near-infrared region", *Optical and Quantum Electronics*, **55**, (229), 1–14, 2023.

[163] H. Kano and H.-o. Hamaguchi, "Characterization of a supercontinuum generated from a photonic crystal fiber and its application to coherent Raman spectroscopy", *Optics Letters*, **28**, (23), 2360–2362, 2003.

[164] I. Zorin, P. Gattinger, A. Ebner, and M. Brandstetter, "Advances in mid-infrared spectroscopy enabled by supercontinuum laser sources", *Optics Express*, **30**, (4), 5222–5254, 2022.

[165] I. Hartl, X. D. Li, C. Chudoba, *et al.*, "Ultrahigh-resolution optical coherence tomography using continuum generation in an air–silica microstructure optical fiber", *Optics Letters*, **26**, (9), 608–610, 2001.

[166] N. Nishizawa, Y. Chen, P. Hsiung, E. P. Ippen, and J. G. Fujimoto, "Real-time, ultrahigh-resolution, optical coherence tomography with an all-fiber, femtosecond fiber laser continuum at 15 μm", *Optics Letters*, **29**, (24), 2846–2848, 2004.

[167] G. Humbert, W. Wadsworth, S. Leon-Saval, *et al.*, "Supercontinuum generation system for optical coherence tomography based on tapered photonic crystal fibre", *Optics Express*, **14**, (4), 1596–1603, 2006.

[168] S. Moon and Y. D. Kim, "Ultra-high-speed phase-sensitive optical coherence reflectometer with a stretched pulse supercontinuum source", *Applied Optics*, **50**, (21), 4000–4004, 2011.

[169] M.-T. Tsai and M.-C. Chan, "Source for Optical Coherence Tomography", *Optics Letters*, **39**, (4), 865–868, 2014.

[170] S. Rao D. S, M. Jensen, L. Grüner-Nielsen, *et al.*, "Shot-noise limited, supercontinuum-based optical coherence tomography", *Light: Science and Applications*, **10**, (133), 1–13, 2021.

[171] H. R. Telle, G. Steinmeyer, A. E. Dunlop, J. Stenger, D. H. Sutter, and U. Keller, "Carrier-envelope offset phase control: A novel concept for absolute optical frequency measurement and ultrashort pulse generation", *Applied Physics B: Lasers and Optics*, **69**, (4), 327–332, 1999.

[172] T. Udem, R. Holzwarth, and T. W. Hänsch, "Optical frequency metrology", *Nature*, **416**, (6877), 233–237, 2002.

[173] J. T. Woodward, A. W. Smith, C. A. Jenkins, C. Lin, S. W. Brown, and K. R. Lykke, "Supercontinuum sources for metrology", *Metrologia*, **46**, S277–S282, 2009.

[174] S. V. Smirnov, J. D. Ania-Castanon, T. J. Ellingham, S. M. Kobtsev, S. Kukarin, and S. K. Turitsyn, "Optical spectral broadening and supercontinuum generation in telecom applications", *Optical Fiber Technology*, **12**, (2), 122–147, 2006.

[175] M.-C. Chan, C.-H. Lien, J.-Y. Lu, and B.-H. Lyu, "High power NIR fiber-optic femtosecond Cherenkov radiation and its application on nonlinear light microscopy", *Optics Express*, **22**, (8), 9498–9507, 2014.

[176] Q. Cui, Z. Chen, Q. Liu, Z. Zhang, Q. Luo, and L. Fu, "Visible continuum pulses based on enhanced dispersive wave generation for endogenous fluorescence imaging", *Biomedical Optics Express*, **8**, (9), 4026–4036, 2017.

[177] J. Dudley and R. Taylor, *Supercontinuum Generation in Optical Fibers*. Cambridge University Press, 2010.

[178] L. Walmsley, L. Waxer, and C. Dorrer, "The role of dispersion in ultrafast optics", *Review of Scientific Instruments*, **72**, (1 I), 1–29, 2001.

[179] E. F. Chillcce, C. M. B. Cordeiro, R. S. Ramos, *et al.*, "Development of soft-glasses photonic crystal fiber made by stacking-and-draw technique", *Optical Components and Materials IV*, **6469**, 64690U, 2007.

[180] J. W. Fleming, "Dispersion in GeO2 -SiO2 glasses", *Applied Optics*, **23**, (24), 4486–4493, 1984.

[181] T. A. Birks and Y. W. Li, "The Shape of Fiber Tapers", *Journal of Lightwave Technology*, **10**, (4), 432–438, 1992.

[182] A. L. Gaeta, "Nonlinear propagation and continuum generation in microstructured optical fibers", *Optics Letters*, **27**, (11), 924–926, 2002.

[183] B. Kibler, P. A. Lacourt, F. Courvoisier, and J. M. Dudley, "Soliton spectral tunnelling in photonic crystal fibre with sub-wavelength core defect", *Electronics letters*, **41**, (2), 40–41, 2007.

[184] T. Sylvestre, E. Genier, A. N. Ghosh, *et al.*, "Recent advances in supercontinuum generation in specialty optical fibers", *Journal of the Optical Society of America B*, **38**, (12), F90–F103, 2021.

[185] M. Chemnitz, "Soliton Dynamics in Liquid-Core Optical Fibers", Ph.D. dissertation, FSU Jena, 2019.

[186] K. Tai, A. Tomita, J. L. Jewell, and A. Hasegawa, "Generation of subpicosecond solitonlike optical pulses at 0.3 THz repetition rate by induced modulational instability", *Applied Physics Letters*, **49**, (5), 236–238, 1986.

[187] E. Greer, D. Patrick, P. Wigley, and J. Taylor, "Generation of 2 THz repetition rate pulse trains through induced modulational instability", *Electronics Letters*, **25**, (18), 1246–1248, 1989.

[188] P. K. A. Wai, H. H. Chen, and Y. C. Lee, "Radiation by solitons at the zero group dispersion wavelength of single-mode optical fibers", *Physical Review A*, **41**, (1), 426–439, 1900.

[189] N. Akhmediev and M. Karlsson, "Cherenkov radiation emitted by solitons in optical fibers", *Physical Review A*, **51**, (3), 2602–2607, 1995.

[190] J. Herrmann, U. Griebner, N. Zhavoronkov, *et al.*, "Experimental Evidence for Supercontinuum Generation by Fission of Higher-Order Solitons in Photonic Fibers", *Physical Review Letters*, **88**, (17), 173901, 2002.

[191] T. X. Tran and F. Biancalana, "Dynamics and control of the early stage of supercontinuum generation in submicron-core optical fibers", *Physical Review A - Atomic, Molecular, and Optical Physics*, **79**, (6), 4–7, 2009.

[192] A. V. Husakou and J. Herrmann, "Supercontinuum Generation of Higher-Order Solitons by Fission in Photonic Crystal Fibers", *Physical Review Letters*, **87**, (20), 1–4, 2001.

[193] F. Biancalana, D. V. Skryabin, and A. V. Yulin, "Theory of the soliton self-frequency shift compensation by the resonant radiation in photonic crystal fibers", *Physical Review E*, **70**, (016615), 1–9, 2004.

[194] D. V. Skryabin, F. Luan, and J. C. Knight, "Soliton Self-Frequency Shift Cancellation in Photonic Crystal Fibers", *Science*, **301**, 1705–1709, 2003.

[195] F. M. Mitschke and L. F. Mollenauer, "Discovery of the soliton self-frequency shift", *Optics Letters*, **11**, (10), 659–661, 1986.

[196] J. P. Gordon, "Theory of the soliton self-frequency shift", *Optics Letters*, **11**, (10), 662–664, 1986.

[197] J. H. Lee, J. van Howe, C. Xu, and X. Liu, "Soliton Self-Frequency Shift: Experimental Demonstrations and Applications", *IEEE Journal of Selected Topics in Quantum Electronics*, **14**, (3), 713–723, 2008.

[198] T. Cheng, Y. Kanou, K. Asano, *et al.*, "Soliton self-frequency shift and dispersive wave in a hybrid four-hole AsSe2-As2S5 microstructured optical fiber", *Applied Physics Letters*, **104**, (121911), 1–4, 2014.

[199] S. Liu, W. Wu, Z. He, *et al.*, "Dispersive waves generation in photonic crystal fibers: The role on supercontinuum generation and rogue waves manipulation", *Infrared Physics and Technology*, **128**, (104520), 1–10, 2023.

[200] P. Falk, M. H. Frosz, and O. Bang, "Supercontinuum generation in a photonic crystal fiber with two zero-dispersion wavelengths tapered to normal dispersion at all wavelengths", *Optics Express*, **13**, (19), 7535–7540, 2005.

[201] M. H. Frosz, P. Falk, and O. Bang, "The role of the second zero-dispersion wavelength in generation of supercontinua and bright-bright soliton-pairs across the zero-dispersion wavelength", *Optics Express*, **13**, (16), 6181–6192, 2005.

[202] T. Lühder, "Nano-film functionalized exposed core fibers enabling resonance-driven dispersive wave tailoring", Ph.D. dissertation, FSU Jena, 2022.

[203] A. Efimov, A. J. Taylor, F. G. Omenetto, *et al.*, "Time-spectrally-resolved ultrafast nonlinear dynamics in small-core photonic crystal fibers: Experiment and modelling", *Optics Express*, **12**, (26), 6498–6507, 2004.

[204] P. V. Mamyshev, P. G. Wigley, J. Wilson, *et al.*, "Adiabatic compression of Schrödinger solitons due to the combined perturbations of higher-order dispersion and delayed nonlinear response", *Physical Review Letters*, **71**, (1), 73–76, 1993.

[205] R. Scheibinger, J. Hofmann, K. Schaarschmidt, M. Chemnitz, and M. A. Schmidt, "Temperature-Sensitive Dual Dispersive Wave Generation of Higher-Order Modes in Liquid-Core Fibers", *Laser and Photonics Reviews*, **2100598**, 1–11, 2022.

[206] N. Vermeulen, D. Espinosa, A. Ball, *et al.*, "Post-2000 nonlinear optical materials and measurements: Data tables and best practices", *Journal of Physics: Photonics*, **5**, (035001), 2023.

[207] SIGMA-ALDRICH, "Carbon disulfide data sheet", 1–9, 2019.

[208] NIOSH, *Carbon disulfide - The National Institute for Occupational Safety and Health (NIOSH)*, 2023. [Online]. Available: https://www.cdc.gov/niosh/idlh/75150.html (visited on 09/04/2023).

[209] M. Davidson and M. Feinleib, "Carbon disulfide poisoning: A review", *American Heart Journal*, **83**, (1), 100–114, 1972.

[210] B. Elvers and F. Ullmann, *Ullmann's Encyclopedia of Industrial Chemistry*. Weinheim VCH, 1985.

[211] M. Chemnitz, S. Junaid, and M. A. Schmidt, "Liquid-Core Optical Fibers – A Dynamic Platform for Nonlinear Photonics", *Laser and Photonics Reviews*, **2300126**, 1–28, 2023.

[212] D. B. Leviton, K. H. Miller, M. A. Quijada, and F. D. Grupp, "Temperature-dependent refractive index measurements of CaF2, Suprasil 3001, and S-FTM16 for the Euclid Near Infrared Spectrometer and Photometer", *Proc. SPIE, Current Developments in Lens Design and Optical Engineering XVI*, **9578**, 95780M, 2015.

[213] R. Kasztelanic, J. Cimek, I. Kujawa, *et al.*, "Mid-infrared ZBLAN glass optical components made by hot embossing technique", *Optics and Laser Technology*, **157**, (108655), 1–6, 2023.

[214] F. M. Sladen, D. N. Payne, and M. J. Adams, "Determination of optical fiber refractive index profiles by a near-field scanning technique", *Applied Physics Letters*, **28**, (5), 255–258, 1976.

[215] M. Richert, H. Honghua, M. R. Ferdinandus, *et al.*, "Temporal , spectral , and polarization dependence of the nonlinear optical response of carbon disulfide", *Optica*, **1**, (6), 436–445, 2014.

[216] K. Moutzouris, M. Papamichael, S. C. Betsis, I. Stavrakas, G. Hloupis, and D. Triantis, "Refractive , dispersive and thermo-optic properties of twelve organic solvents in the visible and near-infrared", *Applied Physics B*, **116**, 617–622, 2014.

[217] D. Milam, "Review and assessment of measured values of the nonlinear refractive-index coefficient of fused silica", *Applied Optics*, **37**, (3), 546–550, 1998.

[218] D. Milam, M. J. Weber, and A. J. Glass, "Nonlinear refractive index of fluoride crystals", *Applied Physics Letters*, **31**, 822–825, 1977.

[219] S. Junaid, W. Huang, R. Scheibinger, *et al.*, "Attenuation coefficients of selected organic and inorganic solvents in the mid-infrared spectral domain", *Optical Materials Express*, **12**, (4), 1754–1763, 2022.

[220] H. J. Meyer, M. Sharonov, and R. R. Alfano, "Ultra-high intensity temporally oscillatory optical Kerr effect in Carbon Disulfide arising from electronic and molecular distortions", *Optics Communications*, **524**, (128806), 1–6, 2022.

[221] A. J. Campillo and S. L. Shapiro, "H.4 Relationship of Self-Focusing to Spatial Instability Modes", *IEEE Journal of Quantum Electronics*, **24**, (4), 178–180, 1974.

[222] W. E. Williams, M. J. Soileau, and E. W. Van Stryland, "Optical switching and n2 measurements in CS2", *Optics Communications*, **50**, (4), 256–260, 1984.

[223] D. Mcmorrow, W. T. Lotshaw, and G. A. Kenney-Wallace, "Femtosecond Optical Kerr Studies on the Origin of the Nonlinear Responses in Simple Liquids", *IEEE Journal of Quantum Electronics*, **24**, (2), 443–454, 1988.

[224] M. Reichert, H. Hu, M. R. Ferdinandus, *et al.*, "Temporal , spectral , and polarization dependence of the nonlinear optical response of carbon disulfide : erratum", *Optica*, **3**, (6), 657–658, 2016.

[225] M. Chemnitz, M. Gebhardt, C. Gaida, *et al.*, "Hybrid soliton dynamics in liquid-core fibres", *Nature Communications*, **8**, (42), 1–11, 2017.

[226] R. H. Stolen, J. P. Gordon, and W. J. Tomlinson, "Raman response function of silica-core fibers", *Journal of the Optical Society of America B*, **6**, (6), 1159–1166, 1989.

[227] O. D. Herrera, L. Schneebeli, K. Kieu, R. A. Norwood, and N. Peyghambarian, "Raman-induced frequency shift in CS2-filled integrated liquid-core optical fiber", *Optics Communications*, **318**, 83–87, 2014.

[228] D. Wang, K. Mittauer, and N. Reynolds, "Raman scattering of carbon disulfide: The temperature effect", *American Journal of Physics*, **77**, (12), 1130–1134, 2009.

[229] M. Barbier, I. Zaquine, and P. Delaye, "Spontaneous four-wave mixing in liquid-core fibers: Towards fibered Raman-free correlated photon sources", *New Journal of Physics*, **17**, (053031), 1–11, 2015.

[230] S. Vergara Palacio and R. Acuna Herrera, "Dispersive wave and four-wave mixing generation in noninstantaneous nonlinear fiber solitons", *Applied Optics*, **58**, (10), 2736–2744, 2019.

[231] G. S. He, M. Casstevens, R. Burzynski, and X. Li, "Broadband, multiwavelength stimulated-emission source based on stimulated Kerr and Raman scattering in a liquid-core fiber system", *Applied Optics*, **34**, (3), 444–454, 1995.

[232] K. Kieu, L. Schneebeli, R. A. Norwood, and N. Peyghambarian, "Integrated liquid-core optical fibers for ultra- efficient nonlinear liquid photonics", *Optics Express*, **20**, (7), 8148–8154, 2012.

[233] G. Fanjoux, S. Margueron, J.-c. Beugnot, and T. Sylvestre, "Supercontinuum generation by stimulated Raman-Kerr scattering in a liquid-core optical fiber", *J. Opt. Soc. Am. B*, **34**, (8), 1677–1683, 2017.

[234] R. O. Behunin, Y. H. Ou, and K. Kieu, "Spontaneous forward Brillouin scattering in carbon disulfide", *Physical Review A*, **99**, (63826), 1–6, 2019.

[235] D. Churin, T. N. Nguyen, K. Kieu, R. A. Norwood, and N. Peyghambarian, "Mid-IR supercontinuum generation in an integrated liquid-core optical fiber filled with CS2", *Optical Materials Express*, **3**, (9), 1358–1364, 2013.

[236] S. Kedenburg, T. Gissibl, T. Steinle, A. Steinmann, and H. Giessen, "Towards integration of a liquid-filled fiber capillary for supercontinuum generation in the 1.2–2.4 μm range", *Optics Express*, **23**, (7), 8281–8289, 2015.

[237] C. Karaguleff, G. I. Stegeman, R. Fortenberry, R. Zanoni, and C. T. Seaton, "Degenerate four-wave mixing in planar CS2 covered waveguides", *Applied Physics Letters*, **46**, (7), 621–623, 1985.

[238] Y. Chen, L. Wang, and M. Qiu, "Stimulated Raman scattering and four-wave mixing in hollow optical fiber filled with mixture of carbon tetrachloride and phenylethanol", *Zhongguo Jiguang/Chinese Journal of Lasers*, **20**, (4), 296–300, 1991.

[239] W. Sellmeier, "Ueber die durch die Aetherschwingungen erregten Mitschwingungen der Körpertheilchen und deren Rückwirkung auf die ersteren, besonders zur Erklärung der Dispersion und ihrer Anomalien", *Annalen der Physik*, **221**, (4), 520–549, 1872.

[240] K. Schaarschmidt, J. Kobelke, T. Meyer, M. Chemnitz, and M. A. Schmidt, "Third-harmonic generation with tailored modes in liquid core fibers with geometric birefringence", *Optics Letters*, **45**, (24), 6859–6862, 2020.

[241] E. W. Washburn, "The dynamics of capillary flow", *The Physical Review*, **18**, (3), 273–283, 1921.

[242] K. Bartle, B. Wright, and M. Lee, "Characterization of glass, quartz, and fused silica capillary column surfaces from contact-angle measurements", *Chromatographia*, **14**, (7), 387–397, 1981.

[243] M. W. Ogden and H. M. McNair, "Characterization of fused-silica capillary tubing by contact angle measurements", *Journal of Chromatography*, **354**, (C), 7–18, 1986.

[244] M. Beresna, M. Gecevičius, P. G. Kazansky, and T. Gertus, "Radially polarized optical vortex converter created by femtosecond laser nanostructuring of glass", *Applied Physics Letters*, **98**, (20), 2–4, 2011.

[245] B. Schaefer, E. Collett, R. Smyth, D. Barrett, and B. Fraher, "Measuring the Stokes polarization parameters", *American Journal of Physics*, **75**, (2), 163–168, 2007.

[246] R. Scheibinger, *Supercontinuum Generation and Temperature Tunability of Higher-Order Modes in Liquid-Core Fibers - Master thesis FSU Jena*, 2018.

[247] Y. Wan, X. Qi, J. Hofmann, *et al.*, "Optical heating-induced spectral tuning of supercontinuum generation in liquid core fibers using multiwall carbon nanotubes", *Optics Express*, **31**, (19), 30911–30920, 2023.

[248] J. Hult, "A fourth-order Runge-Kutta in the Interaction Picture Method for", *Journal of Lightwave Technology*, **25**, (12), 3770–3775, 2007.

[249] F. Poletti and P. Horak, "Description of ultrashort pulse propagation in multi-mode optical fibers", *Journal of the Optical Society of America B*, **25**, (10), 1645–1654, 2008.

[250] N. M. Lüpken, M. Timmerkamp, R. Scheibinger, *et al.*, "Numerical and Experimental Demonstration of Intermodal Dispersive Wave Generation", *Laser and Photonics Reviews*, **15**, (9), 1–8, 2021.

[251] L. Xu, E. Zeek, and R. Trebino, "Simulations of Frequency-Resolved Optical Gating for measuring very complex pulses", *Springer Series in Chemical Physics*, **25**, (6), A70–A80, 2008.

[252] M. Klimczak, G. Soboń, R. Kasztelanic, K. M. Abramski, and R. Buczyński, "Direct comparison of shot-to-shot noise performance of all normal dispersion and anomalous dispersion supercontinuum pumped with sub-picosecond pulse fiber-based laser", *Scientific Reports*, **6**, (19284), 1–14, 2016.

[253] A. M. Heidt, J. S. Feehan, J. H. V. Price, and T. Feurer, "Limits of coherent supercontinuum generation in normal dispersion fibers", *Journal of the Optical Society of America B*, **34**, (4), 764–755, 2017.

[254] V. T. Hoang, R. Kasztelanic, A. Anuszkiewicz, *et al.*, "All-normal dispersion supercontinuum generation in photonic crystal fibers with large hollow cores infiltrated with toluene", *Optical Materials*, **8**, (11), 3568–3582, 2018.

[255] S. Dai, Y. Wang, X. Peng, P. Zhang, X. Wang, and Y. Xu, "A review of mid-infrared supercontinuum generation in chalcogenide glass fibers", *Applied Sciences*, **8**, (707), 1–28, 2018.

[256] F. Poletti and P. Horak, "Dynamics of femtosecond supercontinuum generation in multimode fibers", *Optics Express*, **17**, (8), 6134–6147, 2009.

[257] D. Marcuse, "Interdependence of waveguide and material dispersion", *Applied Optics*, **18**, (17), 2930–2932, 1979.

[258] R. A. Sammut and S. J. Garth, "Multiple-frequency generation on single-mode optical fibers", *Journal of the Optical Society of America B*, **6**, (9), 1732–1735, 1989.

[259] T. V. Andersen, K. M. Hilligsøe, C. K. Nielsen, *et al.*, "Continuous-wave wavelength conversion in a photonic crystal fiber with two zero-dispersion wavelengths: erratum", *Optics Express*, **12**, (17), 4113–4122, 2004.

[260] M. Kolesik, L. Tartara, and J. V. Moloney, "Effective three-wave-mixing picture and first Born approximation for femtosecond supercontinua from microstructured fibers", *Physical Review A - Atomic, Molecular, and Optical Physics*, **82**, (4), 1–4, 2010.

[261] B. Kibler, C. Michel, A. Kudlinski, B. Barviau, G. Millot, and A. Picozzi, "Emergence of spectral incoherent solitons through supercontinuum generation in a photonic crystal fiber", *Physical Review E*, **84**, (066605), 1–9, 2011.

[262] S. Wei, J. Yuan, C. Yu, *et al.*, "Design on a highly birefringent and highly nonlinear tellurite ellipse core photonic crystal fiber with two zero dispersion wavelengths", *Optical Fiber Technology*, **20**, (4), 320–324, 2014.

[263] R. Absar, S. Fatema, M. I. Reja, and J. Akhtar, "Elliptically Infiltrated Core Nonlinear Photonic Crystal Fiber with Two Zero Dispersion Wavelengths and Ultra High Birefringence for Supercontinuum Generation", *International Journal of Photonics and Optical Technology*, **4**, (1), 19–26, 2018.

[264] S. Xie, F. Tani, J. C. Travers, *et al.*, "As2S3-silica double-nanospike waveguide for mid-infrared supercontinuum generation", *Optics Letters*, **39**, (17), 5216–5219, 2014.

[265] M. N. Hossain, M. S. Alam, D. M. N. Hasan, and K. M. Mohsin, "A highly nonlinear spiral photonic crystal fiber for tailoring two zero dispersion wavelengths in the visible region", *Photonics Letters of Poland*, **2**, (3), 143–145, 2010.

[266] S. Zhao, H. Yang, N. Chen, X. Fu, and C. Zhao, "Soliton Trapping of Dispersive Waves in Photonic Crystal Fiber With Three Zero-Dispersive Wavelengths", *IEEE Photonics Journal*, **7**, (5), 1–9, 2015.

[267] Y. Huang, H. Yang, S. Zhao, Y. Mao, and S. Chen, "Design of photonic crystal fibers with flat dispersion and three zero dispersion wavelengths for coherent supercontinuum generation in both normal and anomalous regions", *Results in Physics*, **23**, (104033), 1–10, 2021.

[268] K. Nielsen, D. Noordegraaf, T. Sørensen, A. Bjarklev, and T. P. Hansen, "Selective filling of photonic crystal fibres", *Journal of Optics A: Pure and Applied Optics*, **7**, (8), L13–L20, 2005.

[269] J. Bethge, A. Husakou, F. Mitschke, *et al.*, "Two-octave supercontinuum generation in a water-filled photonic crystal fiber", *Optics Express*, **18**, (6), 6230–6240, 2010.

[270] M. Vieweg, T. Gissibl, Y. V. Kartashov, L. Torner, and H. Giessen, "Spatial solitons in optofluidic waveguide arrays with focusing ultrafast Kerr nonlinearity", *Optics Letters*, **37**, (13), 2454–2456, 2012.

[271] Y. Peng, J. Hou, Y. Zhang, Z. Huang, R. Xiao, and Q. Lu, "Temperature sensing using the bandgap-like effect in a selectively liquid-filled photonic crystal fiber", *Optics Letters*, **38**, (3), 263–265, 2013.

[272] Y. Yu, X. Gai, T. Wang, *et al.*, "Mid-infrared supercontinuum generation in chalcogenides", *Optical Materials Express*, **3**, (8), 1075–1086, 2013.

[273] A. Bozolan, C. J. S. D. Matos, C. M. B. Cordeiro, E. M. Santos, and J. Travers, "Supercontinuum generation in a water-core photonic crystal fiber", *Optics Express*, **16**, (13), 9671–9676, 2008.

[274] V. T. Hoang, R. Kasztelanic, G. Stepniewski, *et al.*, "Femtosecond supercontinuum generation around 1560 nm in hollow-core photonic crystal fibers filled with carbon tetrachloride", *Applied Optics*, **59**, (12), 3720–3725, 2020.

[275] F. Belli, A. Abdolvand, W. Chang, J. Travers, and P. S. J. Russell, "Vacuum-ultraviolet to infrared supercontinuum in hydrogen-filled photonic crystal fiber", *Optica*, **2**, (4), 292–300, 2015.

[276] I. Cristiani, R. Tediosi, L. Tartara, and V. Degiorgio, "Dispersive wave generation by solitons in microstructured optical fibers", *Optics Express*, **12**, (1), 124–135, 2004.

[277] D. V. Skryabin and A. V. Gorbach, "Colloquium: Looking at a soliton through the prism of optical supercontinuum", *Reviews of Modern Physics*, **82**, (2), 1287–1299, 2010.

[278] I. Babushkin, A. Tajalli, H. Sayinc, U. Morgner, G. Steinmeyer, and A. Demircan, "Simple route toward efficient frequency conversion for generation of fully coherent supercontinua in the mid-IR and UV range", *Light: Science and Applications*, **6**, 1–8, 2017.

[279] T. Marest, F. Braud, M. Conforti, A. Mussot, S. Wabnitz, and A. Kudlinski, "Longitudinal soliton tunneling in optical fiber", *Optics Letters*, **42**, (12), 2350–2353, 2017.

[280] C. Ciret, S. P. Gorza, C. Husko, G. Roelkens, B. Kuyken, and F. Leo, "Physical origin of higher-order soliton fission in nanophotonic semiconductor waveguides", *Scientific reports*, **8**, (17177), 1–11, 2018.

[281] D. Yoon Oh, K. Y. Yang, C. Fredrick, G. Ycas, S. A. Diddams, and K. J. Vahala, "Coherent ultra-violet to near-infrared generation in silica ridge waveguides", *Nature Communications*, **8**, 1–7, 2017.

[282] J. C. Travers, B. A. Cumberland, A. B. Rulkov, *et al.*, "Pulse compression in dispersion decreasing photonic crystal fiber", *Optics Express*, **15**, (20), 13203–13211, 2007.

[283] V. Serkin, V. Vysloukh, and J. Taylor, "Soliton spectral tunnelling effect", *Electronics Letters*, **29**, (1), 12–13, 1993.

[284] F. Poletti, P. Horak, and D. J. Richardson, "Soliton spectral tunneling in dispersion-controlled holey fibers", *IEEE Photonics Technology Letters*, **20**, (16), 1414–1416, 2008.

[285] H. Guo, S. Wang, X. Zeng, and M. Bache, "Understanding soliton spectral tunneling as a spectral coupling effect", *IEEE Photonics Technology Letters*, **25**, (19), 1928–1931, 2013.

[286] E. N. Tsoy and C. M. De Sterke, "Theoretical analysis of the self-frequency shift near zero-dispersion points: Soliton spectral tunneling", *Physical Review A*, **76**, (4), 1–9, 2007.

[287] E. Genier, P. Bowen, T. Sylvestre, J. M. Dudley, P. Moselund, and O. Bang, "Amplitude noise and coherence degradation of femtosecond supercontinuum generation in all-normal-dispersion fibers", *Journal of the Optical Society of America B*, **36**, (2), A161–A167, 2019.

[288] V. T. Hoang, R. Kasztelanic, A. Filipkowski, *et al.*, "Supercontinuum generation in an all-normal dispersion large core photonic crystal fiber infiltrated with carbon tetrachloride", *Optical Materials Express*, **9**, (5), 2264–2278, 2019.

[289] M. D. Pelusi and H. F. Liu, "Higher order soliton pulse compression in dispersion-decreasing optical fibers", *IEEE Journal of Quantum Electronics*, **33**, (8), 1430–1438, 1997.

[290] S. Chernikov, E. M. Dianov, D. J. Richardson, and D. N. Payne, "Soliton pulse compression in dispersion-decreasing fiber", *Optics Letters*, **18**, (7), 476–478, 1993.

[291] T. A. Lühder, M. Chemnitz, H. Schneidewind, E. P. Schartner, H. Ebendorff-Heidepriem, and M. A. Schmidt, "Tailored Multi-Color Dispersive Wave Formation in Quasi-Phase-Matched Exposed Core Fibers", *Advanced Science*, **9**, (2103864), 1–9, 2022.

[292] N. Nishizawa and T. Goto, "Experimental Analysis of Ultrashort Pulse Propagation along Optical Fibers Using the Technique of Cross-Correlation Frequency Resolved Optical Gating.", *Optics Express*, **8**, (6), 328–334, 2001.

[293] F. Hagemann, O. Gause, L. Wöste, and T. Siebert, "Supercontinuum pulse shaping in the few-cycle regime", *Optics Express*, **21**, (5), 5536–5549, 2013.

[294] J. M. Dudley and S. Coen, "Numerical simulations and coherence properties of supercontinuum generation in photonic crystal and tapered optical fibers", *IEEE Journal on Selected Topics in Quantum Electronics*, **8**, (3), 651–659, 2002.

[295] A. Antikainen, H. B. Kabagöz, and S. Ramachandran, "Fragility of a soliton's shot-to-shot coherence", *Optics Letters*, **45**, (19), 1–4, 2020.

[296] T. Morioka, S. Kawanishi, K. Mori, and M. Saruwatari, "Nearly penatly-free, 4ps supercontinuum WDM pulse generation for Tbits/s TDM-WDM networks", *Electronics Letters*, **30**, (10), 790–791, 1994.

[297] K. L. Corwin, N. R. Newbury, J. M. Dudley, *et al.*, "Fundamental Noise Limitations to Supercontinuum Generation in Microstructure Fiber", *Physical Review Letters*, **90**, (11), 113904, 2003.

[298] M. Nisoli, S. De Sivestri, S. Stagira, and O. Svelto, "High energy 10 fs pulses by a new pulse compression technique using hollow quartz waveguides", *Springer Series in Chemical Physics*, **62**, 81–82, 1996.

[299] Y. Sato, R. Morita, and M. Yamashita, "Femtosecond optical pulse compressor using CS2 liquid-core fiber with negative delayed nonlinear response", *Japanese Journal of Applied Physics*, **36**, (11), 6768–6774, 1997.

[300] C.-M. Chen and P. L. Kelley, "Nonlinear pulse compression in optical fibers: scaling laws and numerical analysis", *Journal of the Optical Society of America B*, **19**, (9), 1961–1967, 2002.

[301] K. Tian, L. He, X. Yang, and H. Liang, "Mid-infrared few-cycle pulse generation and amplification", *Photonics*, **8**, (290), 1–24, 2021.

[302] A. K. Majumdar, E. D. Hinkley, and R. T. Menzies, "Infrared Transmission at the 3.39μm Helium-Neon Laser Wavelength in Liquid Quartz Fibers", *IEEE Journal of Quantum Electronics*, **15**, (6), 408–410, 1979.

[303] R. M. Gerosa, A. Sudirman, L. de S. Menezes, W. Margulis, and C. J. S. de Matos, "All-fiber high repetition rate microfluidic dye laser", *Optica*, **2**, (2), 186–193, 2015.

[304] R. M. Derosier and J. Stone, *Low-loss splices in optical fibers*, 1973.

[305] A. Geilen, A. Popp, D. Das, *et al.*, "Exploring extreme thermodynamics in nano-liter volumes through stimulated Brillouin-Mandelstam scattering", *arXiv*, **2208**, (04814), 2022.

[306] L. Michaeli and A. Bahabad, "Genetic algorithm driven spectral shaping of supercontinuum radiation in a photonic crystal fiber", *Journal of Optics*, **20**, (55501), 1–5, 2018.

[307] B. Wetzel, M. Kues, P. Roztocki, *et al.*, "Customizing supercontinuum generation via on-chip adaptive temporal pulse-splitting", *Nature communications*, **9**, (4884), 1–10, 2018.

[308] U. Teğin, B. Rahmani, E. Kakkava, N. Borhani, C. Moser, and D. Psaltis, "Controlling spatiotemporal nonlinearities in multimode fibers with deep neural networks", *APL Photonics*, **5**, (3), 2020.

[309] D. Stucchi, A. Corsini, G. Genty, G. Boracchi, and A. Foi, "A Weighted Loss Function to Predict Control Parameters for Supercontinuum Generation Via Neural Networks", *IEEE International Workshop on Machine Learning for Signal Processing*, (310441), 2021.

[310] M. Shih, H. D. Nelson-Quillin, K. E. Garrett, *et al.*, "Maximizing supercontinuum bandwidths in gas-filled hollow-core fibers using artificial neural networks", *Journal of Applied Physics*, **133**, (233101), 1–12, 2023.

[311] K. F. Lee, A. Rolland, P. Li, J. Jiang, and M. E. Fermann, "Coherent supercontinuum shaping for multiple wavelength optimization over an octave", *Optics Express*, **30**, (1), 427–435, 2022.

[312] M. Afsharnia, Z. Lyu, T. Pertsch, M. A. Schmidt, S. Saravi, and F. Setzpfandt, "Spectral tailoring of photon pairs from microstructured suspended-core optical fibers with liquid-filled nanochannels", *Optics Express*, **30**, (16), 29680–29693, 2022.

[313] T. Wang, S. Y. Ma, L. G. Wright, T. Onodera, B. C. Richard, and P. L. McMahon, "An optical neural network using less than 1 photon per multiplication", *Nature Communications*, **13**, (1), 1–8, 2022.

[314] M. Chemnitz, *Smart Photonics at Leibniz-IPHT*, 2023. [Online]. Available: https://www.leibniz-ipht.de/en/departments/smart-photonics-2/ (visited on 07/04/2023).

[315] A. Klenner, A. S. Mayer, A. R. Johnson, *et al.*, "Gigahertz frequency comb offset stabilization based on supercontinuum generation in silicon nitride waveguides", *Optics Express*, **24**, (10), 11043–11053, 2016.

[316] K. Gürel, V. J. Wittwer, S. Hakobyan, S. Schilt, and T. Südmeyer, "Carrier envelope offset frequency detection and stabilization of a diode-pumped mode-locked Ti:sapphire laser", *Optics Letters*, **42**, (6), 1035–1038, 2017.

[317] Y. Okawchi, M. Yu, B. Desiatov, *et al.*, "Chip-based self-referencing using integrated lithium niobate waveguides", *Optica*, **7**, (6), 702–707, 2020.

[318] S. A. Diddams, D. J. Jones, J. Ye, *et al.*, "Direct link between microwave and optical frequencies with a 300 THz femtosecond laser comb", *Physical Review Letters*, **84**, (22), 5102–5105, 2000.

[319] M. Zimmermann, C. Gohle, R. Holzwarth, T. Udem, and T. W. Hänsch, "Optical clockwork with an offset-free difference-frequency comb: accuracy of sum- and difference-frequency generation", *Optics Letters*, **29**, (3), 310–312, 2004.

List of publications

Publications as first author

Ramona Scheibinger, Niklas M. Lüpken, Mario Chemnitz, Kay, Schaarschmidt, Jens Kobelke, Carsten Fallnich, and Markus A. Schmidt, Higher-order mode supercontinuum generation in dispersion-engineered liquid-core fibers. *Scientific Reports* **11**, 5270 (2021).

Ramona Scheibinger, Johannes Hofmann, Kay, Schaarschmidt, Mario Chemnitz, and Markus A. Schmidt, Temperature-sensitive dual dispersive wave generation of higher-order modes in liquid-core fibers. *Laser & Photonics Reviews* **17**, 1 (2023).

Publications as co-author

Mario Chemnitz, **Ramona Scheibinger**, Christian Gaida, Martin Gebhardt, Fabian Stutzki, Sebstian Pumpe, Jens Kobelke, Andreas Tünnermann, Jens Limpert, and Markus A. Schmidt. Thermodynamic control of soliton dynamics in liquid-core fibers. *Optica* **5** 6 (2018).

Mario Chemnitz, Saher Junaid, Nico Walther, **Ramona Scheibinger**, Kay Schaarschmidt, Jens Kobelke, and Markus A. Schmidt. Tailoring soliton fission at telecom wavelengths using composite-liquid-core fibers. *Optics Letters* **45** 11 (2020).

Xue Qi, Kay Schaarschmidt, Guangrui Li, Saher Junaid, **Ramona Scheibinger**, Tilman Lühder, and Markus A. Schmidt. Understanding Nonlinear Pulse Propagation in Liquid Strand-Based Photonic Bandgap Fibers. *Crystals* **11** 305 (2021).

Niklas M. Lüpken, Maximilian Timmerkamp, **Ramona Scheibinger**, Kay Schaarschmidt, Markus A. Schmidt, Klaus-J. Boller, and Carsten Fallnich. Numerical and Experimental Demonstration of Intermodal Dispersive Wave Generation. *Laser & Photonics Reviews* **15** 9 (2021).

Saher Junaid, Wenqin Huang, **Ramona Scheibinger**, Kay Schaarschmidt, Henrik Schneidewind, Pascal Paradis, Martin Bernier, Réal Valée, Sarmiza-Elena Stanca, Gabriel Zieger, and Markus A. Schmidt. Attenuation coefficients of selected organic and inorganic solvents in the mid-infrared spectral domain. *Optical Materials Express* **12** 4 (2022).

Xue Qi, **Ramona Scheibinger**, Johannes Nold, Saher Junaid, Mario Chemnitz, and Markus A. Schmidt. Axial dispersion-managed liquid-core fibers: A platform for tailored higher-order mode supercontinuum generation. *APL Photonics* **7** 116106 (2022).

Fengji Gui, Shiqi Jiang, Torsten Wieduwilt, **Ramona Scheibinger**, Johannes Hofmann, Ronny Förster, and Markus A. Schmidt. The Light Strand: exploring flat-field modes for tracking single nano-objects. *OPTICA* **10** 6 (2023).

Ying Wan, Xue Qi, Johannes Hofmann, **Ramona Scheibinger**, Guobin Gia, Fengji Gui, Jonathan Plentz, Jianxiang Wen, and Markus A. Schmidt. Optical heating-induced spectral tuning of supercontinuum generation in liquid core fibers using multiwall carbon nanotubes. *31* 19 (2023).

Oral talks at international and local conferences and seminars

Ramona Scheibinger, Mario Chemnitz, Kay Schaarschmidt, and Markus A. Schmidt. Tunable Supercontinuum Generation within Higher-Order Modes in Liquid-Core Optical Fibers. *General Assembly of the German Bunsen Society for Physical Chemistry* (2019)

Ramona Scheibinger, and Markus A. Schmidt. Tunable Supercontinuum Generation of Higher-Order Modes in Liquid-Core Optical Fibers. *Canadian-German Online seminar (CREATE - GRK2101)* (2019)

Ramona Scheibinger, Mario Chemnitz, Kay Schaarschmidt, and Markus A. Schmidt. Higher-Order Mode Temperature-Tunable Supercontinuum Generation in Liquid-Core Optical Fibers. *CLEO Europe* (2019)

Ramona Scheibinger, Pascal Paradis, Réal Vallée, Martin Bernier, Markus A. Schmidt. Mid-IR Supercontinuum Generation in Liquid-Core Fibers. *Canadian-German online seminar (CREATE - GRK2101)* (2020)

Ramona Scheibinger, Johannes Hofmann, Mario Chemnitz, and Markus A. Schmidt. Local control of supercontinuum generation in liquid-core fibers via temperature. *Dornburg seminar for all doctoral candidates of Leibniz-IPHT* (2021)

Ramona Scheibinger, Johannes Hofmann, Mario Chemnitz, and Markus A. Schmidt. Local control of supercontinuum generation in liquid-core fibers via temperature. *DoK-DoK conference* (2021)

Ramona Scheibinger, Johannes Hofmann, Mario Chemnitz, and Markus A. Schmidt. Tailored Tuning of Temperature-Controlled Supercontinuum Generation in Liquid-Core Fibers. *CLEO US* (2022)

For conference contributions as co-author, please refer to
https://www.researchgate.net/profile/Ramona-Scheibinger.

Ehrenwörtliche Erklärung gemäß § 5 Satz 2 Nr. 3 PromO

Hiermit erkläre ich ehrenwörtlich,

1.1. dass mir die geltende Promotionsordnung bekannt ist;

1.2. dass ich die Dissertation selbst angefertigt habe, keine Textabschnitte eines Dritten oder eigener Prüfungsarbeiten ohne Kennzeichnung übernommen und alle von mir benutzten Hilfsmittel, persönlichen Mitteilungen und Quellen in meiner Arbeit angegeben habe;

1.3. dass bei der Auswahl und Auswertung folgenden Materials mich die nachstehend aufgeführten Personen in der jeweils beschriebenen Weise unterstützt haben:

- Durchführung und Auswertung der Absorptionsmessungen von CS_2: Wenqin Huang und Saher Junaid (Leibniz-IPHT).

- Aufnahme und Auswertung der REM-Bilder der Faserquerschnitte: Franka Jahn, Andrea Dellith und Jan Dellith (Leibniz-IPHT).

- Automatisierung und Ansteuerung der Peltierelemente, der Spektrometer, Powermeter und Wärmebildkamera: Johannes Hofmann (Leibniz-IPHT).

- Entwicklung und Bereitstellung des Codes zum Lösen der nicht-linearen Schrödingergleichung und zugehöriger Codes zum Auswerten: Mario Chemnitz (Leibniz-IPHT).

- Implemetierung, Durchführung und Auswertung der modengekoppelten Simulationen der Superkontinuumsgeneration: Niklas Lüpken (WWU Münster).

1.4. dass die Hilfe einer kommerziellen Promotionsvermittlerin/eines kommerziellen Promotionsvermittlers nicht in Anspruch genommen wurde und dass Dritte weder unmittelbar noch mittelbar geldwerte Leistungen für Arbeiten erhalten haben, die im Zusammenhang mit dem Inhalt der vorgelegten Dissertation stehen;

1.5. dass die Dissertation noch nicht als Prüfungsarbeit für eine staatliche oder andere wissenschaftliche Prüfung eingereicht wurde;

1.6. dass eine gleiche, eine in wesentlichen Teilen ähnliche oder eine andere Abhandlung nicht bei einer anderen Hochschule als Dissertation eingereicht wurde.

Jena, den ....
                                          (Ramona Scheibinger)

Acknowledgement

I thank Prof. Markus Schmidt for providing a great environment for research and for his excellent guidance in the last 5 years. I appreciate a lot your efforts to ensure a good working atmosphere in this highly international research group and the mutual respect we shared. The weekly meetings in small groups were really helpful to continuously move forward my projects, especially when facing problems in the lab.

I thank Mario Chemnitz for the introduction to soliton-driven nonlinear optics, the many questions he answered and the inspiration he passed on.

I thank Johannes Hofmann who developed the automated system to control the temperature and who is continuing the work on thermally tuned nonlinear waveguides.

I thank Wenqin Huang and Saher Junaid for the absorption measurements of CS_2, and the investigation of further nonlinear liquids.

I thank Xue Qi and Kay Schaarschmidt for the detailed discussions about nonlinear effects in general, and soliton fission in detail.

I thank Shahrzad Hosseinabadi, Johannes Hofmann, Xue Qi, Saher Junaid and David Vasquez Pinzon for proof reading my thesis.

I thank the competence center for specialty fibers at IPHT for drawing the optical fibers for me, and Franka Jahn, Andrea Dellith and Jan Dellith for characterizing them.

I thank Pascal Paradis and his supervisors Prof. Martin Bernier and Prof. Real Vallée who hosted me for few months at COPL in Québec, where preliminary transmission measurements of CS_2 set the basis for successful measurements at IPHT. It was a pleasure working in such an excellent team with your mid-IR lasers.

I thank Niklas Lüpken and Prof. Carsten Fallnich for the collaboration investigating the coupling of different higher-order modes.

I thank all my colleagues in the hybrid fiber group for their support and the nice conversations we had in the office, and during the lunch breaks. Without your positive spirit our workplace would not have been so friendly and bright.

I thank all members of the PhD council of Leibniz-IPHT for their efforts to connect PhD students and improve their development conditions at the institute. Our possibilities would have been strongly restricted without the support from the institute's head, the PR department and the work's council. Thanks to Neus Allande Calvet for leading the council together with me for a year. And thanks to Amir Nakar, Tino Fremberg and all the previous representatives for paving the way for us.

I thank my peers from the GRK research training group and my colleagues at the optical museum for the team spirit we shared. Thanks to Anna Späthe - you were a great coordinator.

I thank Keshav Jha for starting so many working days with a relaxing yoga session and teaching me how to guide through yoga sessions on my own.

I thank my friends and my family. Your support and love gave me the power and endurance for this project.